Coherent feedback cooling of a nanomechanical membrane with atomic spins

Inauguraldissertation

zur
Erlangung der Würde eines Doktors der Philosophie
vorgelegt der
Philosophisch-Naturwissenschaftlichen Fakultät
der Universität Basel

von

Chun Tat Ngai

2023

Genehmigt von der Philosophisch-Naturwissenschaftlichen Fakultät
auf Antrag von

Prof. Dr. Philipp Treutlein
Prof. Dr. Christoph Bruder
Prof. Dr. Eugene Simon Polzik

Prof. Dr. Marcel Mayor
The Dean of Faculty

Basel, den 22.03.2022

Contents

Abstract

This thesis focuses on the engineering of light-mediated interaction between distinct quantum system. Specifically, we present experiments on the light-mediated interaction between a nanomechanical membrane oscillator and a collective atomic spin. The mechanical oscillator, a silicon nitride membrane mounted in a single-sided cavity, couples to the light via radiation pressure in a room temperature environment. The spin oscillator, consisting of an optically pumped ensemble of cold Rubidium atoms held in a dipole trap, couples to light via the off-resonant Faraday interaction. By engineering a light mediated interaction between the mechanical oscillator and the atomic spin in a loop geometry, we experimentally demonstrate strong bidirectional Hamiltonian coupling between membrane and spin. We observe normal-mode splitting and coherent energy exchange oscillations as signatures of strong coupling. Combining this strong coherent coupling with the versatile quantum control on the atomic spin we demonstrate for the first time, coherent feedback cooling of a mechanical oscillator using the atomic spins as a coherent controller. We explore different coupling regimes, i.e. from incoherent overdamped cooling to strong stroboscopic coherent feedback. Spin-membrane state swaps along with stroboscopic spin pumping allows us to cool our mechanical oscillator from room-temperature to $T = 216\,\mathrm{mK}$ in $200\,\mu s$. Moreover, we study the effect of delays on the cooling performance. In a further experiment, we exploit the strong correlation between the atomic spin and light to achieve ponderomotive squeezing of light, which is a hallmark of reaching the backaction dominated regime. The squeezing of light allows one to perform measurements with a precision beyond the standard quantum limit, which has many strong implications in quantum metrology.

Chapter 1

Introduction

Quantum technologies have seen an unprecedented development along with increasingly mature control over diverse quantum systems, ranging from photons [1], atoms [2], ions [3] and solid state spins [4, 5] to mesoscopic superconducting [6, 7] and nanomechanical devices [8, 9]. During this ongoing effort, it became apparent that no single quantum system serves as a universal quantum hardware to meet the stringent requirements of all quantum protocols [10]. The plethora of hybrid systems developed in the past decade that integrate disparate quantum systems with complementary functionalities [11] might be key to acquire such multitasking capabilities. Among these hybrid systems, spin-mechanics interfaces in which a nanomechanical oscillator is coupled to a spin emerge as a prominent candidate [12–20]. The interest in hybrid systems stems from the fact that hybrid systems generally involve distinct quantum systems that combine the overall strengths while mitigating the possible weakness of the individual systems [11]. For spin-mechanical systems, mechanical oscillators offer a universal interface between distinct quantum systems owing to their ability to respond to a wide variety of forces [21]. For example, mechanical oscillators can couple to spin systems such as atomic ensembles [12–15, 22, 23], quantum dots [24, 25] or solid-state devices [11, 16–20, 26] via light-, strain-, or magnetically-mediated interactions. At the same time, the microscopic spins can be used to control, read-out and lend new functionalities to the macroscopic mechanical device [21]. These hybrid mechanical platforms equipped with multitasking capabilities holds exciting prospects and a variety of potential applications have already been proposed ranging from fundamental physics [27] and quantum communication [10] to quantum information processing [21, 28].

In our experiment, the hybrid system considered involves atomic spins coupled to a nanomechanical oscillator via light. Despite the distinct differences between the two systems, surprisingly, the two systems couple to light in a similar fashion. Over the years, many similar theoretical concepts [29, 30] and experimental techniques [9] have been developed independently. In the following, we discuss the

background of the individual light-matter interfaces in detail.

Atomic ensembles

The first pioneering experiments for coherent control of atoms concerned the study of light interacting with one or only a few atoms inside an optical cavity [31, 32]. Due to the experimental technical challenge, the interaction between a spin ensemble and light emerged as a viable alternative to achieve strong, coherent light-matter interaction [33]. Although there exist other coupling mechanisms [33–35] between atomic ensemble and light, here we refer to the coupling of a spin ensemble to light in free space via the Faraday effect [33, 36]. In simple terms, it corresponds to the rotation of the polarization of light due to the atomic spin orientation [33]. Over the past decades, the Faraday interface has seen tremendous progress, in particular it was used to create squeezed states of light [37] and spin [38] to generate entanglement between two spin ensembles [39] which finds important applications in quantum metrology [40]. Moreover, state-of-the-art experiments exploiting the Faraday interaction have also demonstrated applications in quantum memories for light [41], quantum teleportation [42], continuous quantum non-demolition of atomic spin ensembles [36] and magnetometry [43, 44].

Mechanical oscillator

While quantum control of the motional state of atomic systems has been well-established for decades [3, 45], it has only been until recent years that, mechanical systems have seen rapid development thanks to the advent of nanofabrication technology [46, 47]. Mechanical devices with excellent quality factors $Q_m > 10^7 - 10^8$ [48, 49] allow cavity optomechanical systems to operate at a low thermal decoherence rates, which paves way to quantum coherent control of mechanical motion. State-of-the-art optomechanical systems have been used for experiments on measurement based feedback [50], resolved sideband cooling [51] which have brought the mechanical oscillator to its quantum ground state, enabling quantum state control and manipulation of the mechanical motion. Moreover, cavity optomechanical systems have already found important applications covering different fields of physics, including gravitational wave detection [52], precision force sensing [53], generation of squeezed mechanical states [54, 55] and light [56] and signal transduction [57].

Hybrid spin-mechanical interface

A further exciting possibility is to couple the atomic ensemble and the mechanical oscillator using light to realize a hybrid platform. Such hybrid atom-mechanical systems have been realized in the past decade. Early pioneering experiment involves the sympathetic cooling of a mechanical membrane by coupling to the center-of-mass of the atomic ensemble via light in Philipp Treutlein's group at

Basel [13, 22]. Later, the motional state coupling experiment was also realized at Christoph Becker's group in Hamburg by exploiting feedback cooling to a pre-cooled membrane inside a cryostat [23], which allowed the membrane to reach a lower temperature. In parallel to these experimental works, Eugene Polzik's group at the Neils Bohr Institute demonstrated quantum backaction noise suppression where a mechanical oscillator and a negative-effective-mass spin oscillator are both coupled to light in a cascaded fashion [12]. In a later experiment, they also demonstrated the generation of entanglement between the two systems [15].

In previous work of our group, interesting coupled dynamics between the mechanical oscillator and the center of mass motion of the atoms in an optical lattice was observed [58]. However, the broad spread of the atomic motional frequencies did not offer the possibility for coherent control. To achieve coherent control of these hybrid system, an important prerequisite i.e. "strong coupling" has to be satisfied. This implies the light-mediated coupling strength exceeds the damping rates of the individual systems. To achieve strong coupling, Karg et al. [30] derived the condition that permits Hamiltonian interactions mediated by light between distant quantum systems over a long distance. It turns out that, contrary to single pass cascaded systems [12,15], to achieve strong, bidirectional Hamiltonian coupling, the light field needs to interact with the systems twice, and the second interaction erases the information obtained on the light from the first pass [30]. We successfully demonstrated the first strong reversible, bidirectional Hamiltonian coupling by arranging the coupling beam such that it interacts twice with the spin, thereby the backaction on the spin is evaded [14,59]. By initializing the spin to the lowest energy configuration, we observe normal-mode splitting and coherent energy exchange oscillations, a hallmark of strong coherent coupling between systems.

Building on our strong coupling result, we exploit the strong light-mediated coupling to demonstrate the concept of coherent feedback, which sets the main theme of this work. Coherent feedback [60,61] involves the coupling of two systems while preserving the quantum coherence between them. In contrast to the measurement based feedback [62], coherent feedback does not require any measurement, thereby the associated backaction and decoherence are avoided. In the context of cooling the mechanical oscillator, previous theoretical studies compare coherent feedback to measurement based feedback, showing that in a certain parameter regime, the coherent feedback strategy can outperform measurement based feedback leading to more efficient cooling [63,64]. In analogy to classical control theory, in a coherent feedback platform, the mechanical system would act as the system to be controlled, i.e. the plant, which is coupled to a noisy thermal environment, and the spin would play the role of the controller, coupled to a zero-temperature bath, which steers the mechanical system towards a target state. In this thesis, we report on the first experimental demonstration of coherent feedback cooling of a mechanical oscillator using the atomic spins as a feedback controller. The strong coupling Hamiltonian provides a beamsplitter interaction between the spin and

membrane that we use to perform a state swap between them, which transfers the thermal excitations from the membrane to the spin. By applying optical pumping to the spin ensemble, we are able to reinitialize the spin to its ground state before the next state swap takes place. We first observed by applying continuous pumping pulses with varying intensity, the smooth transition from strong coupling to an overdamped regime. By interleaving the coherent state swap with strong spin pumping pulses in a timely manner, we reached the phonon steady state faster than in continuous cooling regime. In principle, our coherent feedback platform provides an efficient cooling method for low frequency mechanical oscillators in the bad cavity regime [64]. Moreover, cooling of the mechanical device close to its ground state could enable quantum protocols such as the generation of nonclassical mechanical states via state swaps from the atomic system [65]. Furthermore, on the atomic spin side, recently, in analogy to the ponderomotive squeezing of light observed in cavity optomechanical systems, we exploited the strong correlations of the spin-light interaction to generate squeezing of the polarization of light.

The main result of this thesis were published in [14,66]. The structure of this thesis is organized as follows:

Chapter 2 and 3 introduces the theory of the spin system and the experimental characterization of the dispersive Faraday interaction between light and the atomic spin.

Chapter 4 introduces the basic optomechanical theory and the experimental characterization of the membrane in the bad cavity limit.

Chapter 5 introduces the hybrid experimental setup that realizes the light-mediated interaction between the spin and the membrane and summarizes the strong coupling result as well as the theoretical methods to analyze the spin-membrane coherent feedback cooling results.

Chapter 6 presents the experimental realization of coherent feedback cooling of the nanomechanical membrane with atomic spins.

Chapter 7 contains a conclusion and provides an outlook on future experiments in the quantum regime.

Theory of spin-light interface

This chapter covers the theory of the spin-light interface involved in our hybrid experiment. We begin with an introduction to the quantum mechanical description of an atomic spin and light, which constitutes the basis for the discussion of an off-resonant dipole atom-light interaction in the subsequent section. Moreover, we discuss the limits where the atom-light interaction can be reduced to the Faraday interaction. From this, we establish the input-output relations for quantum non-demolition (QND) read out of the spin oscillator using a free space laser beam. Furthermore, we generalize our spin light interface model to describe non-uniform interaction between the optical mode and the atomic ensemble. In the end of this chapter, we briefly discuss the spin-light interface in the quantum regime, including the standard quantum limit (SQL) and the squeezing of light quadratures using atomic spin. The theoretical models present here should serve as the basis for the discussion of the experimental result of the spin-light interface in Chapter 3.

2.1 Atoms

Our collective atomic spin is comprised of an ensemble of cold, neutral non-interacting ^{87}Rb atoms. The spin degree of freedom originates naturally from the internal structure of the ^{87}Rb atom in the ground state (see Fig. 2.1). The outer-most electron carries spin of $s = 1/2$ and orbital angular momentum $l = 0$, which gives rise to the electronic ground state $5^2S_{1/2}$ with total angular momentum of $j = 1/2$. Moreover, ^{87}Rb has a nuclear spin of $i = 3/2$. Due to the hyperfine coupling between the nucleus and electron spins, the ground state $5^2S_{1/2}$ is further split into two hyperfine manifolds labeled by quantum number $f = 1, 2$ as shown in Fig. 2.1 (a).

Each individual atom (labeled by index i) can be seen as a single spin carrying total angular momentum $\mathbf{f}^{(i)}$, with spin length $|\mathbf{f}^{(i)}| = f$. To describe the whole atomic ensemble, we may introduce a collective spin vector $\mathbf{F}$ by summing up the

individual spins of the ensemble,

$$\mathbf{F} = \sum_{i=1}^{N} \mathbf{f}^{(i)} \tag{2.1}$$

where the collective spin length $|\mathbf{F}| = fN$ for a symmetric state of maximum collective spin eigenvalue, and N is the number of atoms. The collective spin obeys the usual commutation relation for angular momentum $[F_y, F_z] = iF_x$. In this experiment, the atomic ensemble consists of $N \sim 10^7$ atomic spins well polarized along the magnetic field in the x direction. Thus we may treat $F_x \approx \bar{F}_x$ as a classical number (where the bar indicates its mean value), whereas each individual spin is aligned along x such that the transverse spin components $\langle F_y \rangle$, $\langle F_z \rangle \approx 0$ are quantum mechanical in nature. Moreover, this highly oriented collective spin $\bar{F}_x \approx -Nf$ precesses with a small amplitude around the magnetic field in the x-direction [see Fig. 2.1(b)]. Therefore, we may use the Holstein Primakoff approximation (HPA) [67] to describe the transverse components of the spin oscillator in terms of the position X_s and momentum P_s quadrature of a spin harmonic oscillator, respectively:

$$X_s = \frac{F_z}{\sqrt{|\bar{F}_x|}} = \frac{b_s + b_s^\dagger}{\sqrt{2}}, \quad P_s = \frac{F_y}{\sqrt{|\bar{F}_x|}} = \frac{b_s - b_s^\dagger}{\sqrt{2}i} \tag{2.2}$$

where b_s, $b_s^\dagger$ are the bosonic annihilation and creation operators of the spin excitations. The spin quadratures satisfy the canonical commutation relation $[X_s, P_s] = i$. This approximation effectively maps the highly oriented collective spin state $|F = 2, m_F = -2\rangle$ to the ground state $|0_s\rangle$ of the spin oscillator with respect to the quantization axis along x. The approximation holds well as long as the number of the spin excitations remain small compared to the magnitude of the collective spin $\langle \Psi_s | b_s^\dagger b_s | \Psi_s \rangle \ll \bar{F}_x$. Moreover, the Heisenberg uncertainty relation for the transverse spin components holds,

$$\Delta F_y \cdot \Delta F_z \geq \frac{|\bar{F}_x|}{2}, \quad \Delta X_s \cdot \Delta P_s \geq \frac{1}{2} \tag{2.3}$$

where ΔF_z (ΔX_s), ΔF_y (ΔP_s) represent the standard deviation of the ground state fluctuations that follows a Gaussian distribution. As shown in Fig. 2.1(c), the starting point of most experiments present here involves the preparation of the spin ensemble in the minimum uncertainty state (also called coherent spin state (CSS) [68] in the literature), where the noise spread in the amplitude and phase quadratures are equally distributed. In the outlook (see Chapter. 7), we briefly touch on the spin squeezed state, which can be achieved via one axis twisting squeezing Hamiltonian [see Fig.2.1(d)]. In contrast to CSS, this type of spin state has reduced noise spread in the squeezed spin quadrature at the expense of increased noise spread in anti-squeezed quadrature.

(a)

$f = 2$

$5^2 S_{1/2}$

$f = 1$

$-2 \quad -1 \quad \underset{m_f}{0} \quad 1 \quad 2$

(b)

(c)

(d)

B_0

P_s

X_s

P_s

X_s

P_s

X_s
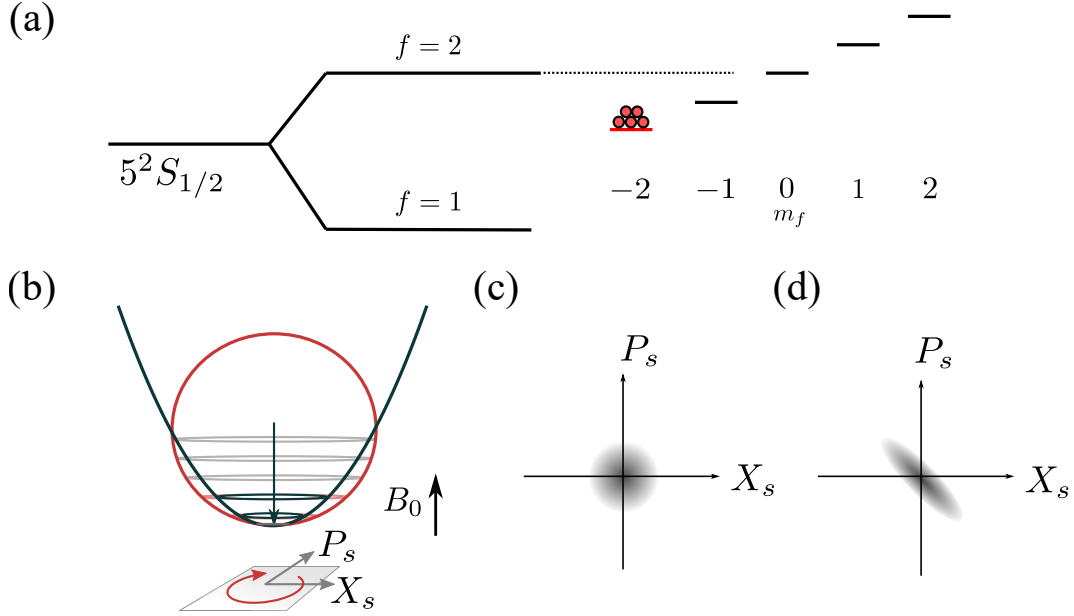
Figure 2.1: (a) Simplified internal level structure of the ^{87}Rb ground state, the hyperfine ground states are labeled by quantum number $f = 1, 2$ and the magnetic field causes further splitting into Zeeman sublevels. (b) Mapping of a collective spin (solid dark red circle) to a spin oscillator (dark solid parabola), and the dark blue arrow indicates the direction of the spin and the black arrow indicates the magnetic field. (c) Phase space diagram of the minimum uncertainty state in the vacuum state $|0_s\rangle$, the grey region indicates the zero-point fluctuation of the transverse spin components in the vacuum state (d) Phase space diagram of a spin squeezed state.

2.2 Light

In our experiment, light plays the role as a quantum bus to exchange excitations between the membrane and the spin oscillator. Moreover, light also plays the role as a meter which allows independent read out of the state of the individual oscillator. Here, we discuss the general properties of the light, including the quantum noise of light which becomes convenient when we discuss measurement close to quantum limit in Sec. 2.9.

For simplicity, here we consider the paraxial mode of a laser beam with wave vector $k_L = \omega_L/c$ propagating in the z direction, where c is the speed of light. As found in many textbooks [69], the positive frequency part of the electric field in the paraxial approximation reads:

$$\mathbf{E}^{(+)} = \mathcal{E}_0 \left(a_-(\zeta)\mathbf{e}_- + a_+(\zeta)\mathbf{e}_+ \right) e^{ik_L z} \tag{2.4}$$

$$= \mathcal{E}_0 \left(a_x(\zeta)\mathbf{e}_x + a_y(\zeta)\mathbf{e}_y \right) e^{ik_L z} \tag{2.5}$$

where $\mathcal{E}_0 = \sqrt{\hbar \omega_L / 2 \epsilon_0 c A}$ contains the angular frequency of the light ω_L, the dielectric constant ϵ_0, the mode area of the probe laser beam A. Throughout this work, the light field is expressed either in the basis of circular polarization, i.e. $\mathbf{e}_- = (\mathbf{e}_x - i\mathbf{e}_y)/\sqrt{2}$ and $\mathbf{e}_+ = -(\mathbf{e}_x + i\mathbf{e}_y)/\sqrt{2}$ or in the linear basis $(\mathbf{e}_x, \mathbf{e}_y)$. Moreover, we used the Fourier transform of the electromagnetic mode with polarization $\sigma \in (+, -)$ or $\sigma \in (x, y)$.

$$a_\sigma(\zeta) = \frac{1}{\sqrt{2\pi}} \int d\omega a_\sigma(\omega) e^{i\omega\zeta/c} \tag{2.6}$$

labeled by the position coordinate ζ. The creation and annihilation operators follow the commutation relations in the position and frequency domains

$$[a_\sigma(\zeta), a_{\sigma'}^\dagger(\zeta')] = c\delta_{\sigma,\sigma'}\delta(\zeta - \zeta'), \quad [a_\sigma(\omega), a_{\sigma'}^\dagger(\omega')] = \delta_{\sigma,\sigma'}\delta(\omega - \omega') \tag{2.7}$$

where $a_\sigma^\dagger(\zeta)a_\sigma(\zeta)$ is the photon flux with σ polarization at position ζ (unit: $s^{-1} =$ Hz) and $a_\sigma^\dagger(\omega)a_\sigma(\omega)$ is the corresponding spectral density at angular frequency ω (unit: Hz^{-1}), respectively. Often we use the polarization of light to encode the information imprinted by the spin or membrane oscillator involved in the experiment. The polarization state of the light can be represented by the stokes vector $\mathbf{S}$ on a Poincáre sphere as shown in Fig. 2.2(a):
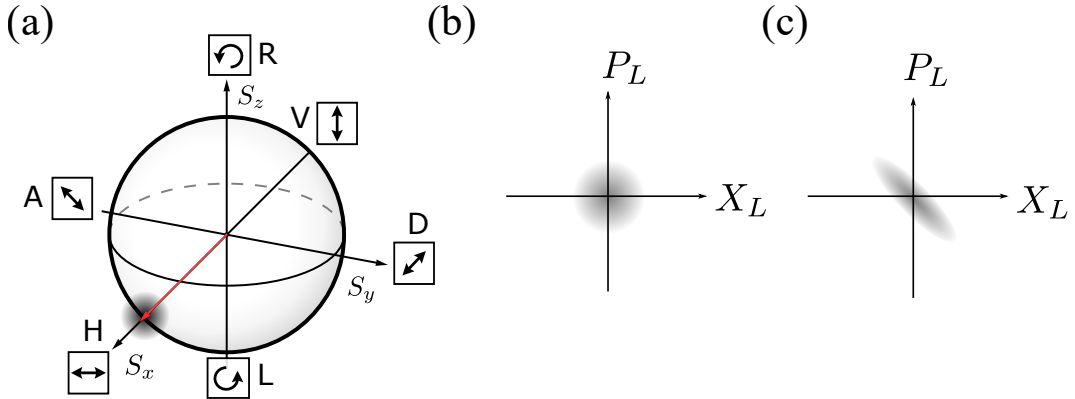
Figure 2.2: (a) Representation of the Poincáre sphere, the stokes vector points along S_x, the quantum signals are encoded in S_y and S_z (b) Phase space diagram of the minimum uncertainty state in the ground state (c) Phase space diagram of a ponderomotive squeezed state.

The stokes vector is described by four stokes components, i.e. $\mathbf{S} = (S_0, S_x, S_y, S_z)$. The first stokes component is proportional to the total photon flux $S_0 = \Phi_L/2$, whereas S_x, S_y, S_z correspond to the differential photon flux for the following choice of bases, i.e. horizontal (H) vs vertical (V) polarization, diagonal (D) vs anti-diagonal (A) polarization and right-hand circular polarized light (R) vs left-hand circular polarized light (L), respectively. For most cases, we assume the input

light is described by stokes vector that points along the x-axis (indicated by the solid red arrow) where $S_x \approx S_0$ and the S_y and S_z encode the quantum signals from the spin oscillator. The stokes vector is defined by

$$S_0 = \frac{1}{2}\left(a_+^\dagger a_+ + a_-^\dagger a_-\right) = \frac{1}{2}(a_x^\dagger a_x + a_y^\dagger a_y) \tag{2.8}$$

$$S_x = \frac{1}{2}\left(a_+^\dagger a_- + a_-^\dagger a_+\right) = \frac{1}{2}(a_x^\dagger a_x - a_y^\dagger a_y) \tag{2.9}$$

$$S_y = \frac{1}{2i}\left(a_+^\dagger a_- - a_-^\dagger a_+\right) = \frac{1}{2}(a_x^\dagger a_y + a_y^\dagger a_x) \tag{2.10}$$

$$S_z = \frac{1}{2}\left(a_+^\dagger a_+ - a_-^\dagger a_-\right) = \frac{1}{2i}(a_x^\dagger a_y - a_y^\dagger a_x) \tag{2.11}$$

Note that in these equations, the left hand side refers to the components of the Stokes vectors on the Poincáre sphere, while the right hand side refers to the x and y polarization in the lab frame. From the commutation relation of the mode operators $a_\sigma(\zeta)$, the stokes vector also satisfies the angular momentum commutation relation $[S_y, S_z] = ic\delta(\zeta - \zeta')S_x$ and the Heisenberg uncertainty relation reads

$$\Delta S_y \cdot \Delta S_z \geq c\frac{|\bar{S}_x|}{2}\delta(\zeta - \zeta') \tag{2.12}$$

where ΔS_y, ΔS_z represent the standard deviation of the white quantum noise that follows a Gaussian distribution. This noise is also called the shot noise or imprecision noise in the literature. We can again make the Holstein-Primakoff approximation for the Stokes vector, for $\bar{S}_x \gg \langle a_y^\dagger a_y \rangle$, the amplitude X_L and phase P_L quadrature of light are defined as

$$X_L = \frac{S_y}{\sqrt{|\bar{S}_x|}} = \frac{a_y + a_y^\dagger}{\sqrt{2}}, \quad P_L = \frac{S_z}{\sqrt{|\bar{S}_x|}} = \frac{a_y - a_y^\dagger}{\sqrt{2}i} \tag{2.13}$$

where a_y is the quantum field in the y-polarization. The light quadratures satisfy the canonical commutation relation $[X_L, P_L] = ic\delta(\zeta - \zeta')$ and the Heisenberg uncertainty relation reads $\Delta X_L \cdot \Delta P_L = c\delta(\zeta - \zeta')/2$. As sketched in Fig. 2.2(c), the input state of light is a coherent state, where the quantum noise in both quadratures are equally distributed. Furthermore, as we will see in Sec. 2.10, it is possible to create a polarization squeezed state of light by interfering the oscillator response with the shot noise of the light [see Fig. 2.2 (d)].

2.3 Atom-light interaction

A first principle derivation of atom light interaction that formulates the coupling between the collective spin of an atom ensemble to the polarization state of light was well-established and studied in the literature [33, 36, 42, 70]. Here, we revisit the atom-light formalism and the physical interpretation of the interaction Hamiltonian, decoherence effect and discuss their main consequences.
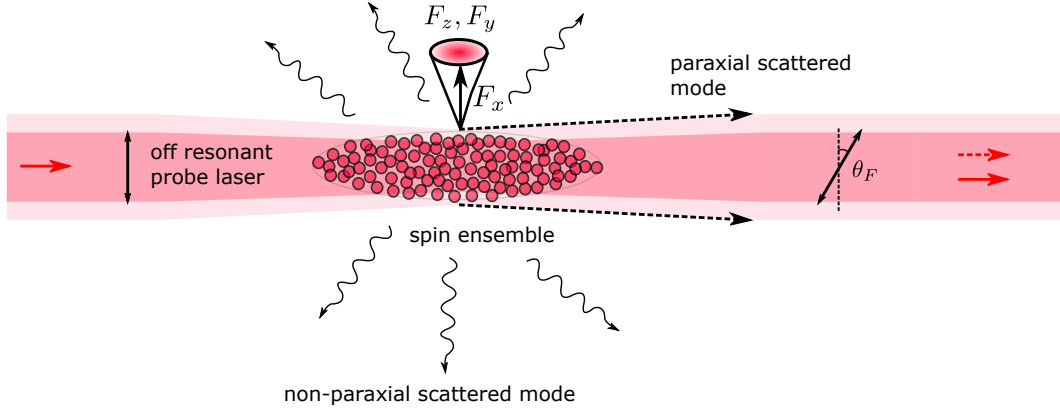
Figure 2.3: Illustration of the spin light interaction, the paraxial probe mode interacts with the spin ensemble, the paraxial scattered mode (light pink color) and the paraxial probe mode (red color) both exit the polarized spin ensemble in the same direction. The non-paraxial mode (indicated by wavy arrow) corresponds to the spontaneous emission into vacuum. Upon the light exits the ensemble, the polarization of the paraxial scattered mode is rotated by Faraday angle θ_F via the Faraday effect.

We first consider the simple scenario where the paraxial mode of the probe laser interacts with one of the atoms in the spin ensemble as shown in Fig. 2.3. This is well described by the electric dipole interaction Hamiltonian $H_{s,\text{int}} = -d \cdot E$, where d is the dipole operator of the atom. In our experiment, we only consider the D_2 line of ^{87}Rb at 780 nm. Here we also define ω_0 to be the resonant frequency of the D_2 transition and the laser-atom detuning to be $\Delta = \omega_L - \omega_0$. It turns out that if the probe laser is far off resonant with respect to the hyperfine excited manifold $5^2P_{3/2}\ f'$ (see Fig. 2.4) with a laser-atom detuning Δ large compared to the hyperfine splitting of the excited states i.e. ($\Delta \sim 10^1 - 10^2$ GHz $\gg \Delta'_{hfs} \sim 10^2$ MHz), the ground state atom no longer resonantly absorbs and emits photons.

Instead, the dynamics of the excited states can be adiabatically eliminated [33], which returns an effective Hamiltonian $H_{s,\text{int}}$ that describes the off-resonant interaction between the collective spin and the light field,

$$H_{s,\text{int}} = -\mathbf{E}^{(-)} \cdot \boldsymbol{\alpha} \cdot \mathbf{E}^{(+)} \tag{2.14}$$

where $\boldsymbol{\alpha}$ is the atomic polarizability tensor. Due to the tensor nature of the atom polarizability, the Eq. 2.14 can be divided into scalar, vector and tensor part $H_{s,\text{int}} = H^{(0)} + H^{(1)} + H^{(2)}$ which we interpret the individual term in detail below. In general, the effect of the individual Hamiltonian consists of a spin part couples to the polarization state of light. Here, we assume the atoms are non-interacting and a uniform spin-light coupling is assumed. The light induces a polarization dependent potential to the atom (known as the AC Stark shift or light shift) and the atom acts on the light field as a spin-state dependent index of refraction.
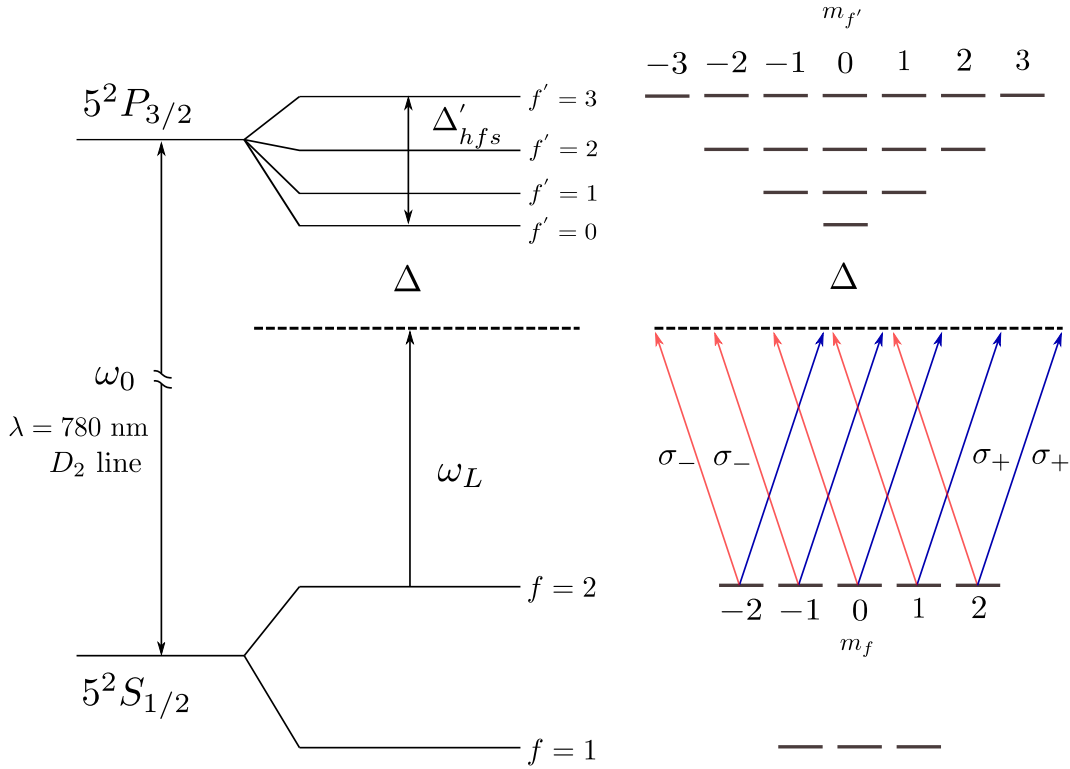
Figure 2.4: Schematic diagram of the ^{87}Rb energy level structure. The off-resonant probe laser beam is detuned from the D_2 optical transition. The blue and red solid lines indicate the σ_- and σ_+ transitions responsible for the dispersive atom light interaction.

First, the scalar Hamiltonian $H^{(0)}$ reads

$$H^{(0)} = \hbar\alpha_0 \mathbb{1}_g S_0 \tag{2.15}$$

where α_0 is the scalar polarisability and $\mathbb{1}_g$ is the projector operator on the ground state manifold.

$$\alpha_0 = \frac{\sigma_\pi}{2A}\frac{\gamma_e}{\Delta} = \frac{\lambda^2}{2\pi A}\frac{\gamma_e}{\Delta} \tag{2.16}$$

where $\sigma_\pi = \lambda^2/\pi$ is the scattering cross section for linear polarization, λ is the wavelength of the probe laser and γ_e is the spontaneous emission rate. The scalar interaction causes a global spin-independent energy shift to the atomic energy levels, depending on light intensity and detuning. For red detuning, the probe beam creates a trapping potential for the atom, whereas for blue detuning, the probe beam induces a repulsive trapping potential. On the other hand, the light experiences a trivial phase shift induced by the atom which can change the divergence of the laser beam.

13

Secondly, the vector Hamiltonian $H^{(1)}$ responsible for QND readout of the spin oscillator reads:

$$H^{(1)} = \hbar \alpha_1 f_z S_z \tag{2.17}$$

where vector polarizability α_1 reads

$$\alpha_1 = \frac{\sigma_\pi}{8A} \frac{\gamma_e}{\Delta} (-1)^f = \frac{\lambda^2}{8\pi A} \frac{\gamma_e}{\Delta} (-1)^f \tag{2.18}$$

where α_1 has opposite sign for $f = 1, 2$. For the vector interaction, the circular polarization of light acts a fictitious magnetic field that acts along the transverse direction of the spin, causing differential energy splitting of the hyperfine Zeeman m_f sublevels. During the spin light interaction, this causes a spin rotating around the z axis by an amount proportional to the circular component of light S_z. On the other hand, the atoms rotate the polarization of light by an amount proportional to the f_z along the propagation axis of the light. This is a circular birefrigent effect of the atom, known as the Faraday effect, which will be the dominant interaction part we use to realize our spin light interface.

Finally, the tensor Hamiltonian $H^{(2)}$ reads:

$$H^{(2)} = \hbar \alpha_2 \left[t_{x^2-y^2} S_x + t_{xy} S_y + \left(\frac{\mathbf{f}^2}{3} - f_z^2 \right) S_0 \right] \tag{2.19}$$

where α_2^f is the tensor polarizability depending on the hyperfine ground state $f = 1, 2$ takes the following expressions in the large detuning limit:

$$\begin{aligned} \alpha_2^{f=1} &\sim \frac{\lambda^2}{8\pi A} \frac{\gamma_e}{\Delta} \frac{-4\delta_0 + 5\delta_1 - \delta_2}{4\Delta} \\ \alpha_2^{f=2} &\sim \frac{\lambda^2}{8\pi A} \frac{\gamma_e}{\Delta} \frac{-\delta_1 + 5\delta_2 - 4\delta_3}{20\Delta} \end{aligned} \tag{2.20}$$

where $\delta_{f'}$ are the frequency offsets of the hyperfine levels relative to the excited state $5^2 P_{3/2}$ f'. And $t_{x^2-y^2}$, t_{xy} correspond to spin alignment tensor terms given by

$$\begin{aligned} t_{x^2-y^2} &= f_x^2 - f_y^2 = \frac{1}{2} \left(f_+^2 + f_-^2 \right) \\ t_{xy} &= f_x f_y + f_y f_x = \frac{1}{2i} \left(f_+^2 - f_-^2 \right) \end{aligned} \tag{2.21}$$

The dynamics of the tensor interaction is less trivial and is discussed in more detail in Sec. 2.6. Here, we provide a qualitative description. The tensor effect is a linear birefrigence effect, which causes a power dependent quadratic splitting of the ground state hyperfine Zeeman sublevels (see Sec. 2.6). On the other hand, for a linearly polarized laser beam, the tensor part of the atom causes the beam to become elliptically polarized i.e. S_y is rotated into S_z, which could drive the spin downstream, acting as a source of spin decoherence due to inhomogeneity of

the laser intensity profile. In general, the tensor interaction is interesting and has practical use e.g. in tomography [70]. However, in this work, we want to minimize the tensor effect as this degrades our QND interaction for readout of the spin oscillator. For this, we work in a large detuning regime and a polarization angle at which the tensor effect becomes negligible. To conclude this section, we discuss the scaling of the different ranks of the atom polarizability to justify that the tensor effect can be neglected. In Fig. 2.5, different ranks of atom polarizability are plotted as a function of laser-atom detuning Δ. We see that the scalar and vector
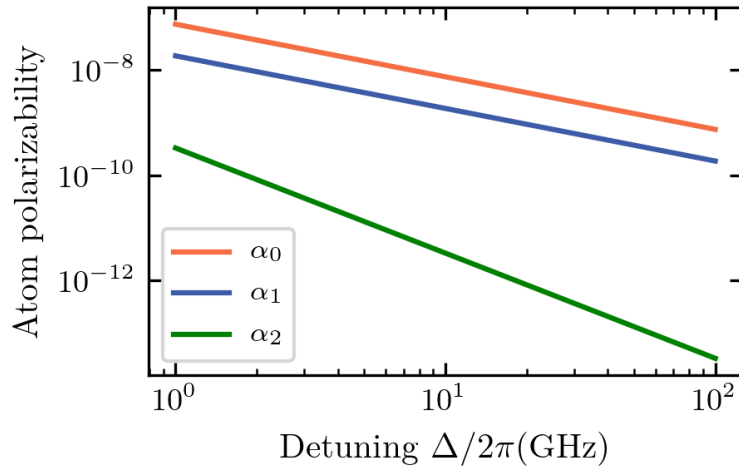
Figure 2.5: Scaling of different ranks of the atomic polarisability tensor of ^{87}Rb as a function of detuning Δ with probe waist of $w_0 = 50\ \mu$m.

polarizability scale as Δ^{-1} and the tensor polarizability scales as Δ^{-2}, respectively. Therefore, this implies that a larger detuning is favourable for the desired Faraday interaction. In this thesis, we work with typical detuning from 10 GHz to 80 GHz, which well justifies this approximation as $\alpha_1/\alpha_2 \sim 10^2 - 10^3$.

2.4 Spin decoherence mechanism

So far, we only discuss the coherent evolution of the spin light interaction, in practice, our collective spin is subjected to a multiple of decoherence mechanisms. Here, the individual decoherence mechanisms are discussed in detail below.

2.4.1 Spontaneous scattering

The predominant and most fundamental decay process is due to the photon scattering of the probe field. Suppose we are interested in studying the Faraday interaction contributed by atoms initially prepared in the ground state $|f = 2, m_f =$

$-2\rangle$. The excited atom can decay to any levels allowed by the dipole selection rule $\Delta f = 0, \pm 1$, $\Delta m_f = 0, \pm 1$. In general, this happens in two ways to an atom upon excitation [70] by any driving laser fields as shown in Fig. 2.6. First, the
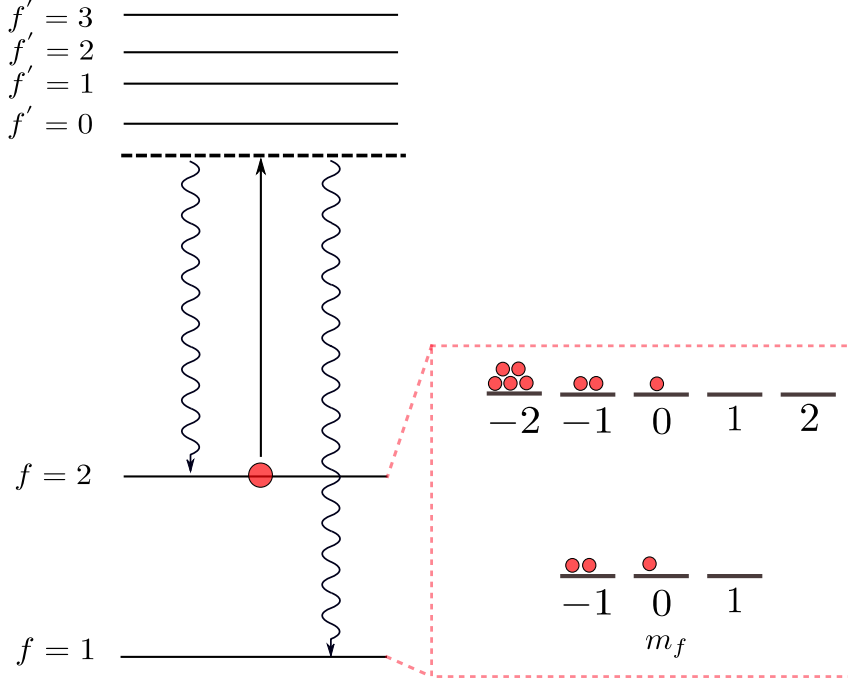
Figure 2.6: Schematic diagram of atomic decay processes induced by spontaneous scattering, the straight arrow shows the transition driven by the probe laser, the wavy arrows indicate the two possible decay processes.

excited atoms can decay into hyperfine ground state $f = 1$, for small detuning, the atom no longer participates in the interaction [70] and at the large detunings in our experiment, both $f = 2$ and $f = 1$ contribute to the Faraday signal (see Sec. 2.3 and Fig. 2.6). Another way the excited atom can decay is returning to the same hyperfine ground state $f = 2$ with a random orientation, i.e. atoms can be randomly redistributed to different m_f sublevels without leaving the $f = 2$ hyperfine manifold. This leads to a depolarization and dephasing of the collective spin (see Fig. 2.6). Both processes are due to spontaneous photon scattering and characterized by the spontaneous photon scattering rate γ_{sc} [59]:

$$\gamma_{sc} = \alpha_0 S_0 \frac{\gamma_e}{\Delta} = \frac{\sigma_\pi}{2A} \left(\frac{\gamma_e}{\Delta}\right)^2 \frac{\Phi_L}{2} \tag{2.22}$$

Similar to the tensor coupling, the photon scattering rate γ_{sc} also scaled as Δ^{-2}, whereas our desired vector polarizability scales as Δ^{-1}. Therefore, the decoherence due to spontaneous scattering is suppressed by the favourable scaling $\gamma_{sc}/\alpha_1 \sim \Delta^{-1}$ at large detunings.

2.4.2 Spin broadening due to inhomogeneous magnetic field

The spin coherence is also reduced by the inhomogeneity of the magnetic field, for example, a small uncompensated magnetic field gradient can cause a spread of Larmor frequencies across the atomic ensemble. As shown in Fig. 2.7, consider a linear magnetic gradient applied across the Gaussian spatial distribution of the atomic ensemble, if one adds up the spin oscillator signals $X_{s,i}(t)$ precessing at slightly different Larmor frequencies, an exponential decay signal is obtained. The width of the frequency spread corresponds to the inverse of the spin dephasing time T_ϕ in the absence of light. The magnetic field inhomogeneity sets the intrinsic spin linewidth $\gamma_{s,0} = 1/T_\phi$ and is negligible when spin broadening is dominated by spontaneous scattering i.e. $\gamma_s = \gamma_{s,0} + \gamma_{sc} \approx \gamma_{sc}$.
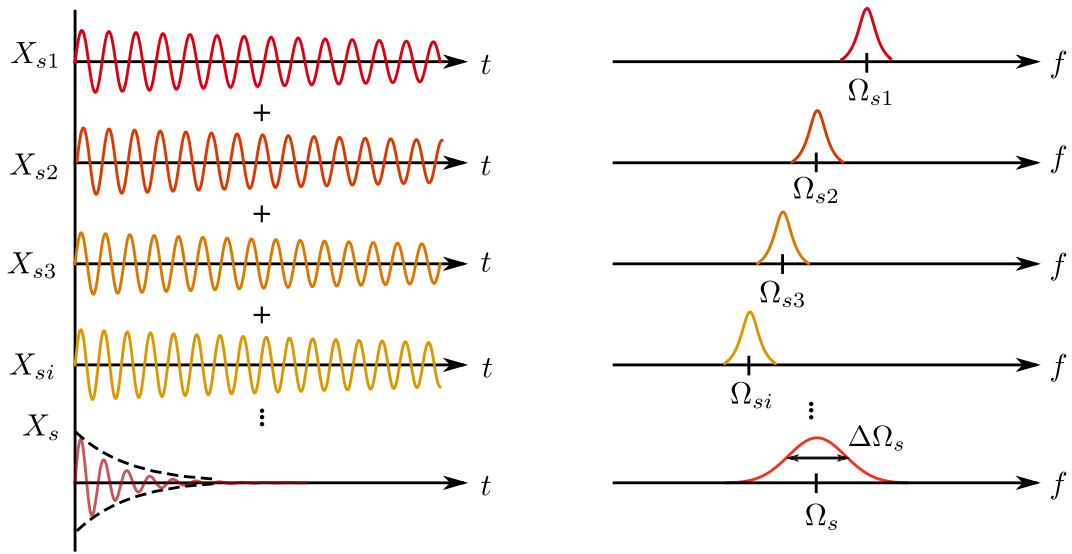
Figure 2.7: Schematic diagram of spin broadening induced by inhomogeneous magnetic field gradient. The first four pair of time and frequency data show examples X_{s1}-X_{si} where atoms at different locations with respect to a linear magnetic gradient precess at a different Larmor frequency. By summing the spin signals contributed by atoms at different locations over the continuum, this leads to dephasing of the collective spin.

2.4.3 Spin broadening due to inhomogeneous light field

Since the probe laser beam has a Gaussian spatial distribution, atoms at different locations experiences a different amount of vector or tensor light shift. Similar to the inhomogeneous broadening due to magnetic field discussed in Sec. 2.4.2, for a constant light intensity, the non-uniform intensity profile also leads to a spread of Larmor frequencies and acts as a source of dephasing mechanism.

2.5 Input-output relation

As discussed in Sec. 2.3, in the large detuning limit, the QND Faraday interaction dominates. We may now consider the collective spin (see Eq. 2.1) couples to light via the dominant Faraday interaction $H_{s,\text{int}} = \hbar\alpha_1 F_z S_z$, this allows one to map the collective spin state onto the light field via the input output relation.

$$
\begin{aligned}
S_x^{(\text{out})} &= S_x^{(\text{in})} - \alpha_1 S_y^{(\text{in})} F_z \\
S_y^{(\text{out})} &= S_y^{(\text{in})} + \alpha_1 S_x^{(\text{in})} F_z \\
S_z^{(\text{out})} &= S_z^{(\text{in})}
\end{aligned}
\tag{2.23}
$$

we see that $S_y^{(\text{out})}$ effectively reads out the F_z spin component. We also define the Faraday angle θ_F to be the rotation angle of the linearly polarized light in the lab frame. Equivalently, on the Poincáre sphere, the S_y is rotated into S_x by $2\theta_F$ around S_z [71]:

$$
\theta_F = \frac{S_y}{2\bar{S}_x} = \frac{1}{2}\alpha_1 F_z
\tag{2.24}
$$

The Faraday angle θ_F relates to the on-resonance optical depth $d_0 = N\sigma_\pi/A$ for linearly polarized light, which is an important figure of merit to quantify the strength of the spin light interaction. For an ensemble fully polarized along z, we have $F_z = 2N$,

$$
\theta_F = d_0 \frac{\gamma_e}{8\Delta}
\tag{2.25}
$$

Similarly, we may compute the equation of motion for the spin (ignoring quantum noises but including the oscillator dynamics):

$$
\begin{aligned}
\dot{F}_y(t) &= -\Omega_s F_z - \frac{\gamma_s}{2} F_y(t) + \alpha_1 F_x S_z(t) \\
\dot{F}_z(t) &= +\Omega_s F_y - \frac{\gamma_s}{2} F_z(t)
\end{aligned}
\tag{2.26}
$$

Solving the coupled equations for the spin in frequency space, we may write the steady state of the spin component F_z in response to the drive $S_z^{(\text{in})}(\omega)$,

$$
F_z(\omega) = \chi_s(\omega)\alpha_1 \bar{F}_x S_z^{(\text{in})}(\omega)
\tag{2.27}
$$

where the spin susceptibility is defined as

$$
\chi_s(\omega) = \frac{\Omega_s}{\Omega_s^2 - \omega^2 - i\gamma_s\omega}
\tag{2.28}
$$

2.6 Effect of tensor light shift on atoms

In this section, we discuss the influence of tensor interaction on the spin dynamics. As discussed in Sec. 2.3, tensor polarizability is a linear birefrigence effect, which
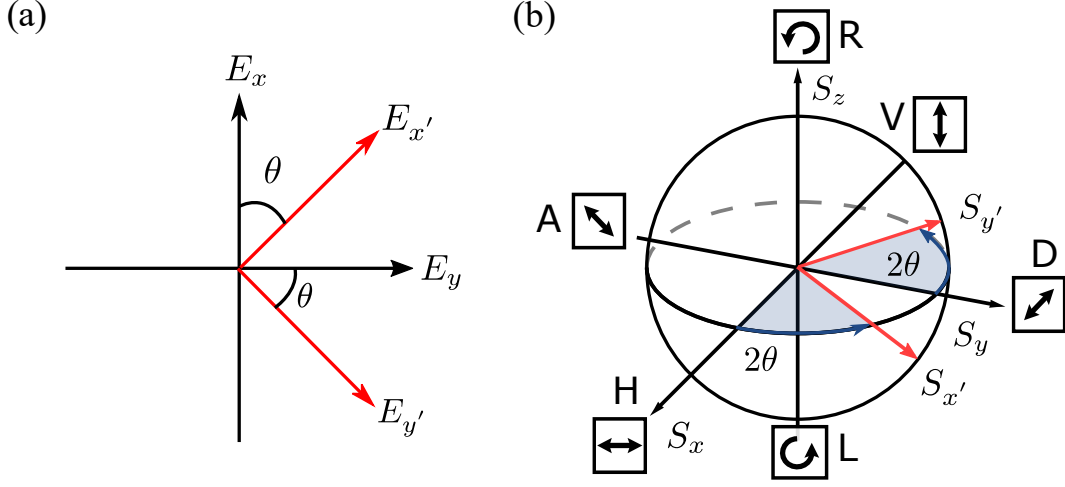
Figure 2.8: (a) Basis transformation in Jones basis. (b) Basis transformation in Stokes basis.

depends strongly on the orientation of linear polarization. For this, we define the laser polarization relative to the x-axis in the lab frame. The polarization of light can be rotated by θ (see Fig. 2.8) with the aid of a half waveplate, the positive frequency part of the electric field with input polarization θ reads

$$\mathbf{E}^{(+)} = \mathcal{E}_0 \left[a_{x'} \mathbf{e}_{x'} + a_{y'} \mathbf{e}_{y'} \right] e^{ik_L z} \tag{2.29}$$

where the polarization field operators are represented by $a_{x'} \to \sqrt{\Phi_L} + a_{x'}$ and $a_{y'}$, respectively. The corresponding basis vector for the x-polarized local oscillator along $\mathbf{e}_x$ and the y- polarized quantum field along $\mathbf{e}_y$ transform as $\mathbf{e}_{x'} = \cos(\theta)\mathbf{e}_x + \sin(\theta)\mathbf{e}_y$ and $\mathbf{e}_{y'} = -\sin(\theta)\mathbf{e}_x + \cos(\theta)\mathbf{e}_y$, respectively. Under the basis rotation, the stokes vectors transform accordingly,

$$\begin{aligned}
S_x &= +\cos(2\theta)S_{x'} - \sin(2\theta)S_{y'} \\
S_y &= +\cos(2\theta)S_{y'} + \sin(2\theta)S_{x'}
\end{aligned} \tag{2.30}$$

where the prime variable refer to the stokes vector fixed to the frame of laser field. For convenience, from here onward, we consider the spin light interaction in the rotated polarization basis and we drop the prime variable of the rotated stokes operator. Here, the input field has a strong coherent amplitude along the rotated linear polarization $\langle S_x \rangle \approx \bar{S}_0 = \Phi_L/2$ and $\langle S_y \rangle = \langle S_z \rangle = 0$. Here, $f_x \approx -f$, where the well-oriented atom aligns opposite to the magnetic field along the positive x direction. Following the derivation in [59], the tensor Hamiltonian from Eq. 2.19 can be simplified to

$$H^{(2)} = \hbar\alpha_2 \left[(\frac{3\cos(2\theta)+1}{2}) f_x^2 \bar{S}_0 + (1-2f)f_y \left[\cos(2\theta)S_y + \sin(2\theta)S_x \right] \right] \tag{2.31}$$

19

The first term inside the bracket corresponds to a quadratic splitting $\hbar\delta\Omega_2 m_f^2$ of the Zeeman sublevels due to the tensor light shift

$$\delta\Omega_2 = \alpha_2 \bar{S}_0 \frac{3\cos(2\theta) + 1}{2} \tag{2.32}$$

Since the quadratic shift $\delta\Omega_2$ is proportional to laser intensity $\bar{S}_0$, and the atoms are distributed across the non-uniform laser beam profile, this induces inhomogeneous spin broadening as discussed previously in Sec. 2.4.3. Therefore we typically work with $\theta \approx 55°$ with respect to the magnetic field where $3\cos(2\theta) + 1 \approx 0$ to minimize the inhomogeneous spin broadening due to tensor effect. We remark that it is possible use the quadratic Zeeman tensor shift to cancel out the quadratic Zeeman shift induced by large biased magnetic field [72], however, this can induce spatial inhomogeneities due to spatial dependence of S_0. Finally, to gain intuition of the dynamics generated by the tensor Hamiltonian, it is insightful to write down the input-output relation generated from the last term $\hbar\alpha_2(1 - 2f)f_y(\cos(2\theta)S_y + \sin(2\theta)S_x)$ of the tensor Hamiltonian Eq. 2.31 in addition to the Faraday interaction:

$$
\begin{aligned}
S_x^{(\text{out})} &= S_x^{(\text{in})} - \alpha_1 F_z S_y^{(\text{in})} + \alpha_2(1 - 2f)F_y \cos(2\theta)S_z^{(\text{in})} \\
S_y^{(\text{out})} &= S_y^{(\text{in})} + \alpha_1 F_z S_x^{(\text{in})} - \alpha_2(1 - 2f)F_y \sin(2\theta)S_z^{(\text{in})} \\
S_z^{(\text{out})} &= S_z^{(\text{in})} - \alpha_2 F_y(1 - 2f)[\cos(2\theta)S_x^{(\text{in})} - \sin(2\theta)S_y^{(\text{in})}]
\end{aligned}
\tag{2.33}
$$

First, the $\cos(2\theta)S_y$ term in Eq. 2.31 causes a rotation in S_x-S_z plane, this opens up a noise channel that allows the technical amplitude noise of the laser to couple to the circular component S_z that drives the spin. Whereas, the $\sin(2\theta)S_x$ term in Eq. 2.31 corresponds to a linear birefringence effect, which rotates the stokes vector in S_y-S_z plane. Due to Faraday rotation, the imprinted spin signal $S_y^{(\text{out})} \propto F_z$ can be converted back to S_z that started the Faraday interaction. For the spin side, the observable of interest F_z is rendered non-QND as $S_z^{(\text{out})} \neq S_z^{(\text{in})}$. For the above arguments, it is reasonable apply a large atom-light detuning to suppress the higher order dynamics which violates the simple Faraday interaction picture.

2.7 Non-uniform atom-light interaction

In the previous sections, we considered the idealized case where the probe laser beam uniformly couples to the atomic ensemble. However, in reality, both the probe laser beam and the atomic ensemble are described by their individual spatial mode functions. Moreover, to enhance the spin-light interaction strength, the laser beam is typically focused to a waist size comparable to the transverse waist of the atomic ensemble, this means non-uniform coupling would occur since the light field is not uniform across the volume occupied by the atoms. To gain a better intuition, we illustrate the role of non-uniform coupling with various examples of

probe-atom geometries as shown in Fig. 2.9 [73]. In Fig. 2.9(a), the mode matching is poor, due to the large 4π solid angle of the light scattered from the atoms, only a small portion of light scatters back into the paraxial mode in the forward axis parallel to the propagation axis. Fig. 2.9(b) contains an uniform slab of atoms interacts with the light but the optical depth is very small, only Fig. 2.9(c) and (d) that compromise between the optical depth and mode matching maximizes the efficiency of the atom light coupling. To take the above mode matching into account, we follow the theoretical framework in [74] to describe the non-uniform coupling between the probe mode and the ensemble mode.

(a)   (b)

(c)   (d)
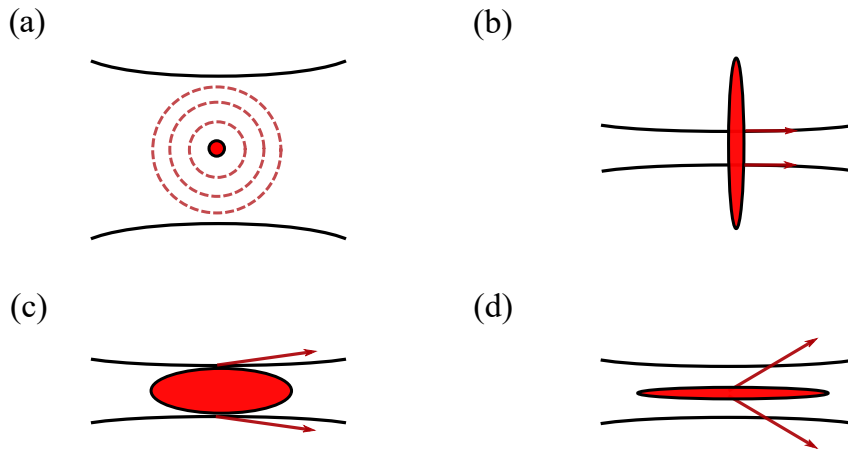
Figure 2.9: Schematic diagram of various probe-atom geometries. The red solid lines indicate the scattered mode whereas the black solid line corresponds to the spatial profile of the probe mode. (a) A point like atomic ensemble that scatters in all directions (b) A thin disk cloud that radiates into the probe mode but the OD is small. (c) The pencil shaped atomic ensemble match well or (d) poor [adapted from [73]]

First, we introduce the modified Faraday Hamiltonian that generalizes our uniform spin-light Hamiltonian [1] to the non-uniform coupling case [74]:

$$\tilde{H}_{\text{int},s} = \hbar \alpha_1 \Sigma_{i=1}^{N} \eta_s^{(i)} f_z^{(i)} S_z \tag{2.34}$$

where each atom couples to the probe laser field with a weighting coefficient $\eta_s^{(i)}$, proportional to the local intensity each individual atom sees. In this formulation, the α_1 is defined such that the weighting coefficient $\eta_s^{(i)} = 1$ evaluated at the peak intensity of the optical mode function, where $\max(u(r)) = 1$ and the mode area A is defined as the integral over the spatial mode function

$$A = \int \int |u(r)|^2 d^2 r \tag{2.35}$$

---

[1]The word "generalizes" is used here, because the framework includes the simple case of uniform atom-light coupling if we simply set the weight coefficient to 1 (see equation below)

As an example, the vector polarizability that defined previously for the uniform coupling description lies within the non-uniform coupling theory. There the spatial mode of the probe is a flat top-hat spatial mode function $\alpha_1 = \frac{1}{8A}\frac{\lambda^2}{\pi}\frac{\gamma_e}{\Delta}$ where $A = \int_0^{2\pi}\int_0^{\infty}\mathbf{1}\,[0,w_0]\,(r)r dr d\phi = \pi w_0^2$ where w_0 is the beam radius. The spin operators are replaced by the effective spin operators which is defined as [74]:

$$\tilde{F}_\alpha = \Sigma_i \frac{\eta_s^{(i)}}{\eta_{\text{eff}}} f_\alpha^{(i)} \tag{2.36}$$

, where $f_\alpha^{(i)}$ is the single hyperfine spin operator of the i th atom, where $\alpha = x, y, z$. To preserve the spin commutation relation and Heisenberg uncertainty principle, i.e. $[\tilde{F}_y, \tilde{F}_z] = i\hbar\tilde{F}_x$, the effective coupling strength η_{eff} is introduced as

$$\eta_{\text{eff}} = \frac{\Sigma_i \eta_s^{(i)2}/N}{\Sigma_i \eta_s^{(i)}/N} = \frac{\langle \eta_s^2 \rangle}{\langle \eta_s \rangle} \tag{2.37}$$

where the usual commutation relation between uncorrelated individual spins was assumed:

$$[f_l^{(k)}, f_m^{(j)}] = i\epsilon_{lmn}\delta_{kj}f_n^{(k)} \tag{2.38}$$

, where ϵ_{lmn} is the Levi-Civita symbol. One can also write the above Hamiltonian Eq. 2.34 in a form equivalent to the uniform coupling case [74]:,

$$\tilde{H}_{\text{int,s}} = \hbar\tilde{\alpha}_1 \tilde{F}_z S_z \tag{2.39}$$

where the effective coupling strength η_{eff} is now absorbed into our effective vector polarizability, i.e. $\tilde{\alpha}_1 = \eta_{\text{eff}}\alpha_1$, and the light is now coupled to the z-component of the effective spin. In this description, we may see the N atoms coupled to the light mode η_i locally amounts to an effective spin uniformly coupled to the light with effective coupling strength reduced by η_{eff} and a reduced spin length $|\bar{\tilde{F}}_x| = N_e \bar{f}_x \approx N_e f$, where the effective atom number N_e is defined as,

$$N_e = \frac{\Sigma_i \eta_s^{(i)}}{\eta_{\text{eff}}} = \frac{\langle \eta_s \rangle}{\eta_{\text{eff}}} N \tag{2.40}$$

here we assumed a well-polarized spin ensemble $f_x^{(i)} = f_x \approx f \forall i$. Analogous to the uniform coupling case, if the macroscopic effective spin component is large compared to the transverse spin components, i.e. $|\bar{\tilde{F}}_x| \approx N_e f \gg \langle F_y \rangle, \langle F_z \rangle$ (i.e. where H.P.A holds) [74], we may treat the effective spin $\tilde{F}$ as a harmonic oscillator, and introduce the position and momentum quadrature for the inhomogeneous spin wave:

$$\tilde{X}_s = \frac{\tilde{F}_z}{\sqrt{\bar{\tilde{F}}_x}} = \frac{1}{\sqrt{f\Sigma_{i=1}^N \eta_s^{(i)2}}}\Sigma_{i=1}^N \eta_s^{(i)} f_z^{(i)} \tag{2.41}$$

$$\tilde{P}_s = \frac{\tilde{F}_y}{\sqrt{\tilde{F}_x}} = \frac{1}{\sqrt{f \Sigma_{i=1}^{N} \eta_s^{(i)2}}} \Sigma_{i=1}^{N} \eta_s^{(i)} f_y^{(i)} \tag{2.42}$$

, which satisfies the usual commutation relation for $f_x^{(i)} = f_x = f \forall i$:

$$[\tilde{X}_s, \tilde{P}_s] = i \frac{1}{f \Sigma_{i=1}^{N} \eta_s^{(i)2}} \Sigma_{i=1}^{N} \eta_s^{(i)2} f_x^{(i)} \approx i \tag{2.43}$$

With the modified Faraday Hamiltonian Eq. 2.39, the input-output relation and Faraday angle are now defined in terms of effective spin operator and vector polarizability [c.f. Eq. (2.24) and Eq. (2.23)]:

$$S_y^{(\text{out})} = S_y^{(\text{in})} + \tilde{\alpha}_1 \tilde{F}_z S_x^{(\text{in})} \tag{2.44}$$

$$\theta_F = \frac{\langle S_y^{(\text{out})} \rangle}{2 \bar{S}_x} = \frac{1}{2} \tilde{\alpha}_1 \tilde{F}_z \tag{2.45}$$

where $\tilde{\alpha}_1 = \eta_{\text{eff}} \alpha_1$. For a $f = 2$ spin ensemble fully polarized along z, i.e. $\tilde{F}_z = N_e f = \frac{\langle \eta_s \rangle}{\eta_{\text{eff}}} N f$, the Faraday angle reads[2]:

$$\theta_F = \frac{1}{2} \tilde{\alpha}_1 \tilde{F}_z = \alpha_1 \langle \eta_s \rangle N \tag{2.46}$$

We can apply the same formalism to derive the effective spin measurement rate. Starting from the modified Faraday Hamiltonian Eq. 2.34, each spin obeys the following equation of motion under the non-uniform coupling description:

$$\frac{df_y^{(i)}(t)}{dt} = -\Omega_s f_z^{(i)}(t) - \frac{\gamma_s}{2} f_y^{(i)}(t) + \mathfrak{f}_y^{(i)}(t) + \alpha_1 \eta_s^{(i)} f_x^{(i)}(t) S_z(t) \tag{2.47}$$

$$\frac{df_z^{(i)}(t)}{dt} = \Omega_s f_y^{(i)}(t) - \frac{\gamma_s}{2} f_z^{(i)}(t) + \mathfrak{f}_z^{(i)}(t) \tag{2.48}$$

where the first term on the R.H.S is the Larmor precession of the spin around the x axis and γ_s describes the spin damping, the Langevin forces $\mathfrak{f}_y$ and $\mathfrak{f}_z$ are included to preserve the noise statistics in presence of the damping term. By performing

---

[2]In general, for non-uniform coupling, $0 \leq \langle \eta_s \rangle \leq 1$. One can see that if we assume uniform coupling, i.e. $\langle \eta_s \rangle = 1$, we recover the vector polarizability equation (see Eq. 2.18) for the uniform coupling case.

Fourier transform on both sides, we can solve the above coupled equations in the Fourier domain:

$$f_z^{(i)}(\omega) = \frac{(\frac{\gamma_s}{2} - i\omega)f_z^{(i)}(\omega) + \Omega_s[f_y^{(i)}(\omega) + \alpha_1\eta_s^{(i)}f_x^{(i)}S_z(\omega)]}{(\Omega_s^2 - \omega^2) + (\frac{\gamma_s}{2})^2 - i\gamma_s\omega} \tag{2.49}$$

Substituting the solution into the input-output relation for the output field $S_y^{(\text{out})}(\omega)$, we obtain the symmetrized power spectral density under the non-uniform coupling description:

$$S_y^{(\text{out})}(\omega) = S_y^{(\text{in})}(\omega) + \alpha_1\bar{S}_x\Sigma_{i=1}^N\eta_s^{(i)}\frac{(\frac{\gamma_s}{2} - i\omega)f_z^{(i)}(\omega) + \Omega_s[f_y^{(i)}(\omega) + \alpha_1\eta_s^{(i)}f_x^{(i)}S_z(\omega)]}{(\Omega_s^2 - \omega^2) + (\frac{\gamma_s}{2})^2 - i\gamma_s\omega} \tag{2.50}$$

Before we compute the noise spectrum of the output field, we write down the noise properties for the input coherent state of light field [75],

$$\left\langle S_y^{(\text{in})}(\omega)S_y^{(\text{in})}(\omega')\right\rangle = \left\langle S_z^{(\text{in})}(\omega)S_z^{(\text{in})}(\omega')\right\rangle = \delta(\omega + \omega')\frac{\bar{S}_x}{2} \tag{2.51}$$

and for spin coherent state, respectively [75]:

$$\begin{aligned}
\left\langle f_y^{(i)}(\omega)f_y^{(j)}(\omega')\right\rangle &= +\left\langle f_z^{(i)}(\omega)f_z^{(j)}(\omega')\right\rangle = \delta(\omega + \omega')\delta_{ij}\frac{\gamma_s}{2}\left|\bar{f}_x^{(i)}\right| \\
\left\langle f_y^{(i)}(\omega)f_z^{(j)}(\omega')\right\rangle &= -\left\langle f_z^{(i)}(\omega)f_y^{(j)}(\omega')\right\rangle = \delta(\omega + \omega')\delta_{ij}i\frac{\gamma_s}{2}|\bar{f}_x^{(i)}|
\end{aligned} \tag{2.52}$$

Assuming $f_x^{(i)}(\omega) = \bar{f}_x$, the symmetrized power spectral density of the output field $S_y^{(\text{out})}(\omega)$ reads:

$$\bar{S}_{S_yS_y}(\omega) = \frac{\bar{S}_x}{2} + \frac{(\alpha_1\bar{S}_x)^2}{[(\Omega_s - \omega)(\Omega + \omega) + (\frac{\gamma_s}{2})^2] + (\gamma_s\omega)^2}\left[\Sigma_{j=1}^N(\frac{\gamma^2}{4} + \omega^2 + \Omega_s^2)\frac{\gamma_s}{2}\frac{\bar{S}_x}{2}\eta_s^{(j)2}\bar{f}_x^{(i)}\bar{f}_x^{(j)}\right] \tag{2.53}$$

$$\bar{S}_{S_yS_y}(\omega) \approx \frac{\bar{S}_x}{2} + \frac{(\frac{1}{2}\alpha_1\bar{S}_x)^2}{(\Omega_s - \omega)^2 + (\frac{\gamma_s}{2})^2}\left[\Sigma_{j=1}^N\gamma_s\eta_s^{(j)2}|\bar{f}_x^{(j)}| + \frac{1}{2}\Sigma_{i=1}^N\Sigma_{j=1}^N\alpha_1^2\eta_s^{(i)2}\eta_s^{(j)2}\bar{f}_x^{(i)}\bar{f}_x^{(j)}\bar{S}_x\right] \tag{2.54}$$

where in the second line, we applied the narrow band approximation, this approximation holds well if we have a high-frequency oscillator with a narrow spin linewidth, i.e. $\frac{\gamma_s}{2}, |\Omega_s - \omega| \ll \Omega_s$.

The form of Eq. 2.54 suggests one to define an effective spin operators of higher order moment in a similar way to the theoretical treatment in [73], the effective spin operators of higher order moments are defined as:

$$\tilde{F} \rightarrow \tilde{F}^{(n)} = \Sigma_{i=1}^N(\frac{\eta_s^{(i)}}{\eta_{\text{eff}}})^n f^{(i)} \tag{2.55}$$

while we still have:

$$\alpha_1 \to \tilde{\alpha}_1 = \alpha_1 \eta_{\text{eff}} \tag{2.56}$$

With this generalization, we may write Eq. 2.39 as

$$\tilde{H}_{\text{int,s}} = \hbar \tilde{\alpha}_1 \tilde{\bar{F}}_z^{(1)} S_z \tag{2.57}$$

the symmetrized power spectral density of the output field (see Eq. 2.54) can then be expressed in terms of the effective spin operators of the second order moment:

$$\bar{S}_{S_y S_y}(\omega) \approx \frac{\bar{S}_x}{2} + \frac{(\frac{1}{2}\tilde{\alpha}_1 \bar{S}_x)^2}{(\Omega_s - \omega)^2 + (\frac{\gamma_s}{2})^2}\left[\gamma_s|\tilde{\bar{F}}_x^{(2)}| + \frac{1}{2}\Sigma_{i=1}^N \Sigma_{j=1}^N \tilde{\alpha}_1^2 (\tilde{\bar{F}}_x^{(2)})^2 \bar{S}_x\right] \tag{2.58}$$

Assuming we can prepare identical spins i.e. $f_x^{(i)} = f_x = f \forall i$, the first and second order spin operators are equivalent:

$$\tilde{\bar{F}}_x^{(2)} = \Sigma_{i=1}^N (\frac{\eta_s^{(i)}}{\eta_{\text{eff}}})^2 f^{(i)} = \frac{1}{\eta_{\text{eff}}^2} N f \langle \eta_s^2 \rangle = \frac{\langle \eta_s \rangle}{\eta_{\text{eff}}} N f = N_e f = \tilde{\bar{F}}_x^{(1)} \tag{2.59}$$

We may define an effective spin measurement rate as

$$\tilde{\Gamma}_s := \tilde{\Gamma}_s^{(2)} = \frac{\tilde{\alpha}_1^2 \bar{S}_x \tilde{\bar{F}}_x^{(2)}}{4} = \frac{\tilde{\alpha}_1^2 \bar{S}_x N_e f}{4} = \tilde{\Gamma}_s^{(1)} \tag{2.60}$$

for $\tilde{\bar{F}}_x^{(2)} = \tilde{\bar{F}}_x^{(1)}$.

$$\tilde{\Gamma}_s = \frac{\tilde{\alpha}_1^2 \bar{S}_x N_e f}{4} = \langle \eta_s \rangle \eta_{\text{eff}} \frac{\alpha_1^2 \bar{S}_x N f}{4} = \langle \eta_s^2 \rangle \Gamma_s \tag{2.61}$$

Similarly, if we compare to the uniform coupling case, we see that the effective spin measurement rate is simply rescaled by $\langle \eta_s^2 \rangle$. With this definition of the effective spin measurement rate and the effective spin quadratures we introduced earlier (see Eq. 2.41 and Eq. 2.42), we can write the Faraday Hamiltonian (see Eq. 2.39) in the Holstein Primakoff approximation i.e. $\tilde{H}_{\text{int,s}} = \hbar\sqrt{\tilde{\Gamma}_s}\tilde{X}_s P_L$ within the non-uniform coupling framework.

Application of the non-uniform coupling model

As we see later in Chapter 3, the non-uniform coupling model is applied to predict the vector polarizability and measurement rate when the probe and atomic waist have different transverse sizes. Here, by making simple assumptions of the probe-atom geometry, we may derive the analytical form of the Faraday angle and measurement rate in the non-uniform coupling framework. Here, we study the two common intensity profiles for the probe beam using Eq. 2.35,

For a flat top hat intensity profile $\eta_s(r) = \mathbf{1}[0, w_0](r)$:

$$A = \int_0^{2\pi} \int_0^\infty \mathbf{1}[0, w_0](r) r dr d\phi = \pi w_0^2 \tag{2.62}$$

where w_0 is the beam radius. We recover the result for the uniform coupling description. In our experiment, the probe beam is given by the fundamental transverse mode (TEM$_{00}$), the intensity profile takes the form of a Gaussian distribution $\eta_s(r) = |u_{00}(r)|^2 = \exp(-2r^2/w_0^2)$,

$$A = \int_0^{2\pi} \int_0^\infty |u_{00}(r)|^2 r dr d\phi = \frac{\pi w_0^2}{2} \tag{2.63}$$

where w_0 corresponds to the beam waist. Note that here we compute using only the waist at $z = 0$, this is a very good approximation as long as the rayleigh range of the probe beam is large compared to the length of the atomic cloud.

For the spatial mode of the atomic ensemble:

$$n(r,z) = \frac{N}{V_0} \exp\left(-2\frac{r^2}{w_a^2}\right) \mathbf{1}\left[\frac{-L_0}{2}, \frac{L_0}{2}\right](z) \tag{2.64}$$

we can assume the atoms are uniformly distributed in the z-direction, where $V_0 = L_0 \pi w_a^2/2$ is the volume that encloses the atomic ensemble. Going to a continuous description, the average over a quantity $\langle Q \rangle$ can be obtained by computing the overlap integral between the atomic and probe mode, i.e. $\langle Q \rangle = \Sigma Q/N \rightarrow \frac{1}{N} \int d^3 r n(r) Q(r)$. We get

$$\langle \eta_s \rangle = \frac{w_0^2}{w_0^2 + w_a^2} = \frac{1}{1 + \sigma^2} \tag{2.65}$$

$$\langle \eta_s^2 \rangle = \frac{w_0^2}{w_0^2 + 2w_a^2} = \frac{1}{1 + 2\sigma^2} \tag{2.66}$$

$$\eta_{\text{eff}} = \frac{w_0^2 + w_a^2}{w_0^2 + 2w_a^2} = \frac{1 + \sigma^2}{1 + 2\sigma^2}, \tag{2.67}$$

where $\sigma = w_a/w_0$, in the limit, $\sigma \rightarrow 0$ where $w_a \rightarrow 0$, we get $\langle \eta_s \rangle = 1, \langle \eta_s^2 \rangle = 1, \eta_{\text{eff}} = 1$, (equivalent to the uniform case). Whereas, in the opposite limit where $\sigma \rightarrow \infty, w_a \gg w_0$, we get $\langle \eta_s \rangle = 0, \langle \eta_s^2 \rangle = 0, \eta_{\text{eff}} = \frac{1}{2}$, effective coupling. In the perfect mode-matching case $\sigma = 1$, we get $\langle \eta_s \rangle = \frac{1}{2}$, $\langle \eta_s^2 \rangle = \frac{1}{3}$ and $\eta_{\text{eff}} = \frac{\langle \eta_s^2 \rangle}{\langle \eta_s \rangle} = \frac{2}{3}$. The results are summarized below

$$0 \leq \langle \eta_s \rangle \leq 1 \tag{2.68}$$

$$0 \leq \langle \eta_s^2 \rangle \leq 1 \tag{2.69}$$

$$\frac{1}{2} \leq \eta_{\text{eff}} \leq 1 \tag{2.70}$$

$$0 \leq N_e \leq N \tag{2.71}$$

To sum up, we see that the above results indeed reconcile with the intuitive picture that the N atoms coupled to the light mode η_i can be understood as an effective spin with reduced spin length ($N_e \leq N$) uniformly coupled to the light with effective coupling strength reduced by $\eta_{\text{eff}} \leq 1$ as mentioned in the beginning of this section. The non-uniform coupling model provides one a more accurate description to predict the measurement rate since possible mismatch between the probe and the ensemble mode is also taken into consideration.

2.8 Quantum regime of spin light interface

Probing into the quantum regime of the spin oscillator using light highlights an example of a profound research effort in the field of quantum sensing [12], quantum metrology [40] and gravitational wave detection [52,76]. Here, we present the theoretical model to identify the different noise processes in a quantum-limited measurement and discuss the consequences of the polarization squeezing of light using spin. Before diving into the quantum limits of spin light interface, we briefly revisit the main concepts in the language of standard quantum limit measurement.

Quantum non-demolition measurement and backaction evasion

Quantum non-demolition measurement [77,78] states that a system observable O_s that we want to measure should not be altered by the free evolution of its intrinsic spin oscillator Hamiltonian. In quantum mechanics language,

$$\frac{\mathrm{d}}{\mathrm{d}t}O_s(t) = -\frac{i}{\hbar}\left[H_{s,0}, O_s\right] = 0 \tag{2.72}$$

or equivalently the operators for different times t_i, t_j must satisfy

$$\left[O_s(t_i), O_s(t_j)\right] = 0 \tag{2.73}$$

There are two perspectives to this problem. If one measures in the laboratory frame, it is clear that the spin amplitude quadrature X_s does not satisfy the above requirement (Eq. 2.73)

$$\dot{X}_s = -\frac{i}{\hbar}\left[H_{s,0}, X_s\right] = \Omega_s P_s \tag{2.74}$$

as the observable evolves under its free evolution. However, a closer look at the commutation relation between $X_s(t)$ and $X_s(t+\tau)$

$$[X_s(t), X_s(t+\tau)] = i\sin(\Omega_s\tau), \quad [P_s(t), P_s(t+\tau)] = i\sin(\Omega_s\tau) \tag{2.75}$$

suggests that Eq. 2.73 condition is satisfied for integer multiple of half periods $\tau = n\pi/\Omega_s$, where $n \in \mathbb{Z}$. Therefore, for a harmonic oscillator in lab frame, (X_s, P_s) are

called stroboscopic QND variables. Here we introduce the spin measurement rate $\Gamma_s = \alpha_1^2 \bar{F}_x \bar{S}_x / 4$, as discussed in Sec. 2.5, the Faraday interaction $H_{s,\text{int}} = \hbar \alpha_1 F_z S_z = \hbar 2 \sqrt{\Gamma_s} X_s P_L$ is called the QND interaction for a different reason but a similar one, the interaction is QND in the sense that the original pair of spin light quadratures X_s, P_L remain unchanged after the interaction given by input-output relation. The spin and light quadrature $P_s^{(\text{out})}$, $X_L^{(\text{out})}$ become entangled,

$$\dot{X}_s = \Omega_s P_s \tag{2.76}$$

$$\dot{P}_s = -\Omega_s X_s - 2\sqrt{\Gamma_s} P_L^{(\text{in})} \tag{2.77}$$

$$X_L^{(\text{out})} = X_L^{(\text{in})} + 2\sqrt{\Gamma_s} X_s^{(\text{in})} \tag{2.78}$$

$$P_L^{(\text{out})} = P_L^{(\text{in})} \tag{2.79}$$

For an efficient read out of the spin quadrature using light, we want the measured observable to be imprinted on the light meter undisturbed with $[H_{s,\text{int}}, X_L] \neq 0$. The measured observable X_s commutes with the QND interaction Hamiltonian remains unchanged is known as back-action evading (BAE),

$$[X_s, H_{s,\text{int}}] = [X_s, 2\hbar\sqrt{\Gamma_s} X_s P_L] = 0 \tag{2.80}$$

whereas the conjugate variable of the measured quadrature is disturbed as a result of the measurement $[H_{s,\text{int}}, P_s] \neq 0$ in accordance to Heisenberg principle.

Quantum backaction

Consider a weak continuous measurement of the spin quadrature using light as a meter. Due to Faraday effect, the spin position quadrature X_s is mapped onto the light quadrature $X_L^{(\text{out})}$, simultaneously, the measurement leads to random perturbation on the spin momentum P_s (see sec. 2.8) as discussed above. Therefore, the term $2\sqrt{\Gamma_s} P_L^{(\text{in})}$ in Eq. 2.77 is known as the quantum backaction (QBA) term [75]. Due to the oscillator dynamics of the spin oscillator, the uncertainty in momentum P_s is then rotated into uncertainty X_s every quarter of a period which then induces backaction noise onto the meter. One can see the role of backaction more clearly in the rotating frame, the rotating frame ($\tilde{X}_s$, $\tilde{P}_s$) relate to the lab frame operators (X_s, P_s) as follows

$$\tilde{X}_s(t) = +X_s(t)\cos(\Omega_s t) - P_s(t)\sin(\Omega_s t) \tag{2.81}$$

$$\tilde{P}_s(t) = +X_s(t)\sin(\Omega_s t) + P_s(t)\cos(\Omega_s t) \tag{2.82}$$

The equation of motion for the spin reads [75]:

$$\dot{\tilde{X}}_s = +2\sqrt{\Gamma_s} P_L^{(\text{in})}\sin(\Omega_s t) \tag{2.83}$$

$$\dot{\tilde{P}}_s = -2\sqrt{\Gamma_s} P_L^{(\text{in})}\cos(\Omega_s t) \tag{2.84}$$

and the input-output relation in the rotating frame reads:

$$X_L^{(\text{out})} = X_L^{(\text{in})} + 2\sqrt{\Gamma_s}\left[\tilde{X}_s^{(\text{in})}\cos(\Omega_s t) + \tilde{P}_s^{(\text{in})}\sin(\Omega_s t)\right] \tag{2.85}$$

$$P_L^{(\text{out})} = P_L^{(\text{in})} \tag{2.86}$$

In the rotating frame, the role of momentum P_s and position X_s becomes more symmetric, as the role of the rotating frame spin variable is alternated between X_s and P_s every $\pi/2$ cycle. Therefore, the added noise due to backaction i.e. $2\sqrt{\Gamma_s}P_L^{(\text{in})}$ affects both $\tilde{X}_s$ and $\tilde{P}_s$ which eventually enters our measurement in $X_L^{(\text{out})}$.

2.9 Quantum limits

We may discuss the theoretical model that describes quantum noise for our spin light interface. To compute the noise spectrum of the output field, we may start from input output relation of the light field (Eq. 2.23), neglecting the tensor interaction:

$$\begin{aligned} S_y^{(\text{out})}(t) &= S_y^{(\text{in})}(t) + \alpha_1 F_z(t)S_x^{(\text{in})} \\ S_z^{(\text{out})}(t) &= S_z^{(\text{in})}(t) \end{aligned} \tag{2.87}$$

and the equation of motion for the spin, where the oscillator dynamics and noise $\mathfrak{f}_y$, $\mathfrak{f}_z$ of the spin are now included[3] (c.f. Eq. 2.26),

$$\begin{aligned} \dot{F}_y(t) &= -\Omega_s F_z(t) - \frac{\gamma_s}{2}F_y(t) + \mathfrak{f}_y(t) + \alpha_1 \bar{F}_x S_z^{(\text{in})}(t) \\ \dot{F}_z(t) &= +\Omega_s F_y(t) - \frac{\gamma_s}{2}F_z(t) + \mathfrak{f}_z(t) \end{aligned} \tag{2.88}$$

We may solve the above coupled equations readily in the frequency domain. After performing Fourier transform on both sides, we obtain:

$$-i\omega F_y(\omega) = -\Omega_s F_z(\omega) - \frac{\gamma_s}{2}F_y(\omega) + \mathfrak{f}_y(\omega) + \alpha_1 \bar{F}_x S_z^{(\text{in})}(\omega) \tag{2.89}$$

$$-i\omega F_z(\omega) = +\Omega_s F_y(\omega) - \frac{\gamma_s}{2}F_z(\omega) + \mathfrak{f}_z(\omega) \tag{2.90}$$

From these equations, by expressing F_y in terms of F_z and substitute into Eq. 2.90, we get the following expression for F_z as given in [75]:

$$F_z(\omega) = \frac{(\frac{\gamma_s}{2} - i\omega)\mathfrak{f}_z(\omega) + \Omega_s\left[\mathfrak{f}_y(\omega) + \alpha_1 \bar{F}_x S_z^{(\text{in})}(\omega)\right]}{(\Omega_s - \omega)(\Omega_s + \omega) + (\frac{\gamma_s}{2})^2 - i\gamma_s\omega} \tag{2.91}$$

Similarly, we may perform Fourier transform on both sides for Eq. 2.87 and insert the expression for $F_z(\omega)$:

$$S_y^{(\text{out})}(\omega) = S_y^{(\text{in})}(\omega) + \alpha_1 \bar{S}_x \frac{(\frac{\gamma_s}{2} - i\omega)\mathfrak{f}_z(\omega) + \Omega_s\left[\mathfrak{f}_y(\omega) + \alpha_1 \bar{F}_x S_z^{(\text{in})}(\omega)\right]}{(\Omega_s - \omega)(\Omega_s + \omega) + (\frac{\gamma_s}{2})^2 - i\gamma_s\omega} \tag{2.92}$$

---

[3]not to be confused with single spin operators

Before we compute the noise spectrum of the output field, we write down the noise properties for the input coherent state of light field [75],

$$\left\langle S_y^{(in)}(\omega) S_y^{(in)}(\omega') \right\rangle = \left\langle S_z^{(in)}(\omega) S_z^{(in)}(\omega') \right\rangle = \delta(\omega + \omega') \frac{\bar{S}_x}{2} \qquad (2.93)$$

and for coherent spin state, respectively [75]:

$$\begin{aligned} \langle f_y(\omega) f_y(\omega') \rangle &= + \langle f_z(\omega) f_z(\omega') \rangle = \delta(\omega + \omega') \frac{\gamma_s}{2} |\bar{F}_x| \\ \langle f_y(\omega) f_z(\omega') \rangle &= - \langle f_z(\omega) f_y(\omega') \rangle = \delta(\omega + \omega') i \frac{\gamma_s}{2} |\bar{F}_x| \end{aligned} \qquad (2.94)$$

The noise power spectral density of the output field is simply given by Wiener Khinchin theorem [79, 80]:

$$S_{S_y S_y}(\omega) = \int_{-\infty}^{\infty} \left\langle S_y^{(out)\dagger}(-\omega) S_y^{(out)}(\omega') \right\rangle d\omega' = \int_{-\infty}^{\infty} \left\langle S_y^{(out)}(\omega) S_y^{(out)}(\omega') \right\rangle d\omega' \qquad (2.95)$$

We may therefore compute the symmetrized power spectral density i.e. $\bar{S}_{S_y S_y}(\omega) = [S_{S_y S_y}(\omega) + S_{S_y S_y}(-\omega)]/2$, after some lengthy algebra, we obtain the following expression as given in [75]

$$\bar{S}_{S_y S_y}(\omega) \approx \frac{\bar{S}_x}{2} + \frac{\left(\frac{1}{2}\alpha_1 \bar{S}_x\right)^2}{(\Omega_s - \omega)^2 + \left(\frac{\gamma_s}{2}\right)^2} \cdot \left(\gamma_s |\bar{F}_x| + \frac{(\alpha_1 \bar{F}_x)^2 \bar{S}_x}{2}\right) \qquad (2.96)$$

where the first term is shot noise due to the laser, the second term corresponds to the zero-point fluctuation of the spin oscillator and the last term corresponds to the quantum backaction noise. The expression can also be written as

$$\bar{S}_{S_y S_y}(\omega) = \frac{\bar{S}_x}{2} + (\alpha_1 \bar{S}_x |\chi_s|)^2 \cdot \left(\gamma_s |\bar{F}_x| + \frac{(\alpha_1 \bar{F}_x)^2 \bar{S}_x}{2}\right) \qquad (2.97)$$

We may convert the unit in terms of the Faraday angle $\theta_F = S_y/2\bar{S}_x$. Furthermore, we may integrate across the peak of the spin resonance the noise variance of the spin, assuming $\gamma_s \ll \Delta_{BW} \ll \Omega_s$,

$$\text{var}(\theta) \approx \frac{\Delta_{BW}}{8\bar{S}_x} + \frac{\pi \alpha_1^2}{16} \cdot \left(2 |\bar{F}_x| + \frac{(\alpha_1 \bar{F}_x)^2 \bar{S}_x}{\gamma_s}\right) \qquad (2.98)$$

To conclude, we recover the sensitivity plot for quantum limited measurement (see Fig. 2.10), the first term is the imprecision noise, which goes down with higher optical power, i.e. $\langle S_y^{(in)} S_y^{(in)} \rangle / \bar{S}_x^2 \propto 1/\bar{S}_x$, whereas at higher optical power, the backaction noise dominates $\propto \bar{S}_x$. There exists a sweet spot, where the two effects reach the best compromise known as the standard quantum limit (SQL), which is the optimal working point for measurement precision if squeezing strategy is not employed.

var(θ) (Log)

Imprecision noise

$\propto \dfrac{\Delta_{\mathrm{BW}}}{8\bar{S}_x}$

Quantum backaction noise

$\propto \dfrac{\pi\alpha_1^4 \bar{F}_x^2 \bar{S}_x}{16\gamma_s}$

$\dfrac{\pi\alpha_1^2(2\bar{F}_x)}{16}$

Zero point fluctuations

$\bar{S}_x$ (Log)

$\bar{S}_{x,\mathrm{SQL}}$
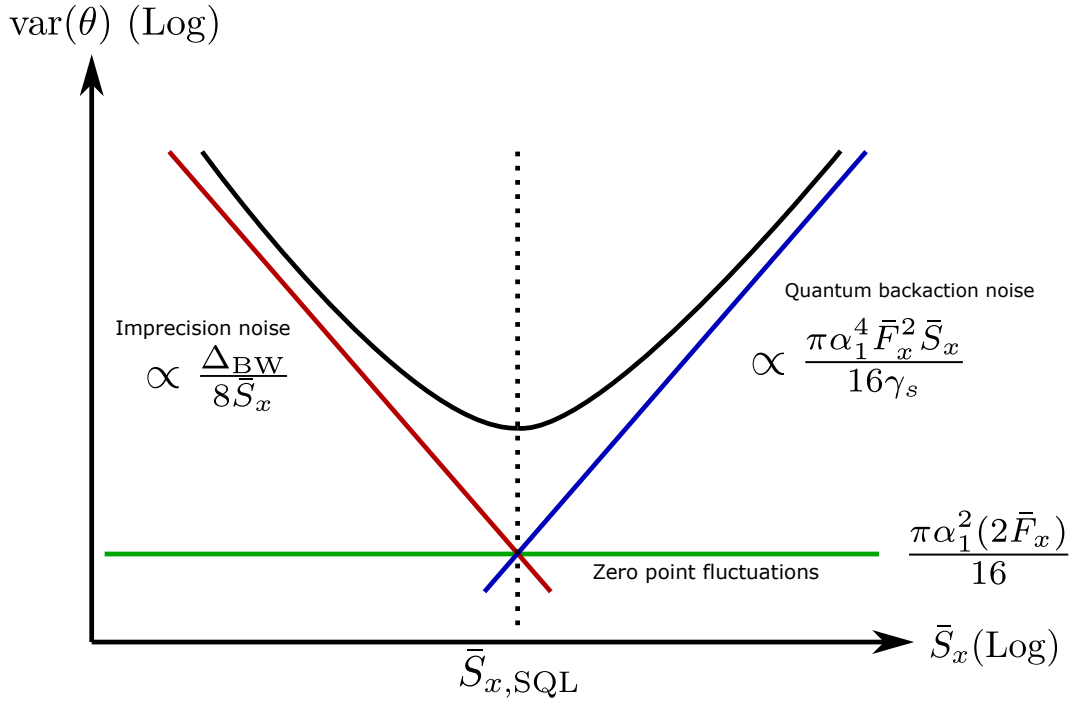
Figure 2.10: Log-Log plot of Faraday angle variance as a function of $\bar{S}_x$. As the laser power increases, since $P_L \propto \bar{S}_x$, the imprecision noise falls as $1/\bar{S}_x$. However, at high optical power, backaction noise competes with the improvement of sensitivity by lowering the imprecision noise. The $\bar{S}_{x,SQL}$ defines an optimal working spot where the two effects reach the best compromise if no squeezing strategy is employed.

2.10 Ponderomotive Squeezing

With sufficiently high optical power, the quantum fluctuations in $S_z^{(\mathrm{in})}$ starts to drive the spin oscillator, which leads to correlations between the spin response $S_y^{(\mathrm{out})}$ and the drive field $S_z^{(\mathrm{in})}$. This effect is analogous to the ponderomotive squeezing in mechanical oscillator [81]. These correlations can be exploited to suppress noise at one optical quadrature at the expense of adding noise in the orthogonal light quadrature. To understand intuitively polarization squeezing of light using spin, we can perform a Fourier transform on both sides of Eqs. 2.85-2.86, we may recast the input-output relation in a matrix form in the frequency domain:

$$\begin{pmatrix} X_L^{(\mathrm{out})}(\omega) \\ P_L^{(\mathrm{out})}(\omega) \end{pmatrix} = \begin{pmatrix} 1 & 4\Gamma_s\chi_s(\omega) \\ 0 & 1 \end{pmatrix} \begin{pmatrix} X_L^{(\mathrm{in})}(\omega) \\ P_L^{(\mathrm{in})}(\omega) \end{pmatrix} \tag{2.99}$$

31

the spin susceptibility is in general complex, we may split it into real and imaginary part:

$$\chi_s = \frac{\Omega_s}{\Omega_s^2 - \omega^2 - i\gamma_s\omega} \approx \frac{1}{2\Delta_s - i\gamma_s} \tag{2.100}$$

$$= \frac{2\Delta_s}{4\Delta_s^2 + \gamma_s^2} + i\frac{\gamma_s}{4\Delta_s^2 + \gamma_s^2} \tag{2.101}$$

$$= \text{Re}[\chi_s] + i\,\text{Im}[\chi_s] \tag{2.102}$$

where we defined $\Delta_s = \Omega_s - \omega$ as frequency difference from the spin oscillator frequency Ω_s. The approximation on the first line we evaluated around the spin resonance $\omega \approx \Omega_s$. Moreover, we see that the susceptibility plays an important role, as the backaction term is directly weighted by the spin susceptibility the $\chi_s(\omega)$. Only the real part of the susceptibility leads to squeezing [56]. More specifically, we follow the calculation in [81], it turns out that the input-output relation can be cast in the form of a rotation in the X_L-P_L phase space plot (see Fig. 2.11) followed by a squeezing operation, the transformed X_L, P_L optical quadrature reads

$$X_L' = S^\dagger(r,\phi)R^\dagger(-\theta)X_L R(-\theta)S(r,\phi) \tag{2.103}$$

$$P_L' = S^\dagger(r,\phi)R^\dagger(-\theta)P_L R(-\theta)S(r,\phi) \tag{2.104}$$

where the rotation operator is defined as:

$$R(\theta) = \exp\left[-i\theta\left(a_y^\dagger(\omega)a_y(\omega) + a_y^\dagger(-\omega)a_y^\dagger(-\omega)\right)\right] \tag{2.105}$$

the effect of rotation operator on the X_L and P_L quadrature is:

$$\begin{aligned}
R(\theta)X_L R^\dagger(\theta) &= \cos(\theta)X_L - \sin(\theta)P_L \\
R(\theta)P_L R^\dagger(\theta) &= \sin(\theta)X_L + \cos(\theta)P_L
\end{aligned} \tag{2.106}$$

and the squeezing operator is defined by

$$S(r,\phi) = \exp\left[r\left(a_y(\omega)a_y(-\omega)e^{-2i\phi} - a_y^\dagger(\omega)a_y^\dagger(-\omega)e^{2i\phi}\right)\right] \tag{2.107}$$

The effect of the squeezing operator on the optical quadrature is:

$$\begin{aligned}
S(r,\phi)X_L S^\dagger(r,\phi) &= X_L(\cosh r + \sinh r \cos 2\phi) + P_L \sinh r \sin 2\phi \\
S(r,\phi)P_L S^\dagger(r,\phi) &= P_L(\cosh r - \sinh r \cos 2\phi) + X_L \sinh r \sin 2\phi
\end{aligned} \tag{2.108}$$

Using the above relationship, we can derive the rotation angle θ, squeeze angle ϕ and squeeze factor r as given in [81]:

$$\theta = \arctan(\mathcal{K}/2), \quad \phi = \frac{1}{2}\text{arccot}(\mathcal{K}/2), \quad r = \text{arcsinh}(\mathcal{K}/2) \tag{2.109}$$

(a)

(b)
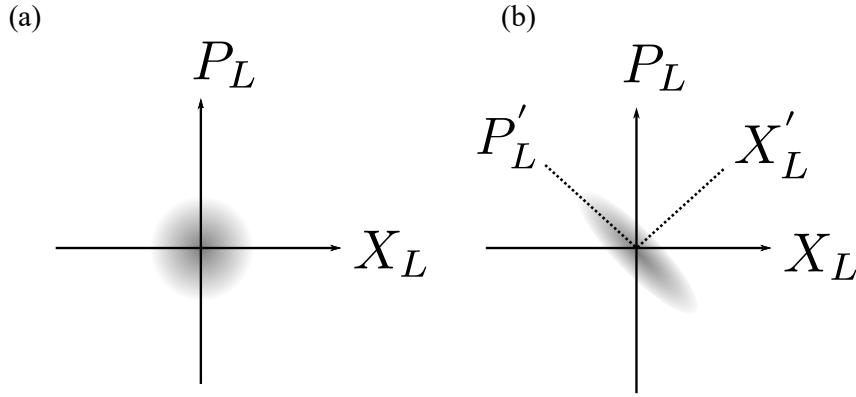
Figure 2.11: (a) Phase space diagram of the coherent state of light. (b) Phase space diagram of the ponderomotive squeezed state.

where $\mathcal{K}$ is defined as $\mathrm{Re}[\chi_s]4\Gamma_s$. For the Faraday interaction, assuming $|\Delta_s| = \gamma_s/2$, $\mathrm{Re}[\chi_s] \approx \mathrm{Im}[\chi_s] \approx \frac{1}{2\gamma_s}$, therefore, we get $\mathcal{K} \approx \frac{2\Gamma_s}{\gamma_s} \approx \frac{2\Gamma_s}{\gamma_{\mathrm{sc}}} = C_s$, where we introduce the quantum cooperativity $C_s = \frac{2\Gamma_s}{\gamma_{\mathrm{sc}}}$. Now, we know what happens to the output field after the spin-light interaction. We may choose an arbitrary quadrature angle between S_y and S_z to detect the ponderomotive squeezing,

$$S_\beta = \cos(\beta)S_z - \sin(\beta)S_y \tag{2.110}$$

where β is the phase quadrature angle. Similar to Sec. 2.9, we may compute the symmetrized output spectrum of a ponderomotive squeezed state in the rotated light basis,

$$\bar{S}_{S_\beta S_\beta}(\omega) \approx \frac{\bar{S}_x}{2} + \frac{\left(\frac{1}{2}\alpha_1\bar{S}_x\right)^2}{(\Omega_s - \omega)^2 + (\frac{\gamma_s}{2})^2} \cdot [\sin^2(\beta)(\gamma_s\,|\bar{F}_x| + \frac{(\alpha_1\bar{F}_x)^2\bar{S}_x}{2}) \tag{2.111}$$

$$- 2\sin(\beta)\cos(\beta)\Delta_s\bar{F}_x] \tag{2.112}$$

where the first term corresponds to imprecision noise due to shot noise, since the shot noise of a coherent state is equally distributed in $X_L^{(\mathrm{in})}$ and $P_L^{(\mathrm{in})}$ it is independent from the homodyne angle β. The second term is the atomic signal and the quantum backaction noise term. The last term is a cross term that encodes the correlation between spin response and the quantum fluctuation in the phase quadrature of the light, which is responsible for the squeezing.

Chapter 3

Experiment implementation of spin light interface

In this chapter, we present the experiment setup of our spin light interface and the key characterization techniques we use to characterize our spin ensemble. This allows us to obtain useful parameter to quantify the spin measurement rate and spin damping rate used in the hybrid experiment. For an earlier description of this setup, we refer readers to [59]. The description in this chapter partially follows this reference. In Sec. 3.7, the new data on the ponderomotive squeezing of light is presented.

3.1 Experiment setup

The experimental setup of the spin-light interface is shown in Fig. 3.1 and the apparatus can in general be classified into three categories, namely, preparation, manipulation and detection of the cold spin polarized atomic ensemble. For the spin ensemble preparation, the cold atomic beams generated from the 2D MOT fill the 3D MOT which consists of the anti-Helmholtz coil and the laser cooling beams propagating from the three orthogonal directions at the center of the glass chamber. Laser cooled atoms are then captured by the far off-resonant trap provided by a focused 25 W 1064 nm dipole trap laser beam propagating from the left. To prepare the collective spin, the atomic ensemble is polarized by the resonant 22 Zeeman pumping beam (780 nm) sent from the bottom along a static, homogeneous DC magnetic field in the x-direction created by the Helmholtz coil. In addition, compensation coils are installed to cancel out residual stray field and maintain spin stability. To manipulate the spin state, either AC magnetic field generated by the RF coils or the circularly polarized light generated by the EOM can be used to drive the spin into precession. Finally, for detection, an off-resonant 780 nm coupling beam is sent from the right to the left, a polarimeter sensitive to polarization change of light is used to pick up the spin signal. The CCD cameras are installed for performing the absorption, florescence and Faraday imaging.
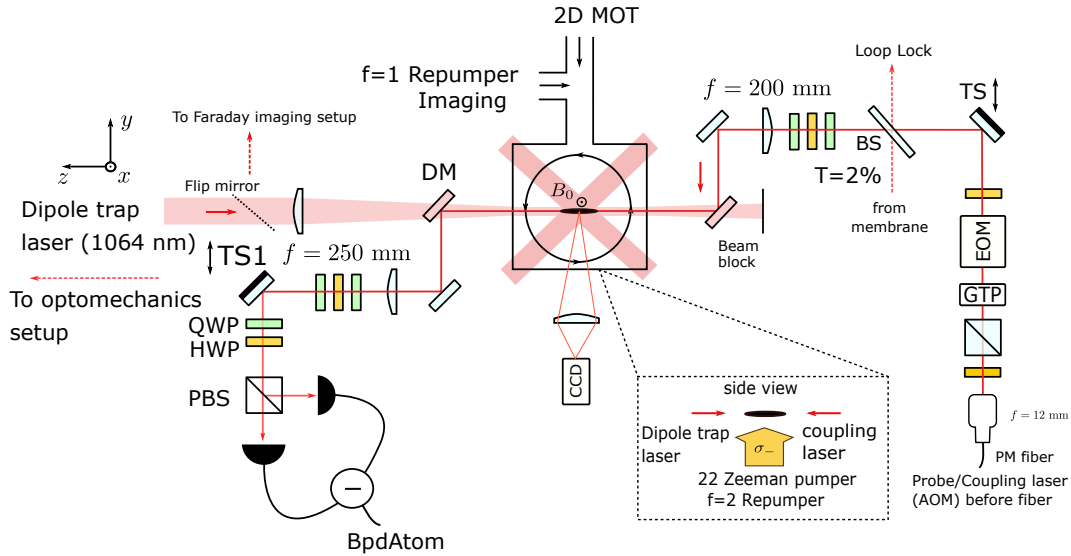
Figure 3.1: Schematic diagram of the spin-light interface

Optical setup

As shown in Fig. 3.1, the probe laser beam is first amplitude modulated using an acoustic optical modulator (AOM) before coupling into a polarization maintaining (PM) fiber. The AOM can be used to switch on and off the beam or create probe pulses. Then, the laser beam exits from a fiber collimator[1] and passes through a Glan-Thompson polarizer (GTP) to create a clean polarization with an extinction ratio of 10^{-8}. After that, the probe beam passes through a free space Electro-optical modulator (EOM)[2]. The EOM is used to create the circular polarized light to drive the spin (see Sec. 3.6.4). The probe beam is focused using a singlet lens with f = 200 mm onto the atomic cloud confined by the dipole trap beam (1064 nm) propagating from the opposite direction. We use a pair of dichroic mirrors on both sides of vacuum chamber to separate the two laser beams. Since the atomic signal is very sensitive to change in laser polarization, the compensation waveplate stack (QWP-HWP-QWP) are installed on both sides to cancel out the bi-refrigence effect due to the dichroic mirror and the vacuum chamber. After passing through the atomic ensemble, the coupling beam carrying the spin signal is picked up by the polarization sensitive polarimeter. The polarimeter consists of a combination of (QWP-HWP) waveplate and a polarisation beamsplitter. By adjusting the wave-plates, arbitrary superposition of the S_y and S_z can be measured. Furthermore, to realize the hybrid spin mechanics experiment, the translation stage (TS) at the input displaces the coupling beam (here the probe beam is referred as the coupling beam) to intersect the atomic ensemble at an angle. Similarly, the translation stage

---

[1]Schäfter & Kirchhoff 60 FC-F-4-A 18-02 or 60 FC-F-4-M 12-10 collimator.
[2]Free space electro-optical modulator from QUBIG: PCA4R-NIR AC (650 - 1000) nm

(TS1) installed for the pick-up mirror can move to a position where the coupling laser beam is sent to the optomechanical part of our hybrid setup (see Chapter 5.7).

3.2 Laser systems

To control and manipulate the neutral ^{87}Rb atoms, several optical transitions must be addressed simultaneously with lasers at different frequencies. First, we start with an overview of the optical transitions relevant to the ^{87}Rb atoms, then we present the individual laser systems that are used for the experiment.

Optical transitions

The relevant optical transitions for ^{87}Rb atoms are summarized in Fig. 3.2 below. For laser cooling and absorption imaging of the atoms, the circularly polarized light are used to address the $f = 2, m_f = \pm 2 \rightarrow f' = 3, m'_f = \pm 3$ closed cycling transition. To satisfy the dipole selection rule and the conservation of angular momentum, the excited atom can only decay to $f = 2$ hyperfine ground state for further laser cooling. For spin preparation, $\sigma^\pm$ circularly polarized light is applied to address the $f = 2 \rightarrow f' = 2$ transition, once the atoms reach the $|f = 2, m_f = \pm 2\rangle$ magnetic sub-level, the atom is in a dark state as the next possible optical transition $f = 2, m_f = \pm 2 \rightarrow f' = 3, m'_f = \pm 3$ is off-resonant to the pump laser. During the Zeeman pumping, excited atoms can decay into $f = 1$ if $\Delta m_f = m_f - m_{f'} = 0, \pm 1$. A $\sigma^\pm$ circularly polarized repumper laser addressing $f = 1 \rightarrow f' = 2$ can bring the atoms back to $f = 2$ for further Zeeman pumping. For large laser atom detunings (see Sec. 2.3), the coupling laser induces transitions allowed by the dipole selection rule.

Diode lasers

We present an overview of the diode lasers used for the preparation and imaging of the atomic ensemble. As shown in Fig. 3.2, since the $f = 1$ and $f = 2$ are separated by hyperfine splitting ~ 6.8 GHz, two different homebuilt grating stabilized diode lasers, i.e. MASTER and REPUMPER (see Fig. 3.3) are used to address optical transitions starting from the different hyperfine state, i.e. $f = 2 \rightarrow f'$ and $f = 1 \rightarrow f'$. The corresponding hyperfine excited state f' are reached by fine tuning the laser frequency using an AOM. Moreover, the AOM acts as a switch to turn the beam on and off during the spin preparation sequence or create pumping pulses for stroboscopic cooling used in the hybrid experiment (see Chapter 5.7). The diode lasers are frequency stabilized using frequency-modulated (FM) saturated absorption spectroscopy on ^{87}Rb vapor cells. Here, the double pass AOM configuration is used to provide a wider frequency tuning range, while enabling fast frequency shift with minimal beam deflection during the MOT cooling stage. Another diode laser SLAVE is seeded by the MASTER and amplified by a tapered amplifier BOOSTA to deliver sufficient light (~ 1 W) for laser cooling and a small
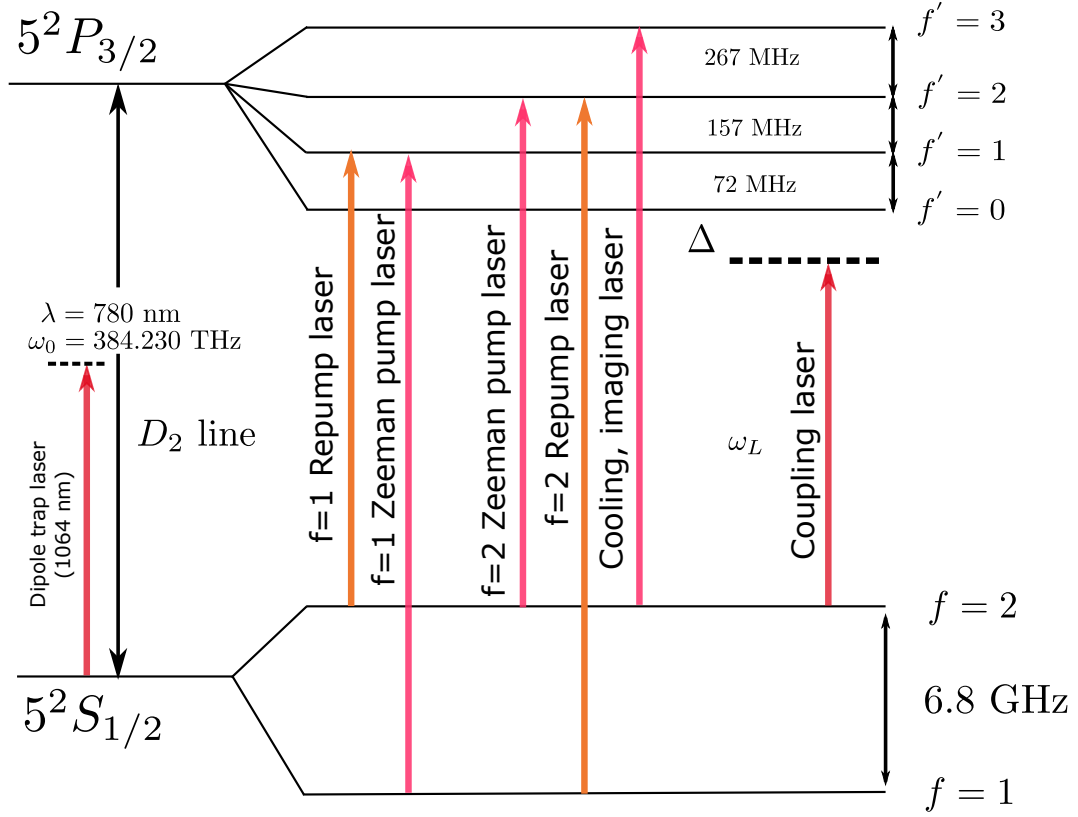
Figure 3.2: Overview of the optical transitions addressed by different lasers (arrows) for ^{87}Rb used in the experiment. The frequency splittings of the hyperfine ground state and excited manifolds are provided.

portion of light ~ 5 mW goes to imaging beam. The REPUMPER laser is used to recycle atoms that decayed to $f = 1$ from $f = 2$. Moreover, it can also be used to Zeeman pump atoms to $f = 1, m_f = \pm 1$ if we work with $f = 1$ hyperfine ground state spin. Recently, we also set up a digital phase-locked loop (DPLL)[3] to stabilize the frequency offset [82] between an interference filter stabilized diode laser REPUMPER2 and MASTER laser. The REPUMPER2 is a $f = 1$ repumper which brings atoms from $f = 2$ back to $f = 1$, this was sometimes used to shorten the cloud.

Coupling laser

Our coupling laser[4] is a widely tunable, continuous wave low noise Ti:Sa laser. To probe the atomic spins, the laser frequency can be set to a large red detuning $\sim$ GHz with respect to the $5^2S_{1/2} \rightarrow 5^2P_{3/2}$ optical transition, this renders the

---
[3]Analog evaluation circuit board ADF4002
[4]CW laser from MSquared (SolsTiS)

spin light interaction to be dominated by the Faraday effect, while suppressing higher order tensor coupling (see Sec. 2.3). The laser frequency can be coarsely adjusted by rotating a piece of birefrigent filter [83] which introduces wavelength dependent loss into the laser resonator, fine adjustment of wavelength is achieved by tuning the Etalon spacing. The coupling laser typically outputs up to 1 W of light at 780 nm when being pumped by a Coherent Verdi laser delivering 7.25 W of light at ~ 500 nm. More importantly, for the laser power level (roughly > 1mW) used in our experiment, the coupling laser is shot noise limited in both amplitude and phase quadrature for frequencies above 1.5 MHz [59], which is sufficient for performing quantum measurements.
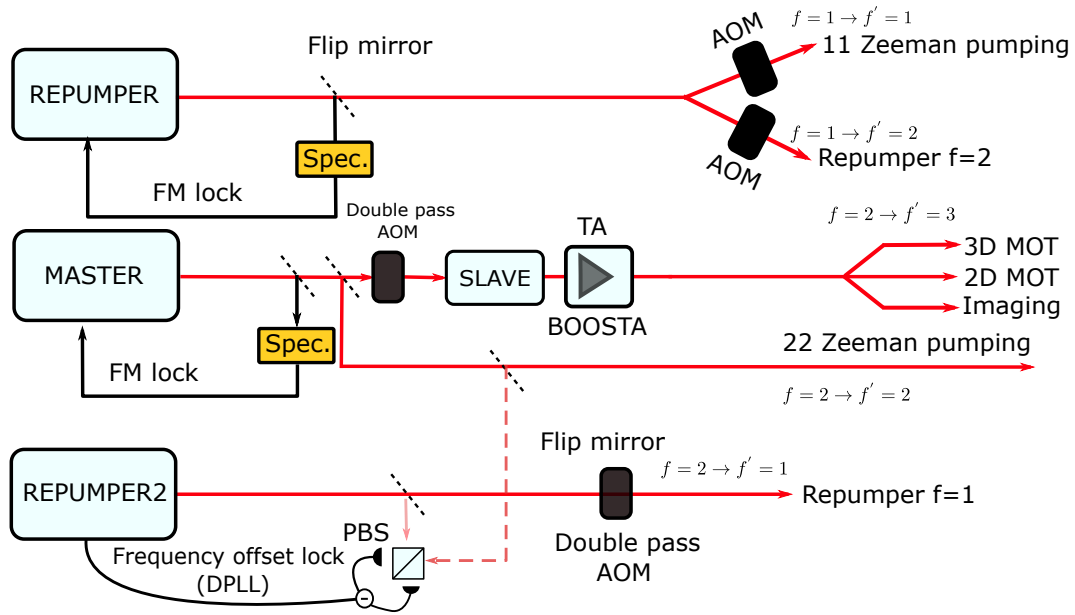
Figure 3.3: Schematic diagram of the diode lasers system to address different optical transitions for preparation of a well-polarized ^{87}Rb spin ensemble.

Dipole trap laser

Cold atoms naturally free fall under gravity, in order to hold the atoms in mid-air for interrogation, we employ a powerful far off-resonant laser to create a scalar potential to trap cold atoms. The dipole trap laser is a commerical Nd:YAG laser[5] with maximum power output of 25 W at $\lambda_{\text{trap}} = 1064$ nm. An AOM is installed after the laser to allow control of the trap depth and switching for trap frequency and time-of-flight (TOF) measurement. Details of the dipole trap characterization are described in [84]. After the AOM, 16 W of the first order diffracted

---

[5]Mephisto MOPA from InnoLight with original maximum power output of 40 W

beam then propagates in a direction opposite to the coupling beam (see Fig. 3.1) and is focused by a singlet lens with $f = 250$ mm down to a small spatial region with transverse waist of 92 μm. In the large detuning limit, the dipole laser creates a conservative, state-independent scalar potential $U_{\text{dip}}(\text{r})$ to trap laser-cooled atoms.

$$U_{\text{dip}}(\text{r}) = \frac{3\pi c^2}{2\omega_0^3} \frac{\gamma_e}{\Delta} I_L(r,z) \tag{3.1}$$

where the spatial distribution $I_L(r,z)$ of the trap laser reads

$$I_L(r,z) = \frac{2P}{\pi w_{\text{trap}}^2(z)} e^{-2r^2/w_{\text{trap}}^2(z)} \tag{3.2}$$

where P_0 is the peak power at $z = 0$ and the trap waist is defined as $w_{\text{trap}}(z) = w_{0,\text{trap}}\sqrt{1 + (z/z_{0,\text{trap}})^2}$, and $z_{0,\text{trap}} = \pi w_{0,\text{trap}}^2/\lambda_{\text{trap}}$ is the Rayleigh range of the dipole trap beam, where $w_{0,\text{trap}}$ is the trap waist at $z = 0$. At large red detuning, the laser beam creates an attractive potential for atoms with trap depth of $U_0 = U_{\text{dip}}(0) \approx -k_B \times 300\mu$K [84] and the spontaneous scattering rate due to dipole laser $\gamma_{sc} = U_{\text{dip}}\,\gamma_e/(\hbar\Delta) \sim 1$ Hz is suppressed [84]. At low temperatures $k_B T \ll U_0$, the atomic number distribution takes the form of a Gaussian distribution with cylindrical symmetry [84]:

$$n(\mathbf{r}) = n_0 \exp\left(-\frac{U_{\text{dip}}(\mathbf{r})}{k_B T}\right) \approx N\sqrt{\frac{1}{8\pi^3 \sigma_r^4 \sigma_z^2}} \exp\left(-\frac{r^2}{2\sigma_r^2}\right) \exp\left(-\frac{z^2}{2\sigma_z^2}\right) \tag{3.3}$$

where n_0 is the peak number density, σ_r and σ_z are the standard deviation spatial spread of a Gaussian spatial distribution along the transverse and longitudinal direction, respectively. The widths σ_r and σ_z are computed to be 18 μm and 6.3 mm (using $T = 50$ μK, trap frequencies $\omega_r = 611$ Hz and $\omega_z = 1.73$ Hz in their respective confinement direction [84]). The aspect ratio σ_z/σ_r of ~ 300 gives a large optical depth which is ideal for strong spin light interaction.

3.3 Atomic ensemble preparation and imaging

In this section, we discuss the experimental technique that are relevant to the preparation and imaging of the atomic ensemble.

Laser cooling and dipole trap loading

Details of the atomic preparation are discussed in [59, 85, 86]. Here, we provide a brief account of the physical processes involved in loading a dipole trap. First, the cold atomic beam generated from 2D MOT is transferred to the center of 3D MOT chamber, where three mutually orthogonal pairs of opposite circularly polarized counter-propagating laser beams intersect at the center of magnetic quadruple field produced by the anti-Helmholtz coils. In the presence of the spatially-varying magnetic field, atoms moving away from the center are brought back to

resonance, which gives a momentum kick opposite to the atomic motion due to photon scattering. In essence, the atoms experience a velocity-dependent damping force and a position dependent restoring force due to the light. Exploiting the closed cycle transition of ^{87}Rb between $f = 2 \rightarrow f' = 3$, on average the atoms are cooled over repeated cycles of absorption and spontaneous emission. Colder atoms that scattered into the "dark" $f = 1$ hyperfine state are not resonant with the cooling lasers accumulate in the center, whereas the atoms away from center gets repumped into $f = 2$ for continuous laser cooling. The next phase is dark MOT, the repumper laser intensity is further reduced and MASTER laser is red-detuned further to reduce the repulsive photon scattering. This process builds up a compressed atomic cloud in the center overlapped with the dipole trap. The weak MOT phase acts as a transitory to the Molasses phase, where the magnetic field gradients are ramped down to zero and the cooling MASTER intensity is reduced and red-detuned further to reduce heating of the atoms. Atoms are cooled to sub-Doppler temperatures $\approx 50\,\mu$K further due to polarization gradient cooling and loaded into dipole trap.

3.3.1 Absorption Imaging

Absorption imaging provides a convenient way to characterize the geometry, number density distribution and temperature of the atomic ensemble. To obtain an absorption image of the ensemble, an imaging beam is sent along the short axis of the cloud. During a typical absorption image sequence (see Fig. 3.4), atoms are Zeeman pumped to the stretched state $\left|f = 2, m_f = -2\right\rangle$ using circularly-polarized beam σ_- resonant to $f = 2 \rightarrow f' = 2$ along a small guiding field $B_y \approx 1$ G parallel to the imaging axis. Atoms decayed into $f = 1$ are recycled back to $f = 2$ using the σ_- polarized repumper laser that addresses the $f = 1 \rightarrow f' = 2$. Subsequently after the state preparation, atoms in $\left|f = 2, m_f = -2\right\rangle$ resonantly scatter the imaging beam on the cycling transition $f = 2, m_f = -2 \rightarrow f' \rightarrow 3, m_{f'} = -3$.
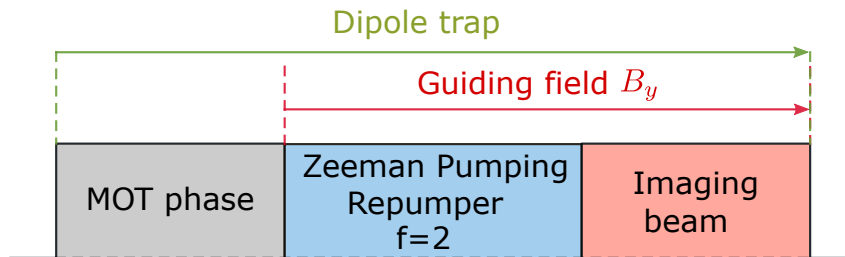
Figure 3.4: Schematic diagram of the absorption imaging sequence, the arrow indicates the time span which the dipole trap and guiding field remains turned on.

As a result, the atoms in the path of the imaging beam cast a shadow on a cali-

brated CCD camera. Comparing the absorption image to a reference image without the atoms allows one to obtain the optical depth,

$$\text{OD}(x,z) = -\ln\left(\frac{I_{\text{atoms}}(x,z)}{I_{\text{ref}}(x,z)}\right) \tag{3.4}$$

Using the Beer-Lambert law, the optical density is connected to column number density n_{2D} (integrated along the imaging axis):

$$\text{OD}(x,z) = \sigma \int n(x,y,z)dy := \sigma n_{2D}(x,z) \tag{3.5}$$

where the atomic scattering cross section in the low saturation limit reads

$$\sigma = \frac{\sigma_0}{1 + (2\Delta/\gamma_e)^2} \tag{3.6}$$

depends on the resonant scattering cross section on the imaging transition and the detuning of the imaging beam Δ. The atom number N is obtained by integrating the number density of each pixel across the xz-imaging plane.

$$N = \iint n_{2D}(x,z)dxdz = \iint \frac{\text{OD}(x,z)}{\sigma}dxdz \tag{3.7}$$
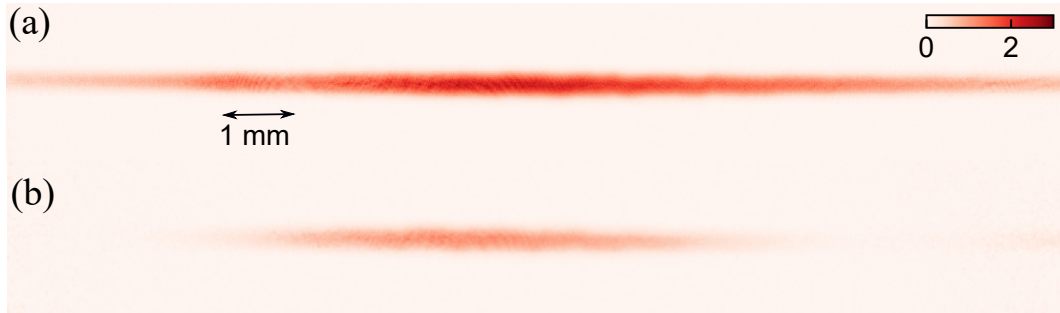
Figure 3.5: Absorption images of the atomic ensemble upon releasing from the dipole trap with 1 ms of time-of-flight. (a) Long atomic cloud filled with 20 M atoms. (b) Short atomic cloud filled with 10 M atoms. The scale bar on the top right corner indicates the measured OD along the imaging axis.

After the state preparation, the trap beam can be abruptly switched off for a variable amount of time τ_{tof}, this allows the atomic cloud to undergo ballistic expansion before an absorption image is taken. Here, absorption images of a short and long atomic cloud with fixed time-of-flight τ_{tof} duration of 1 ms are included in Fig. 3.5. Collecting multiple absorption images as a function of τ_{tof} is known as time-of-flight measurement of the cloud, which allows one to determine the temperature of cloud from the expansion of the cloud. As a side remark, we denote

that the above formula only applies to imaging on resonance requires knowledge of the detuning Δ. After a long period of time ($\sim$weeks), the lock point of the FM lock could change slightly due to effect such as thermal drift, thus the imaging beam could detune. To correct this, the measured integrated OD is plotted as a function of the imaging beam AOM voltage as shown in Fig. 3.6. Here, the detuning of the imaging beam is scanned around the resonance. Each data point corresponds to an average of 3 independent measurements. In this example, a Lorentzian function is fitted to the data, the atomic resonance is centered at AOM voltage of 4.65 V. Moreover, we obtain the FWHM of 0.385 V (with voltage to frequency conversion factor = 0.05 V/MHz) which corresponds to 7.7 MHz which is slightly larger than the natural linewidth γ_e = 6.06 MHz. The imaging beam should be set to resonance to avoid dispersive effect that could distort the image.
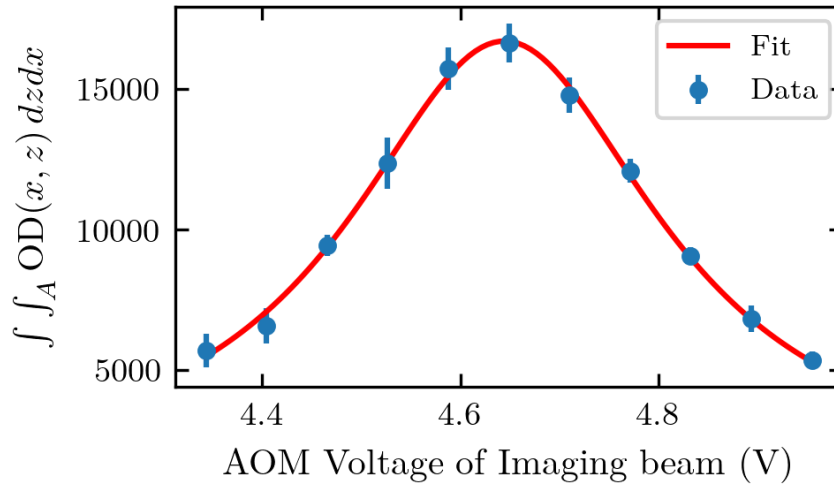
Figure 3.6: Plot of the integrated OD as a function of detuning from the imaging transition $f = 2 \rightarrow f' = 3$. Each blue dot corresponds to an average of 3 independent measurements. The red line is a Lorentzian fit to the measured data.

Faraday Imaging

We can also image DC Faraday rotation [87] onto a CCD camera (see Fig. 3.8) by sending the coupling beam along the long axis of the spin ensemble with the highest OD in the z-direction. The spin is rotated to the propagation axis such that the Faraday rotation measured the macroscopic spin signal $F_z \approx 2N$. The Faraday imaging setup looks similar to the polarimeter except that the balanced photodetector is replaced by a CCD camera (see Fig. 3.7). The HWP is set at $\pi/4$ such that both arms after the PBS is balanced.
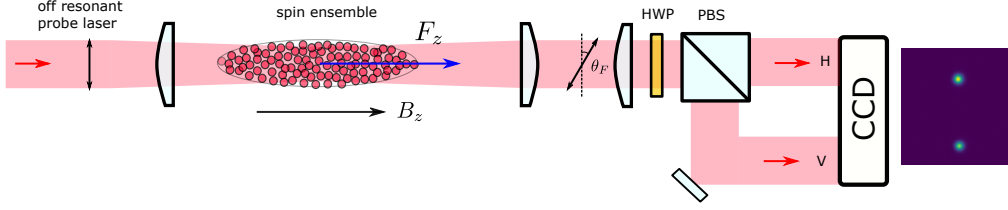
Figure 3.7: Schematic diagram of Faraday imaging setup

This is used to optimize the spatial overlap of the spin ensemble with the coupling beam, typically after a large change in beam alignment e.g. swapping the collimator of the fiber coupler with a different f. The camera position is adjusted such that both the image of the atomic ensemble and coupling beam are focused. Due to the poor signal-to-noise contrast, a small detuning ($\Delta = -1$ to -5 GHz) is required for the Faraday imaging. Here, both absorption images and reference images are obtained horizontally polarized and vertically polarized light $I_{H/V}^{\text{atom}}$, $I_{H/V}^{\text{ref}}$, respectively. Using the sum and difference of the horizontal and vertical polarization images thus gives us the spatial distribution of the scalar and vector signal,

$$I_{\text{scalar}} = \frac{(I_H^{\text{atom}} - I_H^{\text{ref}}) + (I_V^{\text{atom}} - I_V^{\text{ref}})}{I_H^{\text{ref}} + I_V^{\text{ref}}} \tag{3.8}$$

$$I_{\text{vector}} = \frac{(I_H^{\text{atom}} - I_H^{\text{ref}}) - (I_V^{\text{atom}} - I_V^{\text{ref}})}{I_H^{\text{ref}} + I_V^{\text{ref}}} \tag{3.9}$$

An example Faraday imaging measurement with a probe detuning of -2 GHz is plotted below. For scalar interaction [see Fig. 3.8(a)], the spin-state independent refractive index of the atomic ensemble leads to focusing of the coupling beam. From the fits, we can determine the e^{-2} waist (black dashed circle) of the coupling beam at the position of the atom to be 48 μm and the transverse radial waist of the atomic cloud is 27 μm, respectively. For Faraday interaction, the vector part shows the distribution of the Faraday spin signal across the laser beam. Using Eq. 2.24 and Eq. 2.25, the on-axis optical depth OD(x, y) per pixel can be computed [see Fig. 3.8 (c)], the measurement shows a peak optical density of 2000, and an effective OD (average across the pixels of the beam cross section) yields ~ 500. We see that the local spin light interaction strength can vary a lot depending on the position of the laser beam with respect to the position of atom.

3.4 Spin state preparation

3.4.1 Optical pumping

As discussed in Sec. 2.1, the starting point of our experiment is to prepare the atoms in the lowest Zeeman sublevel $|f = 2, m_f = -2\rangle$ to realize a highly oriented
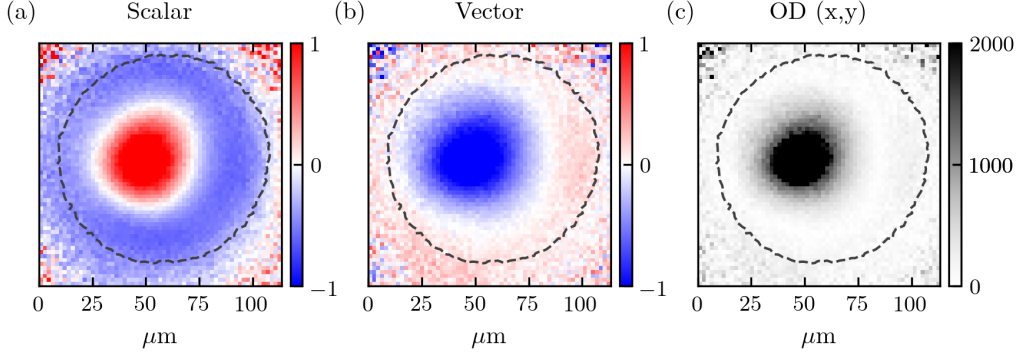
Figure 3.8: Faraday rotation image of a spin ensemble (obtained with $f = 12$ mm fiber collimator at -2 GHz). (a) Image of the laser beam focused by the atomic ensemble due to scalar interaction. (b) Image of DC Faraday rotation signal from the vector polarizability. (c) On axis OD(x,y) computed from Faraday image.

spin state that approximates a spin oscillator. Experimentally, this is achieved by simultaneously applying two σ_- polarized lasers i.e. $f = 2$ Zeeman pumper and repumper lasers (see Sec. 3.2) parallel to the static magnetic field in the x-direction. The pumping process can be divided into two steps. An example is illustrated in Fig. 3.9, an atom initially occupies $|f = 2, m_f = 0\rangle$ absorbs a σ_- photon from the resonant Zeeman pump beam. In general, the excited atoms can decay to ground state via any route (wavy arrows) permitted by dipole selection rule Δf, $\Delta m_f = 0, \pm 1$ and conservation of angular momentum. Overall, atoms net polarization build up because the atom has a higher chance to either move by $\Delta m_f = -1, -2$ than $\Delta m_f = 0$. More importantly, the stretched state $|f = 2, m_f = -2\rangle$ is dark to the pump beam[6], this pumping process accumulate atoms into this state until there is no more scattering of the pump photon. However, the atoms can also decay to $f = 1$ ground state (wavy dashed arrows). Therefore, the σ_- repump laser addressing $f = 1 \rightarrow f' = 2$ repumps atoms that decayed to $f = 1$ hyperfine ground state (see Fig. 3.2) while acting as a Zeeman pumper. An important figure of merit of the spin light interface is the spin orientation,

$$p = \frac{1}{f} \sum_{-f}^{f} m \cdot \langle \rho_{m,m} \rangle \tag{3.10}$$

where $\rho_{m,m}$ is the diagonal density matrix of the spin. A detailed characterization of the pumping is discussed in Sec. 3.5.3. The pumping process robustly initializes

---

[6]Next possible transition $f = 2 \rightarrow f' = 3$ is off resonant to the pump beam

spin polarization characterized by spin orientation up to ~ 0.9 for $B_0 = 2.8$ G. The resonant pump beam and repumper beam indeed introduces decoherence, which broadens the spin linewidth. For typical Faraday rotation characterization, the resonant pump and repumper beams are switched off to maximize the coherence time. More importantly, pumping is a flexible knob that allows us to control the quality factor of our spin oscillator for efficient cooling of the mechanical oscillator (see Chapter 6).
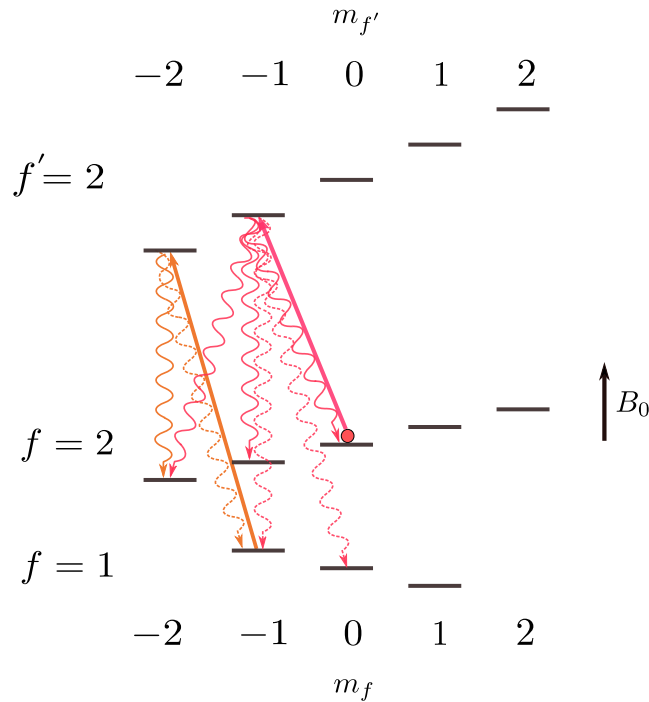
Figure 3.9: Preparing atoms to the $|f = 2, m = -2\rangle$ via optical pumping. An example (see red circle) above shows an atom starts from the $|f = 2, m = 0\rangle$. Excited atoms can decay into any ground state which satisfies conservation of angular momentum and dipole selection rule Δf, $\Delta m_f = 0, \pm 1$. The wavy (dashed) arrows indicate atom decay into $f = 2$ ($f = 1$) hyperfine state.

3.4.2 Magnetic field control

Since our spin oscillator frequency Ω_s is defined by the static magnetic field B_0, it is crucial to maintain a stable and homogeneous magnetic field across the atomic ensemble. To achieve this, a pair of water-cooled coils with diameter 17 cm is employed in Helmholtz configuration (see Fig. 3.10) to set a large static bias field along x direction with a maximum tuning range of 7 G at 3 A. A larger rectangular ~ 0.7 m compensation coil surrounding the vacuum chamber[7] allows for a

---

[7]The compensation coil is also employed in Helmholtz configuration.

homogeneous field to be produced at the atomic site. This allows for fine magnetic field adjustment with a tuning range of 1.5 G at current up to 5 A. The main role of the compensation coil is to counteract any stray field[8] that might enter the spin system using closed-loop control. This is set up by placing a low noise fluxgate sensor [9] as close as possible to the atom. For different magnetic field set values on the computer, our homebuilt magnetic field stabilization PID system[10] then actively stabilize the difference between a pre-calibrated setpoint and the sensor detector output to zero. In general, the feedback run in two regimes, i.e., short and long time scale. For short time scale ($\sim$ ms), the PID takes out noise consists of the dominant 50 Hz harmonics noise to prevent the spin Larmor frequency to jitter at kHz frequency during the Faraday measurement. Whereas for long time scale ($\sim$ mins), the feedback counteracts slow drift due to e.g. thermal drift from coils such that the same spin oscillator frequency can be reproduced to obtain measurement statistics for averaging. Upon turning on the closed loop, the spin linewidth becomes narrower and the long term drift of the spin is reduced. With our recent improvements in the magnetic field control, we obtain a spin-linewidth $\gamma_s \approx 2\pi \times 50$ Hz and a long term rms fluctuation of 42 Hz over a period of an hour. Here, we explain the calibrate procedure to set up the magnetic field system. The calibration procedure serves several purposes, it allows one to null out the earth magnetic field and to establish the closed loop system. Also, this procedure is necessary after an old piece of equipment is replaced, e.g. a current source. First, the measured magnetic field is plotted as a function of the applied current across both the compensation coil and bias coil, respectively (see Fig. 3.11). The measured magnetic field is converted from the Larmor frequency given by Zeeman effect (see details in Sec. 3.5.2):

$$
\begin{aligned}
\Omega_s &= \gamma_f |B| \\
&= \gamma_f \sqrt{B_x^2 + B_\perp^2} + \delta\Omega_s B^2
\end{aligned}
\tag{3.11}
$$

where the gyromagnetic ratio $\gamma_f \approx \pm 0.7$ MHz ($f = 2, 1$) and $B_\perp^2 = B_y^2 + B_z^2$ are the magnetic field components perpendicular to the macroscopic static field along x and the latter term $\delta\Omega_s$ is the quadratic Zeeman contribution due to large static magnetic field. The Larmor frequency is then extracted by fitting the spectrum of a ring down measurement after a RF pulse excitation[11]. As shown in Fig. 3.11(a), at zero compensation coil current, the magnetic field is non-zero, this can be nulled out by introducing an offset I_{comp,x_0} to the compensation coil i.e. replacing $I_{\text{comp},x}$

---

[8]Prominent examples of stray field in our lab include earth magnetic field, 50 Hz noise radiation from nearby electronics, or a powerful $\sim$ T magnet from other labs.

[9]Mag-03 Bartington fluxgate sensor low-noise ($<$ 6 pTrms/Hz), 3 kHz bandwidth

[10]Physics Basel SP 962.

[11]Here, the RF resonant frequency is calibrated previously. If no previous calibration is performed before, one can estimate the magnetic field strength in Helmholtz configuration (based on the e.g. number of windings of the coil and current I_{coil}) to obtain a good estimate or use an external magnetic sensor to calibrate the gain factor.
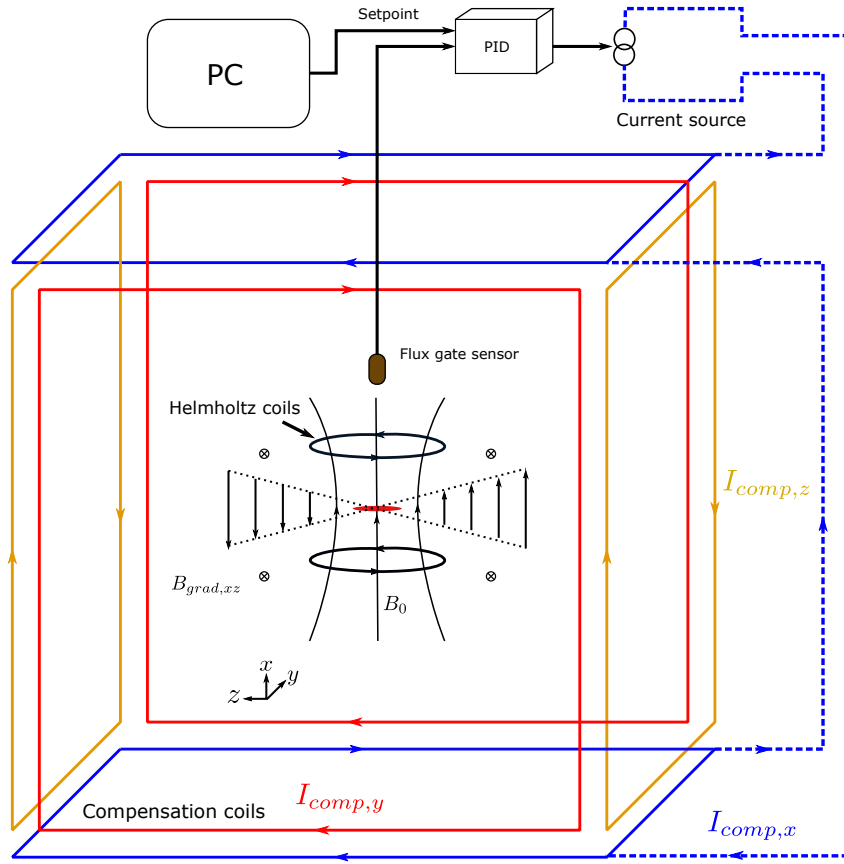
Figure 3.10: Schematic diagram of the magnetic field system

by $I_{\mathrm{comp,x_0}} + I_{\mathrm{comp,x}}$. The calibration is repeated for y and z direction to null out the residual perpendicular static field due to environment. Moreover, the slope of the open loop measurements allow one to calibrate the open loop gain conversion factor (G/A), which converts the open loop applied current into the applied open loop Helmholtz coil field in the closed loop calibration measurement included below (see the x-label of Fig. 3.12).

To operate the magnetic system in the closed loop, as mentioned above, the lock setpoint of the flux gate sensor has to be pre-calibrated V_{sensor} using the following equation:

$$V_{\mathrm{sensor}} = V_0 + G_{\mathrm{tot}}B_{\mathrm{tot}} + G_{\mathrm{bias}}B_{\mathrm{bias}} \tag{3.12}$$

where V_0 is the sensor output at zero field (in presence of the zero-field compensation), G_{tot} and G_{bias} are the sensor sensitivity values for the total magnetic field $B_{\mathrm{tot}} + B_{\mathrm{bias}}$ and the Helmholtz magnetic field B_{bias}. To determine G_{tot} and G_{bias}, the Helmholtz coil field is scanned to determine $(G_{\mathrm{tot}} + G_{\mathrm{bias}})$ i.e. $V_{\mathrm{sensor}} = V_0 + (G_{\mathrm{tot}} + G_{\mathrm{bias}})B_{\mathrm{bias}}$ for $B_{\mathrm{tot}} = B_{\mathrm{bias}}$. Similarly, the sensor gain factor of compensation field B_{comp} can be determined by measuring the sensor output as a func-
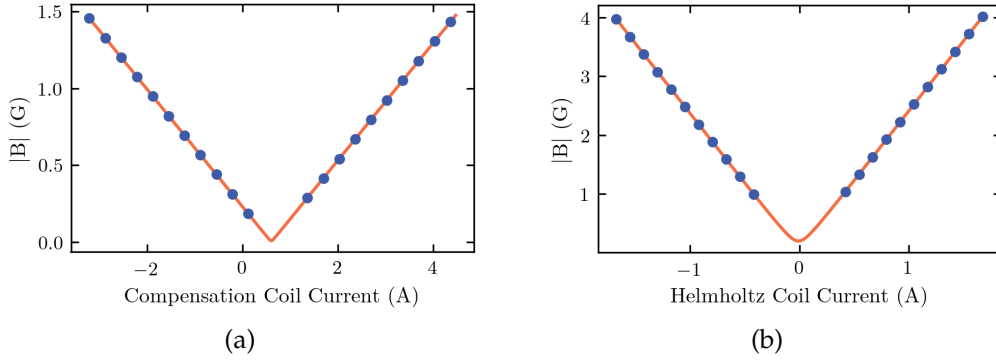
Figure 3.11: Open loop measurement of magnetic field as a function of current through (a) compensation coil (b) Helmholtz coil after the earth field is nulled out.

tion of the compensation field at a fixed Helmholtz coil field B_{bias} i.e. $V_{sensor} = V_0 + G_{tot}(B_{bias} + B_{comp}) + G_{bias}B_{bias}$. By comparing the two independent calibrations, we can determine G_{tot} and G_{bias}. Using the calibrated sensor sensitivity values, we may operate the magnetic field system in closed loop. In Fig. 3.12, we plot a closed loop measurement of the Larmor frequency as a function of open loop bias Helmholtz field. We see that the extracted Larmor frequency is now centered around the Helmholtz coil field as any offset field from the environment is well compensated by the compensation coil and the *x*-axis shows the applied open loop bias field by using the conversion factor obtained from the open loop calibration.
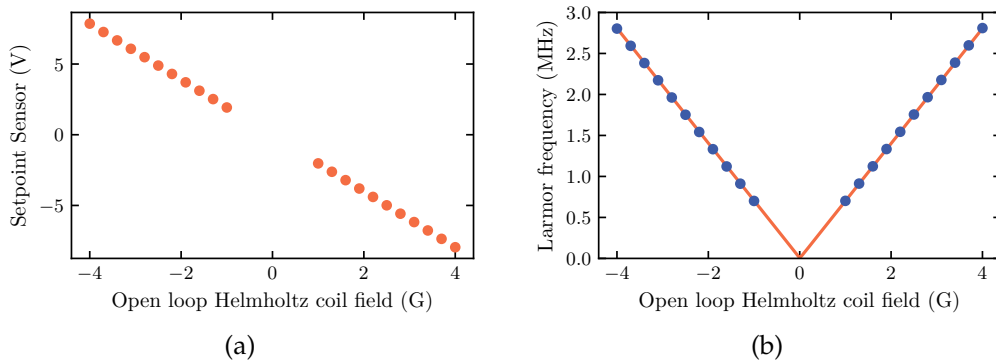
Figure 3.12: (a) Closed loop measurement of the sensor setpoint as a function of applied open loop Helmholtz coil field. (b) Closed loop measurement of the Larmor frequency as a function of open loop bias coil field.

Furthermore, since most atoms are distributed along the long axis of the cloud (~ 1 cm), a small gradient in magnetic field $\partial B_x / \partial_z$ would result in dephasing of

the spin as discussed in Sec. 2.4.2, to compensate the magnetic field gradient along the long axis of the cloud, an additional set of four parallel wires (see Fig. 3.10) is placed to create a static gradient field locally to cancel out the gradient field which improves our minimum spin coherence time from T_ϕ = 2 ms to 7 ms [59].

3.5 Spin state detection and readout

After introducing the spin preparation, we may take the spin oscillator as the starting point, and consider the detection of the collective spin precessing around a biased magnetic field along the x-axis in the lab-frame. Moreover, we further introduce the formulation for spin spectroscopy which provides the model to fully characterize our spin in Sec. 3.5.3, which allows us to extract the spin parameters, such as the spin linewidth and the Larmor frequency. Finally, we discuss the signal processing that allows one to convert the Faraday signal into the number of spin excitations. The detailed derivation are discussed previously in [59,75].

3.5.1 Faraday rotation measurement and spin signal calibration

We first present a simple example of the Faraday spin measurement. The setup used for the Faraday spin measurement is sketched in Fig. 3.13. The atomic ensemble is first initialized to the stretched state via optical pumping. The atomic spin can be driven by either the RF magnetic field produced by the RF coil in the y-direction, or circularly polarized light produced using an EOM in the z-direction. The RF drive tone is sent from a lock-in amplifier and the fast electronic switch is used to control the timing of the RF/EOM drive pulse. Due to the Faraday interaction, the spin state is mapped onto the polarization state of the light $S_y \propto F_z(t)$ and readout by the polarimeter (see Sec. 2.5). The polarimeter considered here only consists of a single HWP and a polarization beamsplitter. By setting the HWP waveplate at angle θ_H, the balanced photodetector (BpdAtom) measures a voltage proportional to $S_x \cos(4\theta_H) + S_y \sin(4\theta_H)$. To compute the Faraday angle for a given spin signal, we first need to calibrate the voltage for a given photon flux. Therefore, for $\theta_H = 0$, the local oscillator $\bar{S}_x$ is calibrated by measuring the DC voltage $V_{S_x} \propto \bar{S}_x$ as a function of laser power using an oscilloscope. To detect the spin signal encoded in S_y, the homodyne angle is set to $\theta_H = \pi/8$, such the local oscillator is balanced on both output after the beamsplitter, the photodetector outputs a time-varying AC voltage V_{S_y} that encodes the spin signal.

$$V_{S_y}(t) \propto S_y^{(\text{out})} = S_y^{(\text{in})} + \alpha_1 F_z(t) \tag{3.13}$$

Signal processing of the spin signal

The time-varying voltage spin signal of the out-going field $S_y^{(\text{out})}$ is further de-modulated by a lock-in amplifier[12] or spectrum analyzer around Ω_s. For a spin precessing in the lab frame , the measured Faraday signal V_{S_y} can be expressed in terms of slowly varying spin components $\tilde{F}_y$, $\tilde{F}_z$[13]

$$S_y^{(\text{out})}(t) = S_y^{(\text{in})}(t) + \alpha_1 S_x^{(\text{in})} \left[\tilde{F}_y(t) \sin(\Omega_s t) + \tilde{F}_z(t) \cos(\Omega_s t) \right] \qquad (3.15)$$

The demodulation corresponds to a measurement in the co-rotating frame of the spin oscillator which returns the in-phase I and the out-of-phase quadrature components of the Faraday signal. The lock-in demodulator returns the root mean
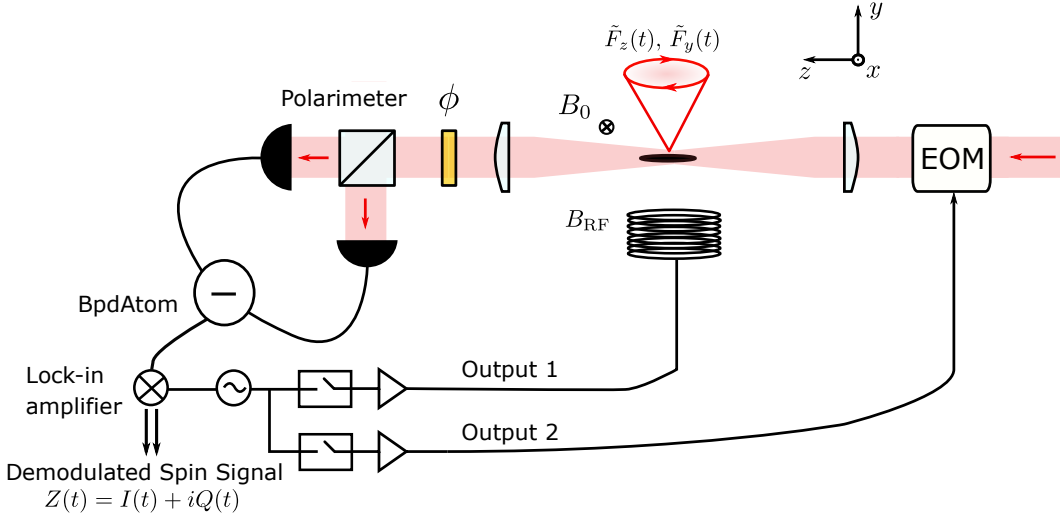
Figure 3.13: Schematic diagram of the experiment setup used to detect spin precesssion signal

---

[12]Both the spectrum analyzers and the lock-in amplifiers show excellent noise performance for our signal processing purpose, however the lock-in amplifier is used more often as the phase co-herence between the drive and detection is preserved, which provides the phase information of the spin oscillator. Whereas, the spectrum analyzer is used to measure a signal that requires a wider bandwidth.

[13]From the oscillator dynamics, $\dot{F}_z = \Omega_s F_y$, $\dot{F}_y = -\Omega_s F_z$, the spin components in the rotating frame transforms to lab frame as follows

$$\begin{aligned}
\tilde{F}_y(t) &= +F_y(t) \cos(\Omega_s t) + F_z(t) \sin(\Omega_s t) \\
\tilde{F}_z(t) &= -F_y(t) \sin(\Omega_s t) + F_z(t) \cos(\Omega_s t)
\end{aligned} \qquad (3.14)$$

square (rms) spin signal with slowly varying spin component $\tilde{F}_y(t)$, $\tilde{F}_z(t)$,

$$I(t) = \sqrt{2} \left\langle V_{S_y}(t) \cos\left(\Omega_s t\right) \right\rangle_t = \frac{\alpha_1}{\sqrt{2}} \tilde{F}_z + W_I$$

$$Q(t) = \sqrt{2} \left\langle V_{S_y}(t) \sin\left(\Omega_s t\right) \right\rangle_t = \frac{\alpha_1}{\sqrt{2}} \tilde{F}_y + W_Q$$
(3.16)

where W_I, W_Q include the input vacuum noise $S_y^{(\text{in})}$.

Moreover, one can also compute the spin excitation number $\bar{n}_s$ from the Faraday spin signal. Care was taken to ensure the proper normalization of the spin signal, which is required for a correct estimation of spin excitation. First, the rms amplitude of the demodulated signal (denoted by $V_{S_y,\text{rms}}^{50\Omega}$) is divided by $\sqrt{2}$ to obtain the peak oscillation amplitude (see Eq. 3.16) and further by a factor 2 due to input impedance mismatch between the 50 Ω input impedance of the lock-in amplifier and the high impedance $\sim$ MΩ of the oscilloscope which was used for the calibration of the $\bar{S}_x$. Including all the factors, we get the slowly varying amplitude of the Faraday signal $\bar{\theta}_F = \sqrt{2} V_{S_y,\text{rms}}^{50\Omega} / V_{S_x}$. By normalizing the spin signal by the square-root of the total spin length we obtain slowly varying amplitude of the X_s-quadrature of the spin

$$\tilde{X}_s = \frac{\bar{F}_z}{\sqrt{\langle F_x \rangle}} = \frac{2\bar{\theta}_F}{\alpha_1 \sqrt{2N}} = \frac{2V_{S_y,\text{rms}}^{50\Omega}}{\alpha_1 V_{S_x} \sqrt{N}}.$$
(3.17)

where $V_{S_y,\text{rms}}^{50\Omega}(t)$ is the demodulated signal the correction factor is taken into account. To calculate the number of spin excitations, we can apply the equipartition theorem

$$\bar{n}_s + \frac{1}{2} = \frac{\langle X_s(t)^2 + P_s(t)^2 \rangle}{2} = \bar{X}_s^2 = \frac{2\bar{\theta}_F^2}{\alpha_1^2 N}.$$
(3.18)

where $X_s(t)$ and $P_s(t)$ are the fast rotating quadratures of the spin oscillator.

3.5.2 Spin oscillator Hamiltonian

Having established the basis for the preparation and the detection of a spin signal, we provide here an in-depth description of the spin precessing around a biased field and the inclusion of a drive term for spin spectroscopy. The calculations present here follows closely to discussion in [59, 75]. As discussed in Sec. 2.1, each ^{87}Rb ground state spin behaves like a tiny bar magnet where its magnetic moment consists of an electronic part μ_j and a nuclear part μ_i. For sufficiently weak bias field, the Zeeman interaction can be treated as a perturbation term to the hyperfine interaction i.e. f remains a good quantum number [88]. Therefore, the magnetic field B couples to the hyperfine spin in the basis $|f, m_f\rangle$ with magnetic moment $-\mu_B g_f \mathbf{f}$, where g_f is the hyperfine Landé g-factor and μ_B is Bohr magneton. Consider a bias field along x, the spin oscillator Hamiltonian reads

$$H_{s,0} = \hbar \Omega_s f_x + \hbar \delta \Omega_s f_x^2$$
(3.19)

where we introduce the Larmor frequency $\Omega_s = \gamma_f B_0$ with the gyromagnetic ratio $\gamma_f = \mu_B g_f / \hbar \approx \pm 0.7$ MHz ($f = 2, 1$). The second term is the quadratic Zeeman energy shift which can be derived by Taylor expanding the Breit-Rabi formula [75, 88]:

$$\delta \Omega_s = -\frac{\Omega_s^2}{\Delta_{\text{hfs}}} \tag{3.20}$$

where Δ_{hfs} is the splitting of the hyperfine levels.

The transition frequency between adjacent Zeeman sublevels $|f, m\rangle$ and $|f, m+1\rangle$ are

$$\Omega_{m,m+1} = \Omega_s + \delta\Omega_s(2m+1) \tag{3.21}$$

For Larmor frequency $\Omega_s = 2$ MHz defined by a biased magnetic field at 2.8 G, the resulting quadratic Zeeman splitting leads to Larmor peaks equally spaced by $\Omega_{m,m+1} - \Omega_{m-1,m} = 2\delta\Omega_s = 1.1$ kHz, and thus can be easily resolved for our narrow spin linewidth ~ 100 Hz.

We may now include the coherent drive to excite the spin, which is crucial for performing the spectroscopy of the spin. As mentioned in Sec. 2.3, an external AC RF-magnetic field or a fictitious magnetic field generated from a strong circularly polarized light $B_{\text{fict}} \propto |S_z|$ can be used to manipulate the spin.

In addition to the oscillator Hamiltonian, we add the drive $H_{s,\text{drive}}$ term that describes the spin coupled to the AC drive field in the transverse direction. In this example, we consider a RF-magnetic field oscillating at drive frequency $\Omega_1 \approx \Omega_s$ in the y-direction.

$$H_s = H_{s,0} + H_{s,\text{drive}} = \hbar\Omega_s f_x + \hbar\delta\Omega_s f_x^2 + \hbar V_{\text{RF}} \cos(\Omega_1 t) f_y \tag{3.22}$$

where $V_{\text{RF}}/2$ is the Rabi frequency.

Substituting the Hamiltonian Eq. 3.22 into the quantum Liouville equation, in the rotating frame of the drive Ω_1, and we assume we work with the quantization axis along z, the evolution for spin coherences and population density matrix elements $\rho_{m,m'} = \langle m|\rho|m'\rangle$ are given by [72, 89]:

$$
\begin{aligned}
\dot{\rho}_{m,m+1} &= [\mathrm{i}(\Omega_1 - \Omega_{m,m+1}) - \gamma_2]\rho_{m,m+1} - \frac{\mathrm{i}V_{\text{RF}}}{2}C(f,m)(\rho_{m+1,m+1} - \rho_{m,m}) \\
\dot{\rho}_{m,m} &= -\gamma_1(\rho_{m,m} - \bar{\rho}_{m,m}) - \frac{\mathrm{i}V_{\text{RF}}}{2}C(f,m)(\rho_{m,m+1} - \rho_{m+1,m})
\end{aligned}
\tag{3.23}
$$

where $C(f,m) = \sqrt{f(f+1) - m(m+1)}$ is the ladder coefficient and $\bar{\rho}_{m,m}$ is the steady state spin population.

3.5.3 Magnetic resonance spectroscopy

Using the Eq. 3.23 above, we may perform the spin spectroscopy by considering the coherent drive in two regimes, i.e. continuous and pulsed regime.

Continuous spectroscopy

For continuous spectroscopy, a continuous RF drive $V_{RF} \ll \gamma_1, \gamma_2$ is applied to the spin such that the state is only weak perturbed around the large biased field along x. Since $\gamma_2 \gg \gamma_1$, the spin population $\rho_{m+1,m+1} - \rho_{m,m}$ remains approximately constant, we obtain the steady state solution

$$\rho_{m,m+1} \approx \frac{-iV_{RF}}{2} \frac{C(f,m)\left(\rho_{m+1,m+1} - \rho_{m,m}\right)}{\gamma_2 - i\left(\Omega_1 - \Omega_{m,m+1}\right)} \tag{3.24}$$

As one would expect from a forced damped oscillator, the spin oscillates at the same frequency as the drive frequency Ω_1.

$$\langle f_z(t)\rangle = \sum_{m=-f}^{f-1} \frac{C(f,m)}{2i}\left[\rho_{m,m+1}e^{-i\Omega_1 t} - \rho_{m,m+1}^* e^{i\Omega_1 t}\right] \tag{3.25}$$

From the demodulated signal, we obtain a complex fitting function for fitting the spectrum:

$$A\left(\Omega_1\right) = A_0 \sum_{m=-f}^{f-1} \frac{C(f,m)^2}{\gamma_2 - i\left(\Omega_1 - \Omega_{m,m+1}\right)}\left(\rho_{m+1,m+1} - \rho_{m,m}\right) \tag{3.26}$$

where A_0 is a scaling factor. Overall, we obtain a complex fitting function that allows one to fit the amplitude $|A(\Omega_1)|$ and phase $\text{Arg}[A(\Omega_1)]$ of the spin response as a function of the drive frequency Ω_1.

Pulsed spectroscopy

For a short, broadband pulse with bandwidth $\Delta_{BW} = \tau^{-1} \gg \gamma_1, \gamma_2, \delta\Omega_s$, i.e. larger than all other rates relevant for the spin dynamics, all transitions can be addressed simultaneously with equal Rabi frequency $V_{RF}/2$. Assuming there are no initial spin coherences $\rho_{m,m'} = 0$ for $m \neq m'$, the density matrix after the pulse at $t = \tau$ takes the form,

$$\rho_{m,m+1}(\tau) \approx \frac{-iV_{RF}\tau}{2}C(f,m)\left[\rho_{m+1,m+1} - \rho_{m,m}\right] \tag{3.27}$$

The spin evolves as $\langle f_z(\tau + t)\rangle \propto \sum_{m=-f}^{f-1} \rho_{m,m+1}(\tau)e^{(-i\Omega_{m,m+1} - \gamma_2)t} + \text{h.c.}$ after the short pulse, the Fourier transform of the spin ring down signal yields

$$f_z(\omega) \propto \sum_{m=-f}^{f-1} \frac{C(f,m)^2}{\gamma_2 - i\left(\omega - \Omega_{m,m+1}\right)}\left(\rho_{m+1,m+1} - \rho_{m,m}\right) \tag{3.28}$$

We obtain a fitting function to extract the useful parameters e.g. γ_2 and spin populations $\rho_{m+1,m+1} - \rho_{m,m}$ from the spectrum obtained from pulse spectroscopy.

3.5.4 Magneto-optical resonance spectroscopy

We may perform both the continuous and pulsed spectroscopy to verify that both models discussed above return consistent characterization results for a spin ensemble with a given orientation p.

Continuous spectroscopy

For the continuous spectroscopy, a weak continuous RF-magnetic field is applied to perturb the spin weakly around the bias field during the time which the coupling beam is switched on (see Fig. 3.14). For each drive frequency Ω_1, the de-
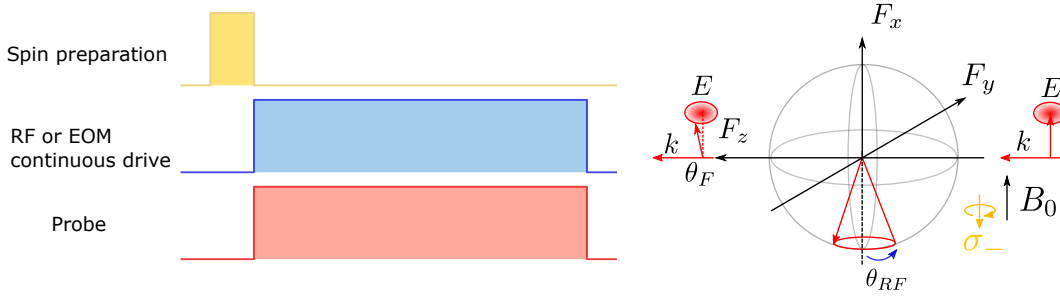
Figure 3.14: Schematic diagram of the continuous spectroscopy sequence

modulated spin signal $Z(t) = I(t) + iQ(t)$ is integrated over a chosen time interval to return the spin response. We can plot the amplitude $|A(\Omega_1)|$ and the phase $\text{Arg}[A(\Omega_1)]$ of the spin response, respectively as shown in Fig. 3.15. If the chosen integration time is increased, there is a slight increase depumping of atoms from $|f = 2, m_f = -2\rangle$ Zeeman sublevel due to spontaneous scattering, thus the coupling beam power was kept low to minimize light induced decay. The data shows four Larmor peaks equally spaced by the quadratic Zeeman splitting of ≈ 1.1 kHz which matches the theory value very well (see Sec. 3.5.2). We fit the spectra using the model Eq. 3.26. To fit the Zeeman population, we set the $m_f = 2$ level to zero. This constraint allows one to assign the extracted unnormalized population $\rho'_{m,m}$ in other Zeeman sublevels as population probability, i.e. $\rho_{m,m} = \rho'_{m,m} / \sum_{m=-f}^{f-1} \rho'_{m,m'}$ the probability sums to unity. Substituting the parameters extracted from the fit of the spectrum [see Fig. 3.15(a)] yields the $\text{Arg}[A(\Omega_1)]$ phase response as shown in Fig. 3.15(b).

Pulsed spectroscopy

For the pulsed spectroscopy, a short RF coherent drive pulse is sent to excite the spin, then we switch on the probe beam to measure the ring down of the spin precession as shown in Fig. 3.16. The time delay $\delta\tau_{RF}$ between the RF pulse and
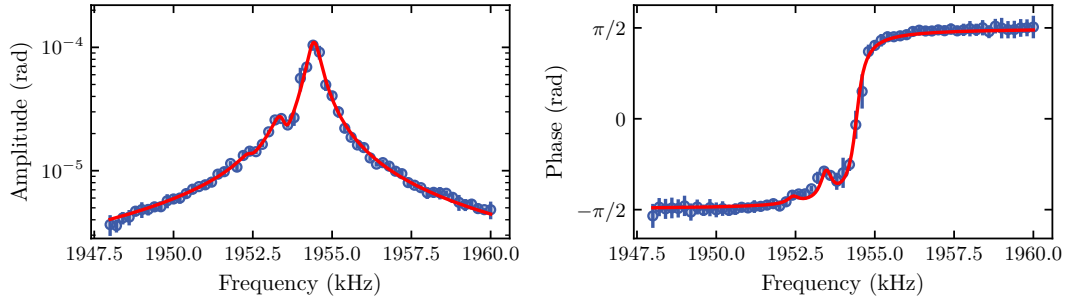
Figure 3.15: Example of a continuous spectroscopy measurement where the atomic orientation was close to unity $p = 0.9$. (a) Amplitude $|A(\Omega_1)|$ (b) Phase $\mathrm{Arg}(\Omega_1)$ of the spin response. The blue points are the measured experimental data and the red solid line shows the fit to the data.
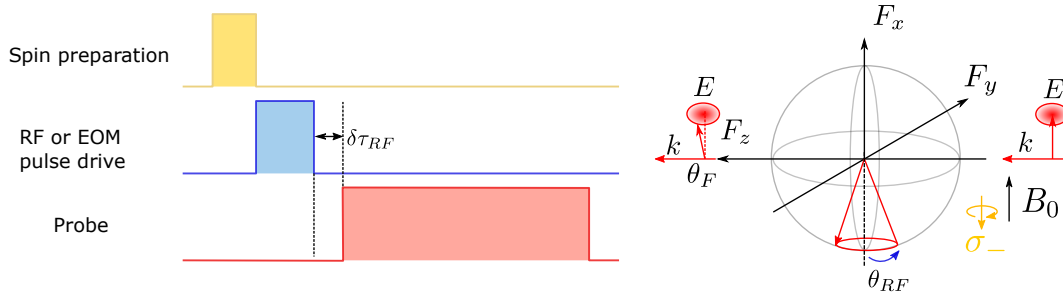
Figure 3.16: Schematic diagram of the pulse spectroscopy sequence, $\delta\tau_{RF}$ between the RF and the probe beam prevents spurious RF noise to be measured directly by the balanced detector.

probe beam[14] was set to $\sim 10\,\mu s$ to avoid spurious RF noise directly measured by the balanced detector. To process the spin signal, Fast Fourier transform (FFT) is performed over a chosen time interval of the spin ring down signal. The integration time is chosen such that there is sufficient frequency resolution for the spectrum but not so long that the spin depumps from $f = 2$ significantly. We plot the power spectral density of the spin response as a function of frequency (see Fig. 3.17). To fit the power spectral density of the spin, we use the model Eq. 3.28 to fit the Zeeman population to extract useful spin parameters. Again, the population in m_f was forced to zero as in the continuous case. We remark that the Larmor peaks look slightly non-Lorentzian shape on the wings of the spin spectrum. This is likely to be caused by the finite bandwidth of the pulse. It was observed that neither the chosen RF amplitude of the pulse nor the integration time changes the fit population significantly.

---

[14]It was observed that spurious RF noise entered the balanced detector there was no light or atom, therefore there is a small time delay before the Faraday measurement.
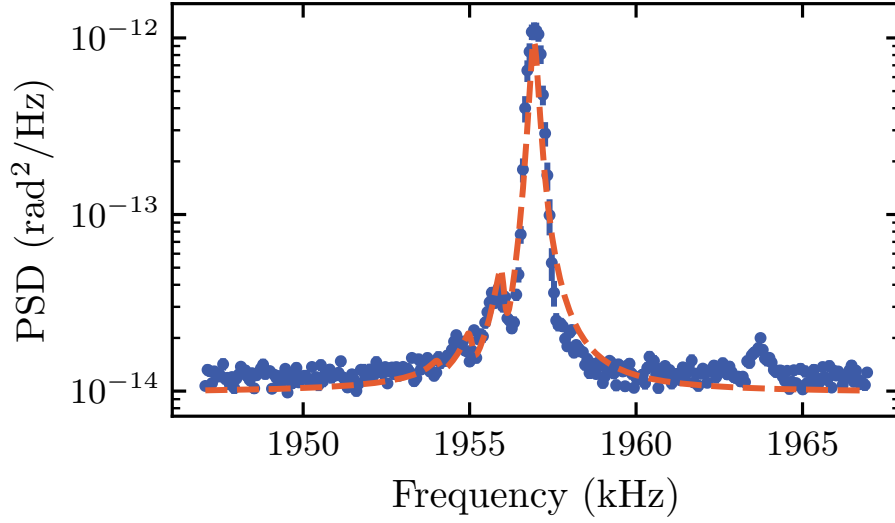
Figure 3.17: Power spectral density (PSD) of the spin, the pulse spectroscopy measurement was performed where the atomic orientation was close to unity $p = 0.9$. The small peak on the rightmost of the spectrum is contributed by the $f = 1$ atoms. The blue points are the measured experimental data and the red solid line shows the fit to the data.

Comparison between continuous and pulsed spectroscopy

For a spin ensemble with a given orientation p, the two methods should return consistent optical pumping result. As shown in Fig. 3.18, the relative occupancy of the magnetic sublevels for both approaches are plotted as a function of pumping time. For the two methods to be comparable, for both cases, we apply a small RF pulse and measure with the low probe power $P_L \sim 100 \, \mu W$ to avoid depumping at a atom light detuning of $\Delta = -2\pi \times 20 \, GHz$. Also, same integration time interval 10 ms was chosen to ensure both spin experiences same amount of depumping due to photon scattering. A slight discrepancy was observed for short pumping duration and for the lower occupied Zeeman sublevels e.g. $m_f = 1$. To study this further, more average might be required to study the effects at lower pump duration. However, we mostly work with pump duration from 300 - 500 μs where the agreement is very good. Despite the two approaches agree very well quantitatively, we also remark that continuous spectroscopy method in general requires much longer data acquisition time compared to pulsed spectroscopy, as each data point in the spectrum consists of spin response at a particular spectroscopy frequency Ω_1, however, the spectrum is also less distorted and preserved phase information. On the other hand, pulsed spectroscopy allows us to probe the Zeeman population in real time in a single experimental shot. This method is typically preferred if one wishes to perform a quick spectroscopy measurement. However, the spectrum tends to be slightly distorted probably due to the imperfection of the

pulse.
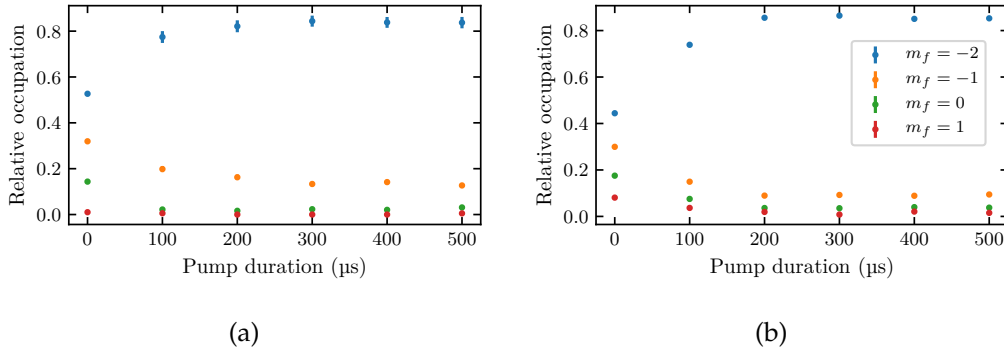
Figure 3.18: Characterization of the spin orientation p as a function of pump duration using (a) continuous spectroscopy (b) pulsed spectroscopy. For both (a) and (b), the data points in different colors correspond to the relative occupation in different Zeeman sublevel m_f.

3.6 Characterization of the spin-light interface

So far we introduce the details of our spin-light interface involving the preparation, manipulation and detection of a cold, well polarized spin ensemble. We are now ready to exploit these established tools to characterize the dispersive spin-light interaction and compare our experimental to our theoretical models discussed in Chapter 2. First, we justify that we can minimize the effect of tensor light shift on our spin which allows us to consider only the Faraday rotation. Then, we present the experiment methods used to characterize the spin oscillator.

3.6.1 Tensor light shift

As discussed in Sec. 2.3, the tensor light shift caused by the linearly polarized light induces quadratic Zeeman splittings of the magnetic sublevels by $\delta\Omega_2 \propto (3\cos(2\theta) + 1)$, where θ is the laser polarization angle defined with respect to the bias magnetic field along the x-direction. Here we show a measurement to demonstrate the dependence of tensor light shift [see Fig. 3.19(a)] as a function of the polarization angle θ. In this measurement, we first excite the spins towards the equatorial plane and perform pulse spectroscopy measurement using a strong RF pulse. In Fig. 3.19(a) measurement, we plot the PSD of the spin spectra, the spectra are offset for clarity. All spectra are measured at a detuning $\Delta = -2\pi \times 20$ GHz at a laser power of $400\,\mu\text{W}$. For $\theta = 0°$, we observe a quadratic splitting of approximately 2 kHz. For $\theta = 51°$, we observe the splitting decreases and only the quadratic splitting from the magnetic field remains. For $\theta = 90°$, the quadratic splittings due to tensor light shift acts against the quadratic shift due

(a)

(b)
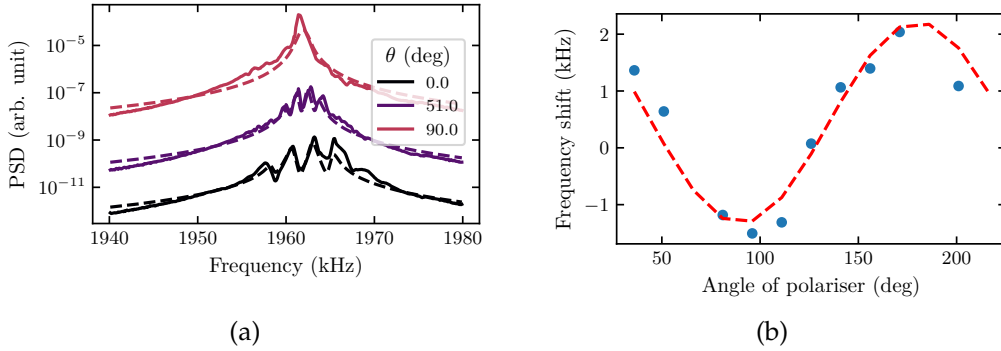
Figure 3.19: (a) PSD of the spin response. The different traces show measurements with different polarization angles. The solid lines correspond to the fits to the measured data using the model discussed in Sec. 3.5.4 (b) Plot of frequency shift $\delta\Omega_2$ as a function of the polarization angle. The blue data points correspond to the extracted resonant frequency from a Lorentzian fit. The red dashed line is a sinusoidal fit to the data.

to the magnetic field, the lines merge into one Lorentzian peak. To verify the quadratic splitting dependence as a function of polarization angle, a similar measurement was taken as a function of the polarization angle at a fixed laser power of $100\,\mu\text{W}$ at a detuning of $\Delta = -2\pi \times 10$ GHz as shown in Fig. 3.19(b). We weakly excite the spin to perform pulse spectroscopy, where only the transition $f = 2, m_f = -2 \rightarrow f = 2, m_f = -1$ transition is excited. The frequency shift is extracted by fitting a Lorentzian to the spectra. The extracted resonant frequency is plotted for different polarization angles with respect to the mean which was centered to zero. The red dashed line is a fit to the data that confirms the sinusoidal shape of the tensor light shift dependence. For the rest of the experiment, we are interested in operating with $\approx 55°$ where tensor light shift is cancelled to minimize inhomogeneous light broadening.

3.6.2 Transverse and longitudinal decoherence rate of spin

In Sec. 2.3, we discuss several mechanisms that lead to decoherence of the spin. Here, we consider the most relevant regime i.e. where the spin decoherence is dominated by spontaneous scattering. For γ_1 measurement, we perform the DC Faraday rotation measurement by scanning the probe power P_{probe} at a detuning of $\Delta = -2\pi \times 40$ GHz. Four example Faraday DC measurement traces were plotted in Fig. 3.20(a) below. The time traces are fitted with an exponential decay function. $\gamma_1 = T_1^{-1}$ is plotted as a function of probe power. γ_1 characterizes the rate at which the longitudinal spin component decays, here, this decay is mostly dominated by spontaneous scattering which causes the spin to decay into $f = 1$ or decay into higher m_f with same hyperfine number $f = 2$. For T_2 measurement, the atomic ensemble is initially polarized to the stretched state and excited to a

(a)   (b)
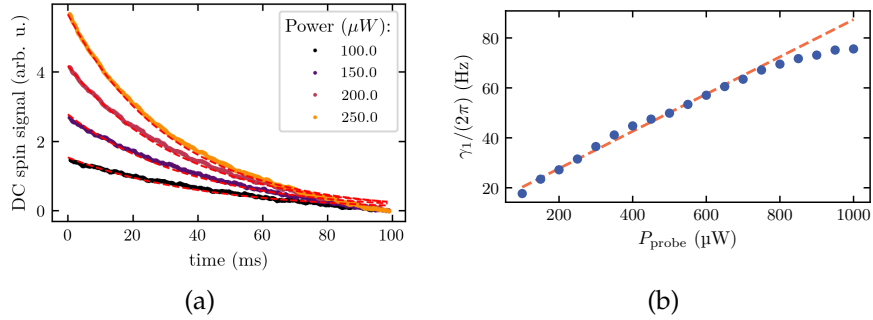
Figure 3.20: (a) DC Faraday signal plotted as a function of time, different traces show measurements with different probe powers. The red dashed lines show fits with an exponential decay. (b) Plot of longitudinal decoherence γ_1 as a function of probe power. The blue data points correspond to the extracted γ_1 determined from the exponential fit to the spin signal. The red dashed line is a linear fit to the data.

small amplitude $\theta \approx \pi/30$ where the quadratic Zeeman effect due to the magnetic field is minimal, then we measure the ring down of the spin signal using Faraday rotation. To extract the transverse decoherence rate γ_2 [see Fig. 3.21 (a)], we can perform a Fourier transform of the spin ring down signal and fit the spectrum with a Lorentzian function where the extracted linewidth yields the transverse decoherence rate γ_2. The transverse decay γ_2 scales linearly as a function of probe power as shown in Fig. 3.21(b) on the right. The fit to a Lorentzian is not perfect, this could be due to the fact that the cloud is very long and part of the cloud dephases faster than the rest of the cloud. One can see that the linewidth extrapolates to the $\gamma_{2,\mathrm{dark}}$ at low optical power. We observed that the spin linewidth is larger than that expected from theory (see Eq. 2.22).

(a)   (b)
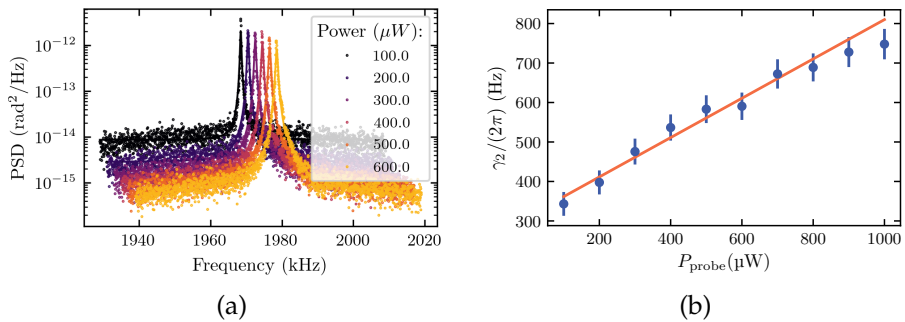
Figure 3.21: (a) PSD of the Faraday signal, measurements with different probe powers are plotted in different colors. Each solid line is a Lorentzian fit to the data. (b) Plot of transverse decoherence γ_2 as a function of probe power. The γ_2 is extracted from the fit obtained in (a) and the red line is a linear fit to the data points, where the linewidth extrapolates to $\gamma_{2,\mathrm{dark}}$ at low optical power.

3.6.3 Calibration of the vector polarizability

Vector polarizability α_1 characterizes the strength of the atom light coupling as discussed in Sec. 2.3. To calibrate the vector polarizability α_1, we aim to detect the macroscopic spin signal due to a $f = 2$ spin polarized ensemble via Faraday rotation. Here, we apply the Faraday angle obtained from the non-uniform coupling theory [see Eq. 2.45 and Eq. 2.46] to account for the overlap of the probe and ensemble mode:

$$\theta_F = \frac{\langle S_y^{(\text{out})} \rangle}{2\bar{S}_x} = \frac{1}{2}\tilde{\alpha}_1 \tilde{F}_z = \alpha_1 \langle \eta_s \rangle N$$

We see that the vector polarizability α_1 can be extracted from the macroscopic Faraday angle θ_F if N and $\bar{S}_x$ are well calibrated where $\langle \eta_s \rangle$ can be computed with the given probe-atom geometry parameters. To detect a macroscopic spin signal such that $\langle F_z \rangle \approx 2N$, atoms are initially polarized along a weak guiding field $B_x = 1\,$G in the x-direction, and the magnetic field is rotated slowly such that both the spins and magnetic field point along the z-direction within 20 ms. We then send a probe pulse of 10 ms duration to imprint the macroscopic Faraday rotation signal θ_F onto the outgoing light field $S_y^{(\text{out})}$. We show an example calibration of the vector polarizability with a probe laser detuning of $-2\pi \times 40\,$GHz. To obtain the Faraday angle, we normalize the outgoing field $S_y^{(\text{out})}$ with the average photon flux $\Phi_L = 2\bar{S}_x$ determined using a power meter. In Fig. 3.22, the Faraday angle θ_F is plotted as a function of atom number in the dipole trap N determined independently using absorption imaging[15]. We can apply a linear fit (blue dashed line) to the Faraday angle as shown in Fig. 3.22. The gradient $\theta_F/N = \alpha_{1,\text{meas}} \langle \eta_s \rangle$ of the fit allows one to compute the calibrated vector polarizability if $\langle \eta_s \rangle$ is known. Substituting the parameters of our probe-atom geometry, $w_0 = 50\,\mu$m and $w_a = 36\,\mu$m, we obtain $\langle \eta_s \rangle = 0.66$, therefore the $\alpha_{1,\text{meas}} = \theta_F/(\langle \eta_s \rangle N) = 1.05 \times 10^{-9}$ which gives a good agreement with the theoretical value $\alpha_1 = 9.35 \times 10^{-10}$ for the given detuning and probe beam waist.

3.6.4 Spin response to classical phase modulation tone

In previous sections, various methods used to characterize the spin measurement rate Γ_s are based on magnetic field control. Here, we discuss a technique that allows one to extract the spin measurement rate Γ_s and spin linewidth γ_s by recording the spin response to a weak, circularly polarized light drive. As one expects from Faraday interaction, an alternative way to drive the spin is to generate a circular polarization modulation of the light using an electro-optical phase modulator (EOM)[16]. The characterization setup is depicted in Fig. 3.23.

---

[15]Due to our high optical pumping efficiency ~ 0.9, we can assume all the atoms occupy $|f = 2, m_f = -2\rangle$.

[16]This technique is analogical to optical response of the membrane to an amplitude modulation of the probe beam present in Chapter 4
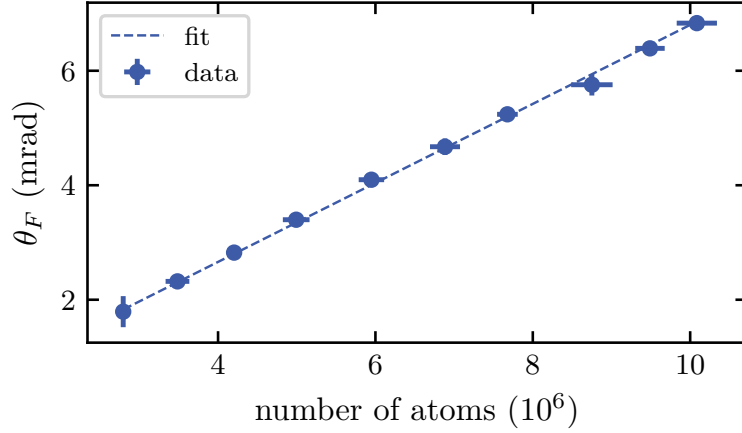
Figure 3.22: Faraday angle θ_F is plotted as a function of atom number N measured using absorption imaging. The blue dashed line corresponds to a linear fit to the data.
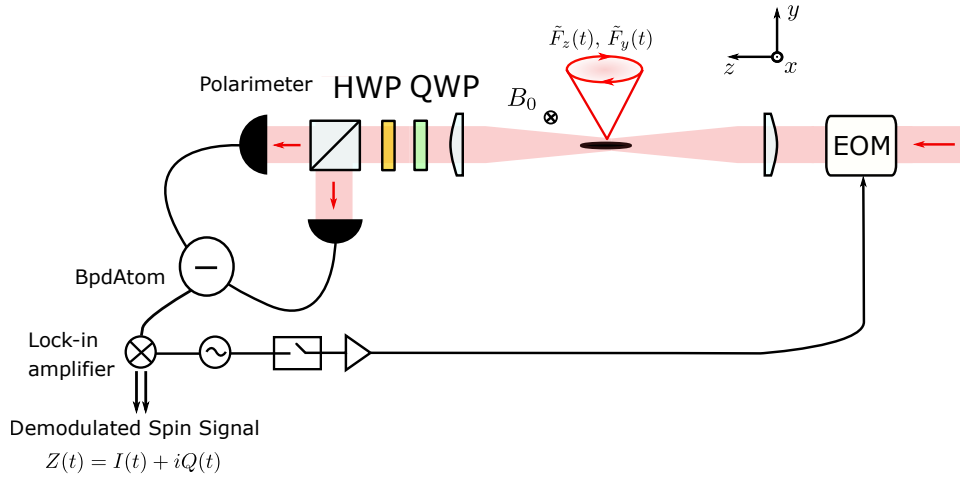
Figure 3.23: Schematic diagram of EOM spectroscopy measurement setup

The EOM consists of a birefrigent crystal where the facets is cut such that an incident horizontal polarization is $45°$ to the axis of the crystal. By applying a sinusoidal RF field oscillating at Ω_1 to the crystal, the refractive index is altered to produce polarization modulation in S_z around Larmor frequency Ω_s. At the input of the atomic ensemble, the polarization state of the light after the EOM is described by the input stokes vector $\mathbf{S}^{(\text{in})}$:

$$\mathbf{S}^{(\text{in})} = \begin{pmatrix} S_x^{(\text{in})} \\ S_y^{(\text{in})} \\ S_z^{(\text{in})} \end{pmatrix} = \begin{pmatrix} \bar{S}_x \\ 0 \\ \beta_{\text{mod}} \bar{S}_x \sin(\Omega_1 t + \phi_{RF}) \end{pmatrix} \tag{3.29}$$

where β_{mod} is the modulation depth and ϕ_{RF} is the phase of the RF modulation drive. Similar to the Faraday angle experiment, to account for possible mode mismatch, we use the input output relation from the non-uniform coupling framework (see Eq. 2.44). Therefore, the output Stokes vector $\mathbf{S}^{(\text{out})}$ at the exit of the atomic ensemble reads

$$\mathbf{S}^{(\text{out})} = \begin{pmatrix} S_x^{(\text{out})}(t) \\ S_y^{(\text{out})}(t) \\ S_z^{(\text{out})}(t) \end{pmatrix} = \begin{pmatrix} S_x^{(\text{in})}(t) \\ S_y^{(\text{in})}(t) + \tilde{\alpha}_1 S_x^{(\text{in})} \tilde{F}_z(t) \\ S_z^{(\text{in})}(t) \end{pmatrix} \tag{3.30}$$

By performing Fourier transform on both sides of Eq. 3.30 for $S_y^{(\text{out})}(t)$ and $S_z^{(\text{out})}(t)$, we obtain:

$$\begin{aligned} S_y^{(\text{out})}(\omega) &= S_y^{(\text{in})}(\omega) + \tilde{\alpha}_1 \bar{S}_x \tilde{F}_z(\omega) \\ S_z^{(\text{out})}(\omega) &= S_z^{(\text{in})}(\omega) \end{aligned} \tag{3.31}$$

where $\tilde{F}_z(\omega)$ is obtained from Eq. 2.27:

$$\tilde{F}_z(\omega) = \chi_s(\omega) \tilde{\alpha}_1 \bar{\tilde{F}}_x S_z^{(\text{in})}(\omega) \tag{3.32}$$

where the spin susceptibility reads $\chi_s = \frac{\Omega_s}{\Omega_s^2 - \omega^2 - i\gamma_s \omega}$. Since we are interested in measuring the interference between the spin response encoded in $S_y^{(\text{out})}(t) \propto \tilde{F}_z$ and the circular polarized light drive, we setup the polarimeter to detect arbitrary superposition of the spin response and optical drive tone. This is achieved by setting up the first QWP at $45°$ relative to the laser polarization and the HWP angle θ_H corresponds to a rotation of the stokes vector around S_x axis in the S_y-S_z plane. The output stokes vector before the detector $\mathbf{S}^{(\text{det})}$ after the QWP-HWP waveplate combination transforms as

$$\mathbf{S}^{(\text{det})} = \begin{pmatrix} \cos(4\theta_H) S_z^{(\text{out})} - \sin(4\theta_H) S_y^{(\text{out})} \\ \cos(4\theta_H) S_y^{(\text{out})} + \sin(4\theta_H) S_z^{(\text{out})} \\ -S_x^{(\text{out})} \end{pmatrix} \tag{3.33}$$

The balanced detector detects the $S_x^{(\text{det})}$ that encodes the spin signal. The homodyne spin signal in the frequency domain can be fitted using the transfer function:

$$\tilde{h}_s(\omega) = \cos(4\theta_H) + 4\tilde{\Gamma}_s \chi_s(\omega) \sin(4\theta_H) \tag{3.34}$$

which describes the interference between the drive and the spin response, and $\tilde{\Gamma}_s$ is the effective spin measurement rate (see Sec. 2.7). To perform the experiment, we first prepare the spin coherent state, then a probe laser with S_z modulation is applied to drive the spin to a small amplitude spin precession. To obtain a good contrast for the interference, the HWP angle $4\theta_H = 142°$ was chosen such that S_y, S_z share the same order of magnitude. The measurement was performed at a

laser atom detuning of $-2\pi \times 40$ GHz and a beam waist of 50 μm. An independent absorption imaging is performed to determine the number of atoms N loaded in the dipole trap. In Fig. 3.24(a), the spin amplitude response was plotted as a function of the drive frequency. Similar to the continuous RF spectroscopy, each data point corresponds to an integral of the spin demodulated signal at a specific drive frequency over a chosen time interval. Here, each data trace corresponds to a measurement obtained with a different laser power, the individual spectra are displayed with offset for clarity. For all laser powers, the fits using the model $|\tilde{h}_s(\omega)|$ from Eq. 3.34 shows good agreement with the data points. From the fits, the extracted measurement rate and spin damping rate were plotted as a function of the probe laser power as shown in Fig. 3.24(b). Substituting our experiment
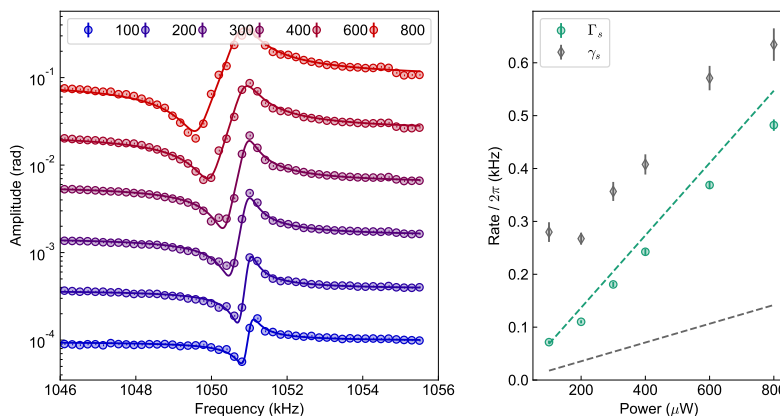
Figure 3.24: Optical response measurement. (a) Amplitude of the spin response plotted as a function of drive frequency. Different traces show measurements with different probe powers P_{probe} in μW. The traces are displayed with a vertical offset for clarity. The solid lines correspond to a fit using the transfer function (see Eq. 3.34). (b) The rates obtained from the fits to the data are plotted as a function of probe power. The dashed lines correspond to the predicted rates obtained from the non-uniform spin-light coupling model with $N = 10^7$.

parameters, $N = 10^{10}$, $\Delta = -2\pi \times 40$ GHz, and our probe-atom geometry parameters, i.e. $w_0 = 50$ μm and $w_a = 36$ μm, $\langle \eta_s^2 \rangle = 0.49$, we obtain the predicted spin measurement rate and damping rate expected from the non-uniform spin-light coupling model (see Sec. 2.7). The spin measurement rate obtained from the optical response measurement [see [Fig. 3.24(b)] is consistent with the measured vector polarizability value obtained from Faraday measurement in Sec. 3.6.3. The spin damping rate was initially dominated by magnetic inhomogeneous broadening and scales linearly with probe power due to spontaneous scattering. However, the spin damping rates were observed to be approximately four times above theory predicted values, the reason for the discrepancy is still under investigation.

3.7 Ponderomotive squeezing of light

As discussed in Sec. 2.10, with sufficiently high laser power, the quantum fluctuation $S_z^{(in)}$ in the probe laser acts as force which drives the spin and build up strong correlation between the spin oscillator and light. The ponderomotive squeezing of light is a clear signature that one can operate the spin light interface in a backaction dominated regime. To observe the ponderomotive squeezing, the measurement sequence is similar to that of EOM pulse spectroscopy, except that the classical modulation tone is disabled and the spin is now driven by the input quantum fluctuation $S_z^{(in)}$ of the probe laser. Using the QWP-HWP waveplate combination, we may choose a detector basis such that we measure an arbitrary superposition of the S_y and S_z of light. After preparing a spin coherent state, a probe pulse with a 20 ms time duration is sent to the atoms, the spin signal is recorded for the entire duration of the probe pulse using lock-in demodulation. In
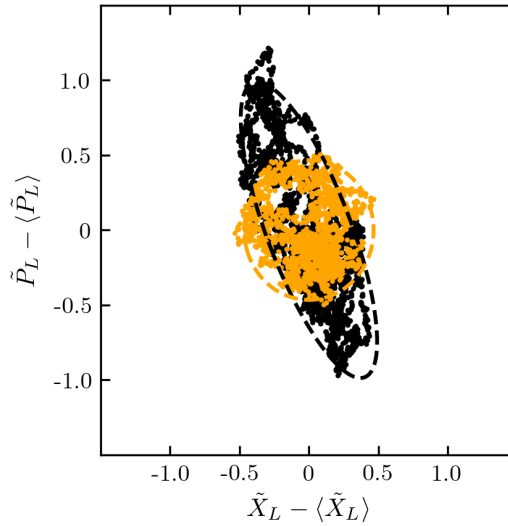
Figure 3.25: Phase space histogram of ponderomotive squeezed light, the black data points correspond to the optical quadratures measurement over the first 10 ms containing the spin signal, whereas the orange points correspond to the data points accumulated in the last 5 ms after the spin decays completely. The dashed black (orange) lines indicates the noise covariance ellipse with two standard deviation (s.d.) of the squeezed (coherent) state. From this measurement, one can clearly see the strong correlation built up between the phase quadrature and amplitude quadrature which contains the driving force and spin signal, respectively. By comparing the minor and major radius to the radius of the coherent state, the squeezing factor and anti-squeezing r_{AS} and r_S can be obtained (see the text below).

this measurement, we chose a $4\theta_H = 196°$, a laser-atom detuning of $\Delta = -2\pi \times 10$ GHz and the beam waist is $w_0 = 35\,\mu$m. In the measurement below, 13 million atoms are loaded into the dipole trap and laser power of $500\,\mu$W were used. The spin measurement can both be visualized both in $(\tilde{X}_L - \langle \tilde{X}_L \rangle, \tilde{P}_L - \langle \tilde{P}_L \rangle)$ phase space and frequency domain, respectively. We plotted the histogram of the slowly varying light quadratures $(\tilde{X}_L - \langle \tilde{X}_L \rangle, \tilde{P}_L - \langle \tilde{P}_L \rangle)$ i.e. the in phase and out of phase quadrature of the demodulated signal, respectively for different interaction time (see Fig. 3.25). In the first 10 ms of interaction, the uncorrelated input light (coherent state) is sheared to a thin uncertainty ellipse due to the strong correlation built up between atom and light. In the last 5 ms, the spin damped out due to spontaneous scattering, therefore the light returns to a coherent state. By comparing the major a and minor radius b of an ellipse (squeezed state) to the radius c of the circle (coherent state), one can compute the anti-squeezing and the squeezing of the quantum noise. For anti-squeezing (squeezing), we obtain $r_{AS} = \ln(a/c) = 0.83$ and $r_S = -\ln(b/c) = 0.42$. By substituting the values of the squeezing factors, one can compute the cooperativity for the spin as discussed in Sec. 2.10. We obtain the spin cooperativity $C_s = 2\sinh r_{AS/S} = 1.85$ or 0.86 using the anti-squeezing r_{AS} and squeezing factor r_s, respectively. In the frequency domain, the power spectral
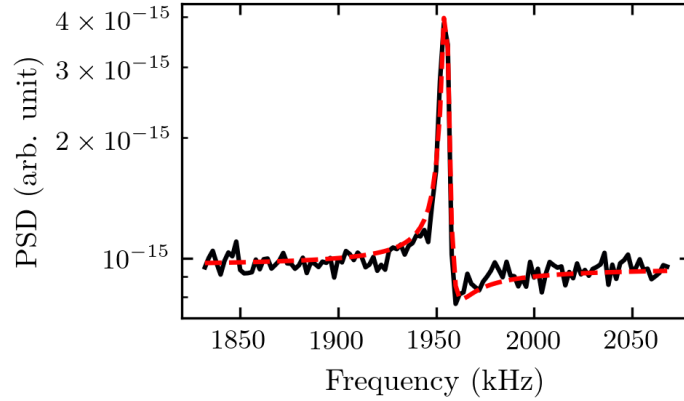
Figure 3.26: PSD of the polarization squeezed light in the frequency domain. The black data point corresponds to the measured experiment data. The red dashed line is a fit using the quantum noise model discussed in Sec. 2.10.

density of the spin detector signal is plotted in Fig. 3.26. To compute the squeezing, the amount of squeezing below shot noise is compared to the mean shot noise level, we obtain -1.3 dB below shot noise level. From the level of squeezing, the squeezing factor was found to be $r_S = 0.16$ which gives a spin cooperativity of $C_s = 0.32$. The maximum achievable squeezing is smaller than anti-squeezing should not come as a surprise, this can be accounted by noise processes that are

not correlated with noise in $S_z^{(\text{in})}$ e.g. technical noise of the laser, noise induced via tensor coupling, and so on. Overall, we observe the strong correlation between the spin and light in both the phase space and frequency domain. Using spin to squeeze light is an example of observation of quantum backaction. The generation of squeezed light using spin can be used to perform measurement beyond the standard quantum limit.

Chapter 4

Membrane light interface

This chapter covers the basic aspects of the membrane light interface, the experimental implementations and the characterization of a nanomechanical membrane inside an optical cavity used in our hybrid experiment. In this work, we operate our membrane light interface in the bad cavity regime, where information from the input field can quickly exit the cavity such that the optomechanical coupling strength is enhanced with negligible propagation delay. We describe this effective coupling of the mechanical oscillator to the cavity input/output field with the input-output formalism. Then, the experimental details of the optomechanics setup are introduced. In the end, we revisit the homodyne detection technique and characterize important optomechanical parameters, including optomechanical coupling strength, damping rate and the steady state thermal phonon occupation of the mechanical oscillator system.

4.1 Cavity optomechanics

Cavity optomechanics involves the interplay between mechanical modes and cavity modes via radiation pressure coupling. For simplicity, we restrict our treatment to a single mechanical mode interacting with a single cavity mode. In this section, we start by introducing the basic properties of the individual membrane and cavity system. Then, the simple case of an empty cavity driven by a pump field is considered. Finally, we insert the membrane which leads to the optomechanical Hamiltonian and input-output relations that describe the membrane light interaction in the hybrid experiment. The membrane part of the setup was mainly built and characterized by Thomas Karg as described in [59]. It is described here for completeness.

4.1.1 Mechanical oscillator

We introduce our first ingredient, i.e. a single vibrational mode, which is well described by the harmonic oscillator Hamiltonian H_m:

$$H_m = \frac{p_m^2}{2m_{\text{eff}}} + \frac{m_{\text{eff}}\Omega_m^2 x_m^2}{2} \tag{4.1}$$

where m_{eff} is the effective mass of a specific vibrational mode and Ω_m corresponds to its angular frequency. A more convenient notation used in the field of cavity optomechanics [80] is the dimensionless oscillator quadratures (X_m, P_m), where the mechanical position x_m and momentum p_m of the mode are normalized by their ground state fluctuations (rms spread) in position, $x_{\text{ZPF}} = \sqrt{\hbar/2m_{\text{eff}}\Omega_m}$ and momentum $p_{\text{ZPF}} = \sqrt{\hbar m_{\text{eff}}\Omega_m/2}$, respectively. In addition, we define the oscillator quadrature operators in terms of the annihilation (b_m) and creation ($b_m^\dagger$) operators of a membrane excitation,

$$X_m = \frac{x_m}{\sqrt{2}x_{\text{ZPF}}} = \frac{b_m + b_m^\dagger}{\sqrt{2}}, \quad P_m = \frac{p_m}{\sqrt{2}p_{\text{ZPF}}} = \frac{b_m - b_m^\dagger}{\sqrt{2}i} \tag{4.2}$$

which obeys the commutation relation $[X_m, P_m] = i$. This allows one to conveniently express the membrane Hamiltonian H_m in terms of oscillator quadrature (X_m, P_m) and the phonon occupation operator $n_m = b_m^\dagger b_m$, respectively:

$$H_m = \frac{\hbar\Omega_m}{2}\left(X_m^2 + P_m^2\right) = \hbar\Omega_m\left(b_m^\dagger b_m + \frac{1}{2}\right) \approx \hbar\Omega_m b_m^\dagger b_m \tag{4.3}$$

The last approximation sign neglects the contribution from the zero-point fluctuation, since the membrane is coupled to a thermal bath in a room temperature environment $\bar{n}_m \approx 10^6 - 10^7$. Furthermore, in general, the membrane oscillator is subjected to dissipation, described by the damping rate γ_m. For details of dissipation mechanisms, we refer readers to the review in [9]. It is helpful to introduce a figure of merit that characterizes the quality of the mechanical oscillator:

$$Q_m = \Omega_m/\gamma_m \tag{4.4}$$

which roughly corresponds to the number of mechanical oscillations before the membrane displacement reaches $(1/e)$ of its original amplitude upon excitation. For a simple mechanical oscillator coupled to a thermal bath, the quality factor is inversely proportional to the thermal decoherence rate $\bar{n}_{m,\text{bath}}\gamma_m$, i.e. the rate at which phonons enter from the environment and excite the mechanical oscillator out of ground state [9],

$$\dot{n}_m(t=0) = \bar{n}_{m,\text{bath}}\gamma_m \approx \frac{k_B T_{m,\text{bath}}}{\hbar Q_m} \tag{4.5}$$

where $T_{m,\text{bath}}$ is the temperature of the membrane thermal bath and k_B is Boltzmann constant. Therefore, a low temperature membrane bath and a large mechanical quality factor are beneficial for performing optomechanics experiment.

4.1.2 Optical cavity

Our second ingredient is an optical cavity. The simplest type of cavity consists of two parallel highly reflective mirrors separated by a distance l_c, where the cavity resonances angular frequencies are given by $\omega_c = 2\pi c/\lambda = m\pi c/l_c$, where λ_c is wavelength of the cavity field and m is the mode number [9] and c is the speed of light. Since the laser mode is almost perfectly matched to the cavity, we restrict our consideration to a single cavity mode frequency ω_c . The oscillator Hamiltonian (ignoring zero point energies) that describes a cavity system reads:

$$H_c \approx \hbar\omega_c c^\dagger c \tag{4.6}$$

where $c(c^\dagger)$ are the annihilation (creation) operators of intracavity photons, which obey $[c, c^\dagger] = 1$. We may also define the amplitude (X_c) and phase quadrature (P_c) for the cavity system:

$$X_c = \frac{c + c^\dagger}{\sqrt{2}}, \quad P_c = \frac{c - c^\dagger}{\sqrt{2}i} \tag{4.7}$$

where the cavity quadratures obey the commutation relation $[X_c, P_c] = i$. In general, the cavity is subjected to losses, a photon therefore stays in the cavity only for a finite lifetime τ_c, and we can introduce the cavity decay rate $\kappa = \tau_c^{-1}$.

4.1.3 Optical cavity without membrane driven by a laser

For simplicity, we first consider the optical cavity driven by a laser in the absence of a membrane to introduce the nomenclature. We use a single sided cavity, and the cavity is driven by an external drive field through the in-coupling cavity mirror at the rate κ. A well established input-output theory formulated in the level of Heisenberg picture is used to treat the coupling of an open quantum system to a stochastic noise bath. Here, we consider an optical cavity coupled to a coherent laser drive field including its quantum fluctuations, i.e. $a_L = \bar{\alpha}_L + a_L^{(in)}$. The external coupling between the laser and cavity is described by the Hamiltonian [90]:

$$H_{ext} = i\hbar\sqrt{\kappa} \int_{-\infty}^{+\infty} \frac{d\omega}{\sqrt{2\pi}} \left[a_L^\dagger(\omega)c - c^\dagger a_L(\omega) \right] \tag{4.8}$$

where $|\bar{\alpha}_L|^2 = \langle a_L^\dagger a_L \rangle = \Phi_L = P/\hbar\omega_L$ is the photon flux of the laser. For convenience, we work in a rotating frame at the laser frequency ω_L, the resulting equation of motion are called the quantum Langevin equation, which includes the stochastic noise into the evolution of the cavity field operator. Thus, the dynamics of the cavity field reads

$$\dot{c}(t) = \left(i\Delta_c - \frac{\kappa}{2} \right) c(t) - \sqrt{\kappa} a_L(t) \tag{4.9}$$

where $\Delta_c = \omega_L - \omega_c$ is the laser-cavity detuning. The steady state solution of cavity amplitude i.e. $\dot{c}(t) = 0$ reads

$$c(t) = -\frac{1}{\kappa/2 - i\Delta_c} \sqrt{\kappa} a_L \tag{4.10}$$

Similarly, we define complex coherent amplitude for the cavity field

$$\bar{c} = \frac{\sqrt{\kappa}}{\kappa/2 - \mathrm{i}\Delta_c} \bar{\alpha}_L = \sqrt{\bar{n}_c} e^{\mathrm{i}\phi_c} \tag{4.11}$$

where $\phi_c = \arctan(2\Delta_c/\kappa)$ is the cavity phase shift and the steady state cavity photon number $\bar{n}_c$ reads

$$\bar{n}_c = |\bar{\alpha}_c|^2 = \langle c^\dagger c \rangle = \frac{\kappa |\bar{\alpha}_L|^2}{(\kappa/2)^2 + \Delta_c^2} = \frac{\bar{n}_0}{1 + 4(\Delta_c/\kappa)^2} \tag{4.12}$$

where $\bar{n}_0 = 4|\alpha_L|^2/\kappa$ is the number of intracavity photons when the laser is on resonance ($\Delta_c = 0$). Eq. 4.12 simply reflects the dependence of cavity photon number on laser-cavity detuning Δ_c. We may also perform a Fourier transform on both sides of Eq. 4.9, the solution of the cavity mode $c(\omega)$ in the frequency domain reads

$$c(\omega) = -\frac{1}{\kappa/2 - \mathrm{i}(\Delta_c + \omega)} \sqrt{\kappa} a_L(\omega) = -\chi_c(\omega)\sqrt{\kappa} a_L(\omega) \tag{4.13}$$

where we introduce the cavity susceptibility:

$$\chi_c(\omega) = \frac{1}{\kappa/2 - \mathrm{i}(\Delta_c + \omega)} \tag{4.14}$$

4.2 Cavity-membrane dynamics

Having introduced the cavity-laser dynamics, we may now include the membrane in the optical cavity. We can consider a mechanical membrane vibrating inside the cavity, for a small mechanical displacement x_m, the cavity length l_c changes, we can Taylor expand the cavity resonance frequency ω_c around the mechanical equilibrium position $\bar{x}_m = 0$:

$$\omega_c(x_m) \approx \omega_c(0) + x_m \partial \omega_c / \partial x_m + \dots \tag{4.15}$$

In addition to the unperturbed cavity oscillator Hamiltonian $H_{c,0}$, the cavity Hamiltonian now includes an optomechanical interaction term H_{om} that describes the coupling between the mechanical displacement x_m to cavity photon number operator $n_c = c^\dagger c$,

$$H_c = H_{c,0} + H_{\mathrm{om}} = \hbar \omega_c(0) c^\dagger c + \hbar G x_m c^\dagger c + \dots \tag{4.16}$$

where we introduce the frequency pulling parameter $G = +\partial \omega_c / \partial x_m |_{x_m=0}$ which quantifies the amount of cavity frequency shift over a small change in mechanical displacement. Moreover, we may define the vacuum optomechanical coupling strength $g_0 = G x_{ZPF}$ which quantifies the frequency shift induced by a single phonon. In cavity optomechanics, very often we are allowed to apply the linearized approximation which greatly simplifies H_{om}, we split the cavity field into

a coherent amplitude part and a quantum part, i.e. $c \rightarrow \bar{\alpha}_c + c$. By collecting the terms with cavity field enhancement and ignoring the second order terms, the optomechanical Hamiltonian simplifies to

$$H_{\text{om}} = \hbar g_{\text{om}}(b_m + b_m^\dagger)(c + c^\dagger) \qquad (4.17)$$

where we define the optomechanical coupling strength $g_{\text{om}} = g_0 \sqrt{\bar{n}_c}$ and dropped a static term $H_{\text{om,s}} = \hbar g_{\text{om}} \sqrt{\bar{n}_c} \left(b_m + b_m^\dagger \right)$ (see Eq. 4.21 in Sec. 4.2, this static term is absorbed into $\bar{n}_c$ by redefining $\bar{x}_m$). Collecting all the Hamiltonian terms (Eq. 4.16 and Eq. 4.3) for the membrane cavity system, the overall Hamiltonian $H_{m,c}$ contains the intrinsic oscillator Hamiltonian of the individual systems and the optomechanical interaction term. For convenience, we again write the Hamiltonian in a frame rotating at the laser frequency ω_L:

$$H_{m,c} = H_m + H_{c,0} + H_{\text{om}} = \hbar \Omega_m b_m^\dagger b_m - \hbar \Delta_c c^\dagger c + \hbar g_{\text{om}} \left(b_m + b_m^\dagger \right) c^\dagger c \qquad (4.18)$$

The overall Hamiltonian $H_{m,c}$ is often seen as the starting point of cavity optomechanics. From this, we may obtain the equation of motions that describe the dynamics between membrane and an optical cavity driven by laser. We may now study the effect of the dropped static part $H_{\text{om,s}}$ and dynamical part H_{om} below.

Static phenomena

Here, we briefly discuss the effect of the static part $H_{\text{om,s}}$, as it does not play an important role for our experiment, but it does deserve a short explanation as it highlights the intrinsic non-linear relationship between mechanical displacement and optical cavity field c [9]. Consider that a photon imparts a radiation pressure force on the membrane, with a momentum exchange of $\Delta p = 2\hbar k$ due to reflection inside the cavity. For simplicity, we assume our cavity behaves as a Fabry-Perot cavity, the radiation pressure force $\bar{F}_{\text{rad}}$ reads [9]

$$\langle F_{\text{rad}} \rangle = 2\hbar k \frac{\langle c^\dagger c \rangle}{\tau_c} = \hbar \frac{\omega}{l_c} \left\langle c^\dagger c \right\rangle = \hbar G \left\langle c^\dagger c \right\rangle \qquad (4.19)$$

where $\tau_c = 2l_c/c$ is the round trip time of an optical cavity. To compute the influence of the photon on the membrane, we can write down the equation of motion of a driven mechanical oscillator:

$$\ddot{x}_m + \gamma_{\text{m}} \dot{x}_m + \Omega_m^2 x_m = \bar{F}_{\text{rad}} \qquad (4.20)$$

where $\bar{F}_{\text{rad}} = \hbar G |\alpha_c|^2$ is the average radiation pressure force due to the coherent amplitude of the cavity field $\bar{\alpha}_c$. Since the cavity frequency is detuned by the displacement of the membrane (see Eq. 4.15), we have

$$\bar{n}_c = \frac{\bar{n}_0}{1 + 4 \left(\Delta_c + G\bar{x}_m \right)^2 / \kappa^2} \qquad (4.21)$$

We see that the intracavity photon number depends on the membrane displacement in a non-linear way. We assume that the membrane displacement is very small and that the cavity quickly reaches the steady state, therefore the radiation pressure force is constant. We can redefine the membrane displacement equilibrium position $x_m \rightarrow \bar{x}_m + x_m$ and absorb this static displacement term $\bar{x}_m = \bar{F}_{\text{rad}}/m_{\text{eff}}\Omega_m^2$ into the laser cavity detuning $\Delta_c \rightarrow \Delta_c + G\bar{x}_m$.

Cavity membrane dynamics

The dynamics of the optomechanical interaction Hamiltonian is captured by:

$$H_{\text{om}} = \hbar g_{\text{om}}(b_m + b_m^\dagger)(c + c^\dagger) \tag{4.22}$$

By applying the rotating wave approximation (RWA), the above Hamiltonian allows one to access different coupling regime depending on the laser-cavity detuning [9], the optomechanical interaction can realize a beam-splitter interaction i.e. $H_{\text{BS}} \propto b_m^\dagger c + c^\dagger b_m$ for $\Delta_c = -\Omega_m$, two-mode squeezing $H_{\text{TMS}} \propto b_m c + b_m^\dagger c^\dagger$ for $\Delta_c = +\Omega_m$ and quantum non-demolition (QND) type interaction i.e. $H_{\text{om}} \propto (b_m + b_m^\dagger)(c + c^\dagger)$ for $\Delta_c = 0$. Here, in this thesis, we focus on the discussion of H_{BS} and H_{om} which is important for cooling the mechanical motion by coupling to a cold photon bath and performing QND readout of the membrane motion X_m, respectively. We may now look at the cavity-membrane dynamics generated by the optomechanical Hamiltonian H_{om}, the Langevin equations of motion for the coupled cavity-membrane dynamics read [90]:

$$\dot{c}(t) = \left(i\Delta_c - \frac{\kappa}{2}\right)c(t) - \sqrt{\kappa}a_L^{(\text{in})}(t) - i\sqrt{2}g_{\text{om}}X_m(t) \tag{4.23}$$

$$\dot{X}_m(t) = \Omega_m P_m(t) \tag{4.24}$$

$$\dot{P}_m(t) = -\Omega_m X_m(t) - \gamma_m P_m(t) - \sqrt{2}g_{\text{om}}\left[c(t) + c^\dagger(t)\right] + \sqrt{2\gamma_m}F_m^{(\text{th})}(t) \tag{4.25}$$

where we also include the thermal noise $F_m^{(\text{th})}(t)$ of the mechanical oscillator. The coupled equations can be solved readily in the frequency domain:

$$-i\omega c(\omega) = \left(i\Delta_c - \frac{\kappa}{2}\right)c(\omega) - \sqrt{\kappa}a_L^{(\text{in})}(\omega) - i\sqrt{2}g_{\text{om}}X_m(\omega) \tag{4.26}$$

$$-i\omega X_m(\omega) = \Omega_m P_m(\omega) \tag{4.27}$$

$$-i\omega P_m(\omega) = -\Omega_m X_m(\omega) - \sqrt{2}g_{\text{om}}\left[c(\omega) + c^\dagger(-\omega)\right] + \sqrt{2\gamma_m}F_m^{(\text{th})}(\omega) \tag{4.28}$$

Using the first two equations Eq. 4.26 and Eq. 4.27 above, we can express the steady state cavity amplitude c and P_m in terms of X_m, respectively:

$$c(\omega) = -\chi_c(\omega)\left(\sqrt{\kappa}a_L^{(\text{in})} + i\sqrt{2}g_{\text{om}}X_m(\omega)\right) \tag{4.29}$$

$$P_m(\omega) = \frac{\omega X_m}{i\Omega_m} \tag{4.30}$$

Substituting Eq. 4.29 and Eq. 4.30 into the equation of motion of P_m (see Eq. 4.28), we obtain the solution of X_m in the frequency domain,

$$X_m(\omega) = \chi_{m,\text{eff}}(\omega) \left[\sqrt{2\gamma_m} F_m^{(\text{th})}(\omega) + \sqrt{2\kappa} F_L^{(\text{in})}(\omega) \right] \tag{4.31}$$

where we define the modified membrane susceptibility χ_m:

$$\chi_m(\omega) = \frac{\Omega_{\text{m}}}{\mathcal{D}_{m,\text{eff}}(\omega)} \tag{4.32}$$

where $\mathcal{D}_{m,\text{eff}}$ includes a denominator $\mathcal{D}_m$ which contains the intrinsic membrane susceptibility $\mathcal{D}_m = \Omega_m/\chi_{m,0}$ and a correction term $\mathcal{C}_m$ that modifies the membrane susceptibility [91]:

$$\mathcal{D}_{m,\text{eff}} = \mathcal{D}_m + \Omega_m \mathcal{C}_m(\omega) \tag{4.33}$$

where the correction term $\mathcal{C}_m(\omega)$ is defined as

$$\mathcal{C}_m(\omega) = -2ig_{\text{om}}^2 \left[\chi_{\text{c}}(\omega) - \chi_{\text{c}}^*(-\omega) \right] \tag{4.34}$$

and we also define the optical vacuum noise of the laser as

$$F_L^{(\text{in})}(\omega) = \chi_{\text{c}}(\omega) g_{\text{om}} [a_L^{(\text{in})} + a_L^{\dagger(\text{in})}(-\omega)] \tag{4.35}$$

The correction term $\mathcal{C}_{\text{m}}(\omega)$ arises from the optomechanical interaction between the laser and the mechanical oscillator. For weak coupling $g_{\text{om}} \ll \kappa$, the coupling to the cavity field effectively modifies the mechanical oscillator frequency Ω_m and damping rate γ_m by $\delta\Omega_{\text{om}}, \delta\gamma_{\text{om}}$, respectively:

$$\begin{aligned} \delta\Omega_{\text{om}} &= \text{Re}\left[\mathcal{C}_{\text{m}}\left(\omega = \Omega_{\text{om}}\right) \right]/2 \\ \delta\gamma_{\text{om}} &= -\text{Im}\left[\mathcal{C}_{\text{m}}\left(\omega = \Omega_{\text{m}}\right) \right] \end{aligned} \tag{4.36}$$

This effect is called the dynamical backaction as the presence of the mechanical oscillator modifies the cavity field which in turns causes a retarded radiation pressure force that acts back on the mechanical oscillator motion. For the non-resolved sideband limit i.e. $\kappa \gg \Omega_{\text{m}}$, this amounts to

$$\delta\Omega_{\text{om}} \approx 8g_{\text{om}}^2 \frac{\Delta_c}{\kappa^2 + 4\Delta_c^2} \tag{4.37}$$

$$\delta\gamma_{\text{om}} \approx -64g_{\text{om}}^2 \frac{\Delta_c \kappa \Omega_m}{\left(\kappa^2 + 4\Delta_c^2\right)^2} \tag{4.38}$$

The above equations deserves some explanations. $\delta\Omega_{\text{om}}$ indicates an optical spring effect that changes the spring constant of the mechanical oscillator due to the optomechanical interaction. Overall, both changes are linearly proportional on input laser power in front of the cavity. In analogy to classical spring where

stiffness $k = m_{\text{eff}}\Omega_m^2$, it means the mechanical oscillator is either stiffened $\Delta_c > 0$ or softened for red detuning $\Delta_c < 0$, respectively. On the other hand, the mechanical damping rate is dependent on laser-cavity detuning Δ_c. For a red detuning $\Delta_c < 0$, $\delta\gamma_{\text{om}} > 0$, the laser induces damping to the mechanical motion. Whereas for blue detuning $\Delta_c > 0$, we get amplification $\delta\gamma_{\text{om}} < 0$, which creates heating for the membrane. As we will see later (see Sec. 4.6.1), the laser cavity lock is stabilized to the red detuning regime for precooling of the mechanical oscillator (see Chapter 6).

4.2.1 Input-output relation, mechanical spectrum

After introducing the effect of dynamical backaction for non-zero detuning ($\Delta_c \neq 0$), we may now consider the above cavity-membrane dynamical equations (see Eq. 4.23 and Eq. 4.24) in the non-resolved sideband limit i.e. $\kappa \gg \Omega_m$ and the laser resonant to the cavity ($\Delta_c = 0$). From Eq. 4.23, one can show that the steady-state solution of cavity field reads

$$c(t) = -\frac{2}{\sqrt{\kappa}}a_L^{(\text{in})} - \frac{i2\sqrt{2}g_{\text{om}}}{\kappa}X_m \tag{4.39}$$

According to input-output relation $a_L^{(\text{out})}(t) = a_L^{(\text{in})}(t) + \sqrt{\kappa}c(t)$, the output light quadrature reflected from the cavity reads:

$$X_L^{(\text{out})} = -X_L^{(\text{in})} \tag{4.40}$$

$$P_L^{(\text{out})} = -\left[P_L^{(\text{in})} + \frac{4g_{\text{om}}}{\sqrt{\kappa}}X_m\right] = -\left[P_L^{(\text{in})} + 2\sqrt{\Gamma_m}X_m\right] \tag{4.41}$$

where we introduced the membrane measurement rate:

$$\Gamma_m = \frac{4g_{\text{om}}^2}{\kappa} = \left(\frac{4g_0}{\kappa}\right)^2\Phi_L \tag{4.42}$$

Similarly, the equation of motion of mechanical oscillator takes the form:

$$\dot{X}_m = \Omega_m P_m$$
$$\dot{P}_m = -\Omega_m X_m - \gamma_m P_m - 2\sqrt{\Gamma_m}X_L^{(\text{in})} + \sqrt{2\gamma_m}F_m^{(\text{th})} \tag{4.43}$$

The above input output relation for light field and the equation of motion for membrane are therefore described by the effective optomechanical Hamiltonian:

$$H_{m,\text{eff}} = \hbar 2\sqrt{\Gamma_m}X_m X_L \tag{4.44}$$

Likewise, we can write down the solution in the frequency domain by performing Fourier transform on both sides for Eq. 4.43 in the non-resolved sideband limit:

$$X_m(\omega) = \chi_m(\omega)\left[\sqrt{2\gamma_m}F_m^{(\text{th})}(\omega) - 2\sqrt{\Gamma_m}X_L^{(\text{in})}(\omega)\right] \tag{4.45}$$

Using the Wiener-Khinchin theorem and equipartition theorem [9,59] i.e. $\langle X_m^2 \rangle = \langle P_m^2 \rangle$, the variance of membrane position quadrature can be easily obtained,

$$\frac{1}{2}\langle X_m^2 + P_m^2 \rangle = \frac{1}{2} + \bar{n}_{\text{th}} + \frac{\Gamma_m}{\gamma_m} \tag{4.46}$$

The variance is proportional to the membrane temperature, which consists of zero point energy (1/2), thermal phonons from the room temperature environment and phonons caused by measurement backaction. Similarly, the variance can be computed in the time domain (see chapter 5) to obtain the phonon occupation.

4.3 Experimental setup

Here, we discuss the design of our mechanical oscillator and provide a brief description of our optomechanics setup used in the hybrid atom-membrane experiment. For detailed design of optical cavity and membrane, we refer readers to [59].

4.4 Silicon-nitride (SiN) nanomechanical membrane

We present a brief overview of the SiN membranes that were designed and characterized by our previous work [59,85,86]. The choice of our mechanical oscillator is silicon nitride (SiN) membranes [see Fig. 4.1(a)]. Thanks to their high tensile stress and low thickness ($\approx$ 100 nm), bending or clamping losses are minimized. Moreover, the SiN film is surrounded by a phononic bandgap [92, 93] structure made of silicon which effectively shields noise from propagating into our mechanical device [see Fig. 4.1(b)]. These factors allow our mechanical oscillators routinely achieve a high quality $Q_m > 10^6$ even in a room temperature environment. The choice of a thinkness of 100 nm which enables high reflectivity $r_m \approx 0.6$ and low absorption $\approx 10^{-6}$ at 780 nm makes these devices an excellent choice for optomechanics experiments. The vibrating element is the a square SiN film [see Fig. 4.1(a)] suspended from a Si substrate. In general, an out of plane displacement of the square SiN film excites a superposition of out-of-plane drum normal modes $u_{j,k}(x,y)$ [see Fig. 4.1(b)] defined by the boundary condition of the Silicon thin film:

$$u_{jk}(x,y) = \sin(j\pi x/a)\sin(k\pi y/a) \tag{4.47}$$

where $x, y \in [0, a]$ are in-plane coordinates and (j, k) are mode indices of the normal modes. The mechanical displacement is given by the sum over all the normal drum modes:

$$u(x,y) = \sum_{jk} u_{jk}(x,y)z_{jk} \tag{4.48}$$

where z_{jk} is defined as the out of plane displacement parallel to the optical axis. Each drum mode can be represented by a harmonic oscillator with displacement
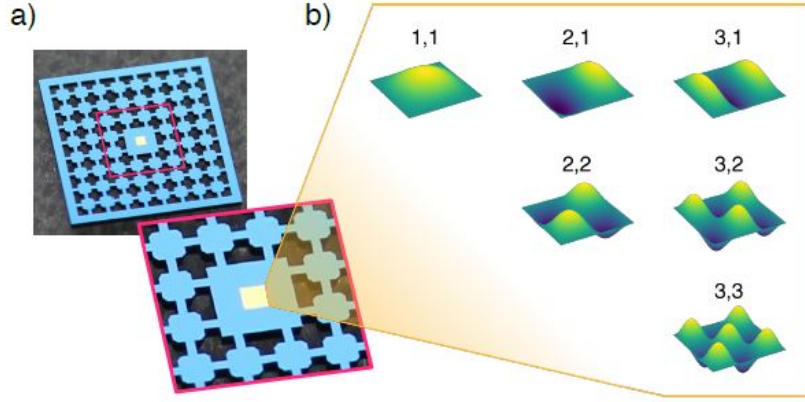
Figure 4.1: (a) Photograph of a square silicon nitride (SiN) membrane thin film (yellow square) suspended from a Silicon (Si) Substrate. The size of the silicon chip is 5×5 mm^2 and each side of the membrane is 270 μm. (b) A close up shot of the square membrane is shown as an inset, indicating the square drum modes supported by the mechanical oscillator. [Figure taken from [14]]

z_{jk} and momentum p_{jk} and their respective annihilation b_{jk} and creation $b_{jk}^\dagger$ operators. The membrane oscillator Hamiltonian is given by the linear combination of the individual oscillator Hamiltonians H_{jk} and can be written as:

$$H_m = \sum_{j,k} H_{j,k} = \sum_{j,k} \hbar \Omega_{jk} \left(b_{jk}^\dagger b_{jk} + \frac{1}{2} \right) \tag{4.49}$$

where $\Omega_{j,k}$ are the eigenfrequencies of the square drum modes:

$$\Omega_{jk} = \Omega_{11} \sqrt{\frac{j^2 + k^2}{2}} \tag{4.50}$$

where $\Omega_{11} = \frac{\pi}{a} \sqrt{\frac{2S}{\rho}} \sim 1$ MHz, the fundamental mode of our mechanical oscillator is determined by density ρ and tensile stress S of the SiN film. In the experiment, we are interested in coupling light to a particular membrane mode via radiation pressure. To select a particular membrane mode, it is intuitive to introduce an overlapping parameter η_{jk} that describes the mode matching between the cavity and mechanical mode [59]:

$$\eta_{jk} = \left| \int_0^a \int_0^a u_{jk}(x,y) |u_{\text{opt}}(x,y)^2| \, dx \, dy \right| \tag{4.51}$$

where $|u_{\text{opt}}(x,y)|^2 = 2/\pi w_0^2 \exp(-2\frac{x^2+y^2}{w_0^2})$ is the intensity distribution of the fundamental TEM$_{00}$ cavity mode with waist w_0. The experimentally observed optomechanical coupling strength relates to theory by $G_{j,k}^{\text{exp}} = \eta_{j,k} G_{j,k}^{\text{theory}}$. We are
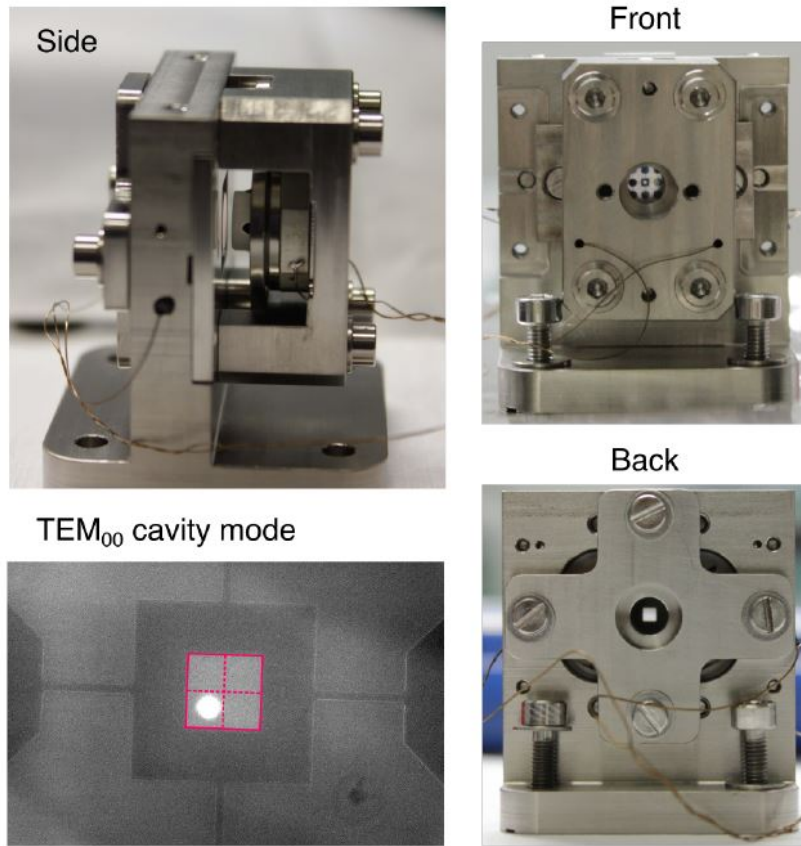
Figure 4.2: Photographs of the optomechanics system. Top left: side view of the cavity without the membrane. Top right: front view of the cavity with the membrane inserted. Bottom left: image of the membrane with the fundamental cavity mode aligned to the membrane (2,2) mode. Bottom right: the back view of a NORCADA membrane. [Figure taken from [59]]

interested in coupling to a higher order symmetric mode as they have a a higher quality factor. Therefore, by adjusting the membrane position relative to the cavity mode carefully without clipping (see Fig. 4.2), we target the symmetric (2,2) mode with natural frequency of $\Omega_m \sim 2\pi \times 1.957$ MHz. In addition to the mode selection, the bandgap used in this experiment is centered around the (2,2) mechanical mode, this means nearby mechanical modes e.g. (1,1), (3,3) and spurious frame modes are heavily suppressed.

4.4.1 Optomechanics setup

The optical setup used for the optomechanics experiment is sketched in Fig. 4.3. Overall, there are three laser beams: the cavity lock beam, the optomechanics and
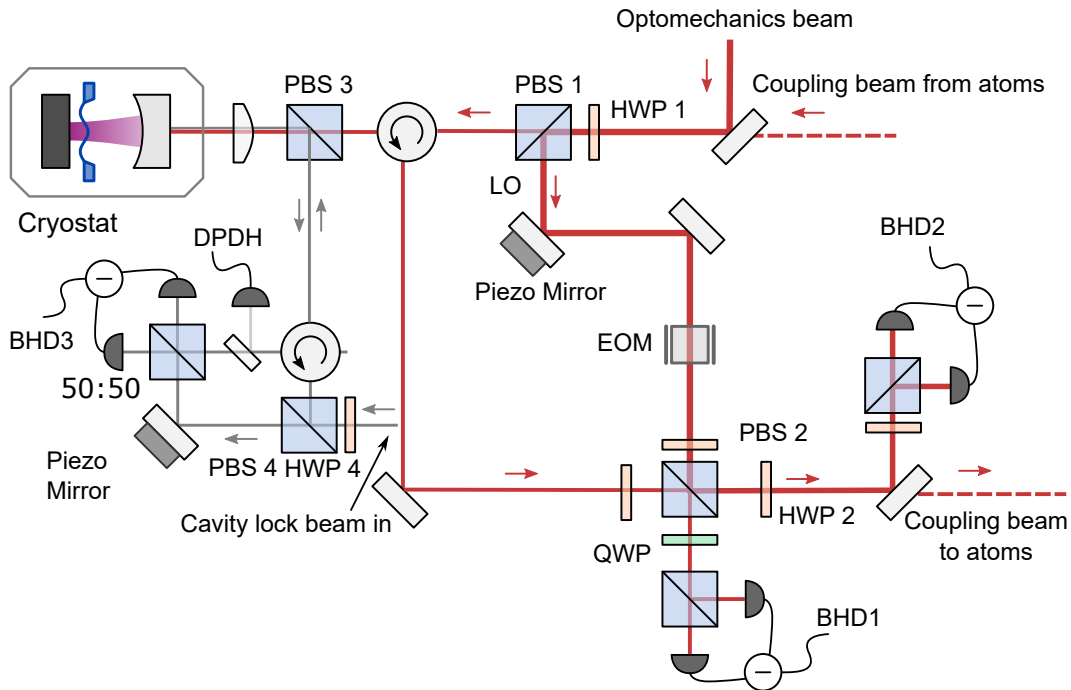
Figure 4.3: Schematic diagram of the optomechanics setup, the thickness of the line indicates the power of the laser beam [Figure adapted from [59]]

the coupling beams. The cavity lock beam carrying a phase modulation tone is sent with a vertical polarization and reflected from the cavity. Part of this reflection is detected directly on a fast photodiode (DPDH) for cavity locking using standard Pound-Drever-Hall locking scheme. The part that coupled into the cavity interacts with the membrane and leaks out again before recombining with the local oscillator of the lock beam to perform independent homodyne detection of the membrane motion using BHD3. The phase of this interferometer is stabilized using a piezo mirror on the local oscillator arm. Moreover, the lock beam is red-tuned from the cavity resonance to provide initial optomechanical cooling to the membrane oscillator. The optomechanics beam and coupling beam play a similar role, they are both set to $\Delta_c \approx 0$ to perform QND readout of the membrane quadrature X_m. The main difference is that the coupling beam carries the atomic spin signal (see Chapter 5). There is a flip mirror that allows one to switch between optomechanics beam or the coupling beam. For both the coupling beam and optomechanics beam, the laser first enters a Mach Zehnder interferometer where the first half waveplate (HWP1) combined with a polarization beamsplitter (PBS1) controls the amount of LO of the beam versus quantum signal going into either the optical cavity arm or the reference arm. Similar to the homodyne detection for the lock beam, the light from the two arms recombine at a second beamsplitter (PBS 2), the low frequency part (below 10 kHz) of the optical interfer-
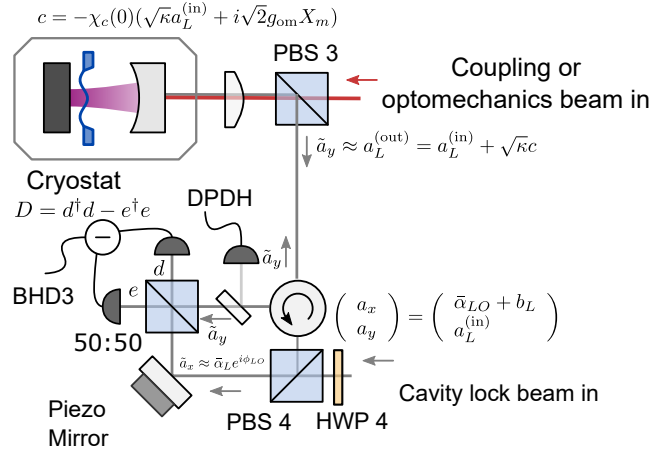
Figure 4.4: Details of the homodyne detection scheme using the cavity-lock interferometer. [Figure adapted from [59]]

ence are used for feedback stabilization of the phase, whereas the high frequency part of the signal at $\Omega_m \approx 2\pi \times 1.957$ MHz is used for detection of the membrane signal. The phase modulation imprinted onto the light is then transduced into an intensity modulation detectable on a balanced photodetector (BHD2).

4.5 Characterization of mechanical oscillator

As shown in previous sections, the vibrational state of the mechanical oscillator is imprinted on the phase of the light reflected from the cavity. The conversion from a phase fluctuation that encodes the membrane to an intensity fluctuation detectable on a balanced photodiode using a Mach Zehnder interferometer can be illustrated by a homodyne detection model. The result allows one to calibrate the phonon occupation $\bar{n}_m$ of membrane oscillator and derive an optical transfer function to extract the important parameters of membrane oscillator e.g. Γ_m, γ_m.

4.5.1 Homodyne detection model

The principle of homodyne detection is best illustrated with a Mach Zehnder interferometer, here, we take our cavity lock interferometer as an example (indicated by the grey lines in Fig. 4.4). The same model also applies for the interferometer of the coupling or optomechanics beam. At the input of the interferometer, the cavity lock beam consists of horizontally polarized a_x and vertically polarized fields a_y, respectively. Here, we may consider the x-polarized field as a coherent state amplitude with its quantum fluctuation i.e. $a_x = \bar{\alpha}_L + b_L$ and y-polarized field with quantum fluctuation $a_y = a_L^{(in)}$, respectively. The splitting ratio of the orthogonally polarized fields is determined by the first half waveplate (HWP4) at an angle θ_H,

the above transformation of light fields can be described by

$$\begin{pmatrix} \tilde{a}_x \\ \tilde{a}_y \end{pmatrix} = \begin{pmatrix} \cos(2\theta_H) & \sin(2\theta_H) \\ \sin(2\theta_H) & -\cos(2\theta_H) \end{pmatrix} \begin{pmatrix} a_x \\ a_y \end{pmatrix} \tag{4.52}$$

where the ($\sim$) tilde above the polarization modes correspond to the fields after the first PBS (PBS4). Ideally, the splitting ratio should be chosen such that most input light goes to the local oscillator arm, however, one must still ensure there is enough laser power going to the optical cavity for the linearization approximation of the optomechanical Hamiltonian to be valid (see Sec. 4.2). For a small half-waveplate angle $\theta_H \ll 1$, after the first PBS (PBS4), the transmitted port is dominated by horizontally polarized coherent state field $\bar{\alpha}_{LO} = \cos(2\theta_H)\sqrt{\Phi_{LO}} \approx \sqrt{\Phi_{LO}}$, and the reflected light is dominated by vertically polarized y-polarized quantum field $a_L^{(in)}$, respectively. We note the the part of the LO is splitted into the signal arm, i.e. $\bar{\alpha}_L = \sqrt{\Phi_L}\sin(2\theta_H)$, where the photon plus behind the reflected port reads $\Phi_L = \Phi_0\sin^2(2\theta_H)$. Therefore, we label the beam path behind the transmission and reflection ports as local oscillator and signal beam, respectively. After the first PBS (PBS4), the sum of the photon flux must be conserved before and after the polarization beamsplitter assuming no optical losses, i.e. $\Phi_{LO} + \Phi_L = \Phi_0[\cos^2(2\theta_H) + \sin^2(2\theta_H)] = \Phi_0$. The LO and signal field propagate in their respective beam paths, the LO field obtains a phase shift from a piezo-controlled mirror $\tilde{a}_x \rightarrow \bar{\alpha}_L e^{i\phi_{LO}}$, whereas the signal field enters the cavity, interacts with the membrane and the output field transforms according to the input-output relation: we get $\tilde{a}_y \approx a_L^{(out)} = a_L^{(in)} + \sqrt{\kappa}c$ where $c = -\chi_c(0)(\sqrt{\kappa}a_L^{(in)} + i\sqrt{2}g_{om}X_m)$ obeys Eq. 4.23. Here, we define the phase shift on the signal arm as ϕ_L. The two fields then recombines at a second beamsplitter with 50:50 splitting ratio such that the two ports of the balanced photodetectors see the same amount of local oscillator, this allows common mode noise to be rejected. The field operators before each port of the balanced photodetector (BHD3) reads:

$$\begin{pmatrix} d \\ e \end{pmatrix} = \begin{pmatrix} 1/\sqrt{2} & 1/\sqrt{2} \\ 1/\sqrt{2} & -1/\sqrt{2} \end{pmatrix} \begin{pmatrix} \tilde{a}_x \\ \tilde{a}_y \end{pmatrix} \tag{4.53}$$

We may again apply the linearization approximation i.e. $a_x \rightarrow \langle \alpha_{LO} \rangle + b_L$, we get

$$D = d^\dagger d - e^\dagger e \tag{4.54}$$

$$\approx \sqrt{2\bar{\alpha}_{LO}}\left[\tilde{X}_L^{(out)}\cos(\Delta\phi) + \tilde{P}_L^{(out)}\sin(\Delta\phi)\right] \tag{4.55}$$

where $\Delta\phi = \phi_{LO} - \phi_L$ is the relative phase between the LO and the signal arm. This result shows that by locking the interferometer at phase $\Delta\phi = 0$ or $\pi/2$, we only measure the amplitude quadrature $\tilde{X}_L^{(out)}$ or the phase quadrature $\tilde{P}_L^{(out)}$ of the light, respectively. To see how the interferometer transforms the input field, we may express d, e light field after the last 50:50 beamsplitter in terms of the original light basis at the input of the interferometer, i.e. we express the rotated

light quadratures $(\tilde{X}_L^{(\text{out})}, \tilde{P}_L^{(\text{out})})$ in terms of the unrotated light quadrature basis $(X_L^{(i)}, P_L^{(i)})$ where $i \in (x, y)$:

$$
\begin{aligned}
D &= d^\dagger d - e^\dagger e \\
&= \sqrt{2\Phi_{LO}} \left[\cos(\Delta\phi) \left((\sqrt{2}\langle\alpha_{LO}\rangle + X_L^{(x)}) \sin(2\phi) - X_L^{(y)} \cos(2\phi) \right) \right. \\
&\quad \left. + \sin(\Delta\phi) \left(P_L^{(x)} \sin(2\phi) - P_L^{(y)} \cos(2\phi) - \frac{\sqrt{\kappa\kappa}}{(\kappa/2)^2 + \Delta_c^2} g_{\text{om}} X_m \right) \right]
\end{aligned}
\tag{4.56}
$$

where $\Phi_{LO} = \Phi_0 \cos^2(2\phi)$ is the photon flux of the local oscillator arm and the optomechanical coupling strength contains $\bar{n}_c$ which is proportional to input photon flux in front of the cavity i.e. $\Phi_L = \Phi_0 \sin^2(2\phi)$. Since part of the drive field at cavity input $\tilde{a}_y$ comprises both a_x and a_y (due to PBS4), the corresponding X_m would be driven also by quantum fluctuations b_L in a_x. The result is much simpler to understand if we consider the special case of $\Delta\phi = 0$ or $\pi/2$. For $\Delta\phi = 0$, only the local oscillator and its quantum fluctuation in amplitude enter and no membrane signal is detected i.e. $D = \sqrt{2\Phi_{LO}} \left[(\sqrt{2}\langle\alpha_{LO}\rangle + X_L^{(x)}) \sin(2\phi) - X_L^{(y)} \cos(2\phi) \right]$. On the other hand, for $\Delta\phi = \pi/2$ and $\Delta_c = 0$, the amplitude part of LO and the amplitude quantum fluctuations of the lasers vanish, only the shot noise of the laser from the phase quadrature and the membrane signal are observed. The detector signal, ignoring shot noise reads:

$$
D(\Delta\phi = \pi/2)(t) = 4\frac{g_0}{\kappa}\sqrt{2}X_m(t)\eta_c D_{\max}
\tag{4.57}
$$

where $D_{\max} = 2\sqrt{\Phi_{LO}\Phi_L}$ is the homodyne contrast calibrated in the next section (see Sec. 4.5.2) and η_c is the incoupling efficiency as not all the signal light enters the cavity is reflected back from cavity after interacting with the membrane.

4.5.2 Calibration of the membrane signal contrast

Having established the basic homodyne technique, however, the measured homodyne signal $V(t) \propto D(\Delta\phi = \pi/2)$ is a time-varying voltage signal that encodes the displacement X_m of the membrane oscillator. In our hybrid experiment, we are interested in the calculation of the number of membrane phonons $\bar{n}_m$. This requires one to first convert the raw voltage signal $V_m(t)$ into membrane oscillator quadrature $X_m(t)$. In the following, we continue with the example of measurement using the cavity lock beam. The calibration factor takes the form as shown in Eq. 4.57, in practice, to find out the calibration factor i.e. $\eta_c D_{\max}$, we first leave the optical cavity unlocked, and move the cavity piezo mirror such that the laser is off-resonant with the cavity, therefore we see a direct interference between the directly reflected light from in-coupling mirror from the signal arm and local oscillator in the LO arm. This gives the maximal homodyne contrast $D_{\max} = 2\sqrt{\Phi_{LO}\Phi_L}\cos(\Delta\phi)$ as

the cavity acts almost as a perfect mirror. Next, instead of scanning the piezo mirror of the local oscillator arm, we can also scan the cavity piezo mirror to sweep across the cavity resonance to obtain a homodyne contrast. The phase of the interferometer is stabilized at $\Delta\phi = \pi/2$ via closed-loop feedback on the position of the piezo-mirror in the LO arm. By sweeping across the cavity resonance at kHz rate, most of the light enters the optical cavity and reflects back with a phase $\phi_c = \arctan\left[\frac{\kappa\Delta_c}{(\kappa/2)^2+\Delta_c^2}\right]$, then the light reflects back and interferes with the LO beam at a 50:50 beamsplitter to give a homodyne contrast D_{cavity} that has a dispersive shape from the phase response of the cavity. Comparing this homodyne contrast D_{cavity} with the previously homodyne contrast D_{max}, the in-coupling efficiency η_c was found to be 0.9, the rest are either lost in the transmission or absorption in the cavity. At the same time, the small part of directly reflected light that did not enter the cavity and directly interferes with LO field only leads to a trivial offset which will be canceled by the 50:50 beam splitting ratio before the homodyne detector (BHD3). In the experiment, we lock our homodyne interferometer at $\Delta\phi = \pi/2$, and the optical cavity is locked such that the cavity is only slightly red-detuned with the laser. The membrane imprints a phase shift $\delta\phi_c$ on the reflected light and produces a homodyne voltage signal that takes the form of Eq. 4.57, with the help of the interferometer, the phase shift is converted into an intensity change detectable by the balanced homodyne detector and demodulated by our lock-in amplifier. Therefore, to obtain $X_m(t)$, we need to divide $D(t)$ from Eq. 4.57 by the useful homodyne contrast $\eta_c D_{\text{max}}$, we rewrite Eq. 4.56 as

$$X_m(t) = \frac{D(\Delta\phi = \pi/2)(t)}{D_{\text{max}}}\left(\frac{\kappa}{4g_0}\right)\left(\frac{1}{\sqrt{2}\eta_c}\right) \tag{4.58}$$

We can hence compute the number of phonon occupation (similar to Eq. 4.46) in the time domain:

$$\langle H(t)\rangle = \hbar\Omega_m\frac{\langle X_m(t)^2 + P_m(t)^2\rangle}{2}$$
$$= \hbar\Omega_m\left(\bar{n}_m(t) + \frac{1}{2}\right). \tag{4.59}$$

where we applied the equipartition theorem, $\langle X_m(t)^2\rangle_t = \langle P_m(t)^2\rangle_t$ and relate to the variance of the quadrature computed in time domain. As a minor remark, since the homodyne contrast D_{max} is measured using a oscilloscope with a high input imepedance, and the measured rms membrane signal using lock-in amplifier has to convert to amplitude variation, we require an overall $2\sqrt{2}$ combined correction factor. Finally, this yields

$$\bar{n}_m(t) + \frac{1}{2} = \langle X_m(t)^2\rangle_t$$
$$= \left(\frac{D(t)_{\text{rms}}^{50\Omega}}{\eta_c D_{\text{max}}}\right)^2\left(\frac{\kappa}{2g_0}\right)^2 \tag{4.60}$$

, where g_0 and κ are independently calibrated from the width of a PDH signal (see Fig. 2.13 in [59]) and optomechanical response to an amplitude modulation tone, respectively (see Sec. 4.6.3).

4.6 Characterization of mechanical oscillator

4.6.1 Cooling of the mechanical oscillator via dynamical backaction

Optomechanical damping via dynamical backaction plays an important role in cooling the room-temperature (298K) membrane from $\bar{n}_m \approx 3 \times 10^6$ phonons to an initial phonon occupation of 2×10^5 phonons with an intrinsic quality factor of $Q \sim 1.3 \times 10^6$. Even though optomechanical damping is not a prerequisite for the main work in Chapter 6, there are a few advantages to have a cooling beam. First, it allows a fast initialization of our membrane oscillator to a low temperature, which avoids saturation of the spin oscillator (as the spin can only hold up to approximately 10^7 phonons) when coupling the membrane to the atomic spins. At the same time, the lower temperature allows measurements to be performed with higher signal to noise ratio and hence fewer measurement repetitions are required to get a clear signal. To compute the cooling rates due to sympathetic cooling of the atoms, it is crucial to be able to estimate the phonon occupation of a membrane coupled to a thermal bath from optomechanical damping of the laser beams alone. For a membrane in thermal equilibrium with its environment, the mean occupation $\bar{n}_m$ at temperature $T_{m,\text{bath}}$ is given by the Bose-Einstein distribution, in the classical limit $k_b T_{m,\text{bath}} \gg \hbar \Omega_m$:

$$\bar{n}_{m,\text{bath}} \approx k_B T_{m,\text{bath}}/\hbar \Omega_m \tag{4.61}$$

To compute the temperature of a mechanical oscillator, we can compute the noise spectrum of the output field $\bar{S}_{PP,L}^{(\text{out})}(\omega)$ [59],

$$\begin{aligned}
\bar{S}_{PP,L}^{(\text{out})}(\omega) &= \bar{S}_{PP,L}^{(\text{in})}(\omega) + 4\Gamma_m \bar{S}_{XX,m}(\omega) \\
&= \frac{1}{2} + 8\Gamma_m \gamma_m |\chi_m(\omega)|^2 \left(\frac{1}{2} + \bar{n}_{\text{th}} + \frac{\Gamma_m}{\gamma_m} \right)
\end{aligned} \tag{4.62}$$

From the membrane displacement signal $X(t)$, one can perform Fourier transform to compute the power spectral density (PSD) of the membrane displacement $X_m(\omega)$. The area under the power spectral density (PSD) of the membrane displacement obeys is proportional to $\propto T_{m,\text{bath}}$. For a membrane coupled to a thermal bath in thermal equilibrium, assuming weak damping $\gamma_m \ll \Omega_m$, the phonon occupation of the membrane relates to the total damping rate by

$$\bar{n}_m = \bar{n}_{m,\text{bath}} \frac{\gamma_m}{\gamma_m + \sum_i \gamma_i} \tag{4.63}$$

where i sums over all the individual processes that leads to additional damping of the membrane, e.g. optomechanical damping from the cavity-locking beam and coupling beam.
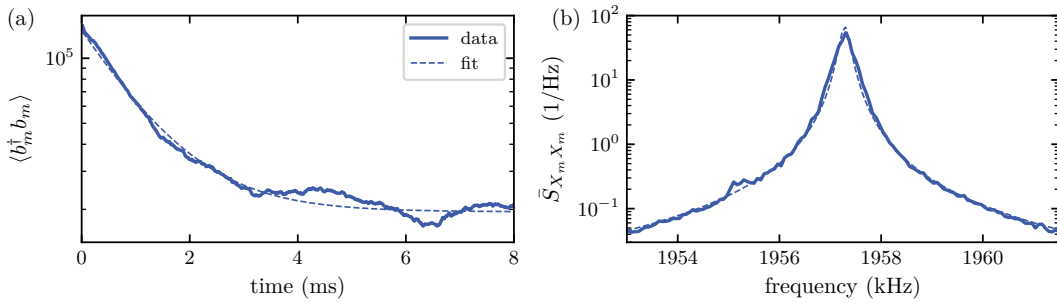
Figure 4.5: (a) Time trace of the membrane occupation number after turning on the coupling beam at $t = 0$ with only the red detuned cavity lock beam and almost on resonant (slightly red-detuned) coupling beam. (b) Power spectral density of the membrane displacement, the membrane is cooled simultaneously by the cavity-lock beam and the coupling beam.

As an example, we plot a ring down measurement of a membrane signal both in the time and frequency domain as shown in Fig. 4.5. shows the time-domain measurement of the mechanical oscillator in the absence of the spin. Before $t = 0$, the -5 MHz red detuned optomechanical damping beam is kept on to lock the cavity as well as provide an initial cooling to $\bar{n}_{m,\text{bath}} \approx 1.4 \times 10^5$ phonons and use as an independent detection of the membrane displacement. To mimic the actual experiment, at $t = 0$, the coupling beam is switched on. The coupling beam is set to be only slightly red-detuned to avoid dynamical backaction, the combined beams result in a lower membrane phonon occupation $\bar{n}_{m,\text{bath}} \approx 2 \times 10^4$ in the steady state. The initial phonon occupation compares to the final phonon obeys Eq. 4.63 very well, which matches the mechanical linewidth extracted from the fit of the spectrum. The mechanical linewidth is found to be broadened to $\gamma_m = 2\pi \times 262$ Hz.

4.6.2 Ringdown measurement of membrane

The intrinsic quality factor is an important figure of merit as it dictates the rate at which phonon enters from the environment. The quality factor of a mechanical oscillator can be easily determined by performing a ringdown measurement. Since we are interested in the intrinsic quality factor of the membrane oscillator, we position the mechanical oscillator to an intermediate finesse location such that there is enough laser power for cavity locking and while minimizing dynamical backaction effect due to the cavity lock beam. The intermediate coupling strength should allow one to determine the quality factor Q with decent signal to noise ratio. To measure the ring down of the membrane signal, a short resonant amplitude modulated in the cavity lock beam is sent to excite the membrane at $t = 0$, at the same time, the optomechanics beam used to detect the membrane displacement is switched on. The rms envelope of the membrane ring down sig-
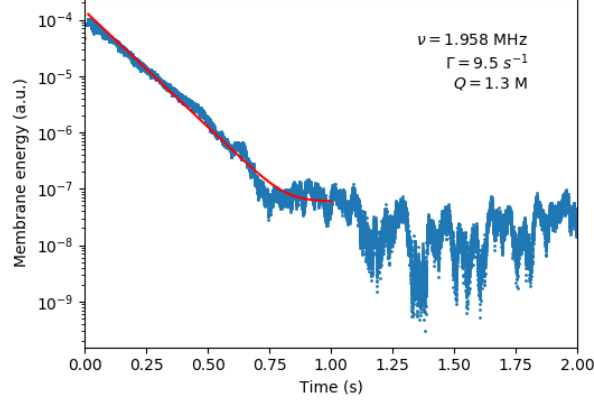
Figure 4.6: Measurement of the membrane ring down signal at low laser power, the blue data points are the rms envelope of the membrane ring down signal via homodyne detection and the red solid line is an exponential fit to the data.

nal $|Z| = \sqrt{I^2 + Q^2}$. is plotted in Fig. 4.6. The red solid line is a exponential time decay fit to the experimental data, the extracted quality factor was found to be $Q = 1.3 \times 10^6$ for the (2,2) mode at frequency of $\Omega_m = 2\pi \times 1.957$ MHz.

4.6.3 Characterization of membrane measurement rate

In this section, we present a calibration that relies on the measurement of the interference between an optomechanical response i.e. $P_L \propto X_m(t)$ to a classical amplitude modulation $X_L \propto A \cos(\Omega_m t + \phi)$ of a laser drive field. To perform this measurement, following Eq. 4.56 from Sec. 4.5.1, it is clear that one can detect an arbitrary superposition of the amplitude quadrature X_L and phase quadrature P_L of the output field, which encodes the classical drive and membrane signal, respectively. Here, by computing the power spectrum of the rotated light quadrature basis Eq. 4.56, the transfer function that describes such optomechanical response between the drive field can be obtained [59]:

$$|h_{X_a}(\omega)| = \left| 4\Gamma_m \chi_m(\omega) e^{2i\theta_c(\omega)} \sin(\Delta\phi) + \left[2(\eta_c - 1) + \eta_c \left(1 + e^{2i\theta_c(\omega)} \right) \right] \cos(\Delta\phi) \right| \tag{4.64}$$

where χ_m is the mechanical susceptibility and $\theta_c(\omega) = \arctan(2\omega/\kappa)$ is the phase angle, that accounts for the delay due to finite cavity response time $2/\kappa$. For this measurement, the membrane is placed at a high finesse position of the cavity, the optical cavity is locked such that the cooling beam is red-detuned ($\Delta_c \sim -5$ MHz) to provide initial cooling of the membrane and the coupling laser is slightly red-detuned to avoid instability due to the dynamical backaction. The homodyne phase of the loop interferometer is stabilized to a well-defined value with feedback
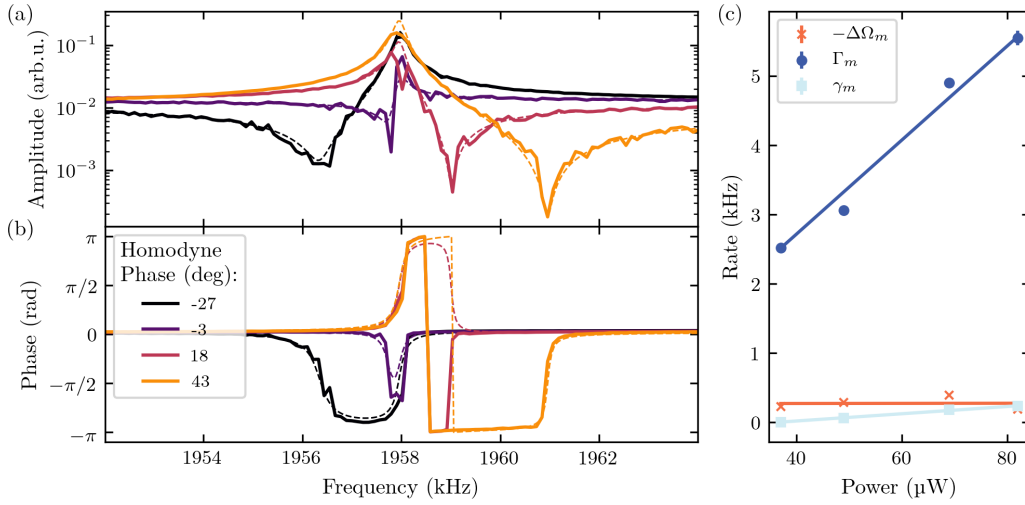
Figure 4.7: Measurement of the mechanical response to an amplitude modulation (a) Amplitude spectrum (b) Phase response. Each trace corresponds to a measurement with a different homodyne angle $\Delta\phi$. The solid line corresponds to the fit to the data using the transfer function Eq. 4.64. (c) The extracted rates are plotted as a function of input laser power. The solid lines are linear fits to the the individual rates.

control using a piezo mirror. Once the locks are set up, we can apply an amplitude modulation tone around the membrane frequency to the probe laser, and demodulate the detector signal using a lock in amplifier while sweeping the frequency of the drive. As shown in Fig. 4.7, we plot the measured optomechanical response in amplitude and phase as a function of drive frequency, respectively. Each trace in the plot corresponds to a different measurement with a chosen homodyne phase angle $\Delta\phi$. The homodyne phase angle $\Delta\phi$ is stabilized to a well-defined value using closed-loop feedback control on the piezo mirror in the local oscillator arm (see Fig. 4.3). To vary the homodyne phase angle, we can lock the piezo mirror at a different position. The experiment data shows the interference between the drive and the membrane responses across the membrane resonance at $2\pi \times 1.957$ MHz. The experimental traces are fitted with the model $|h_{X_a}|$ (see Eq. 4.64) globally with same the same fit parameters. From the fits (indicated by the solid lines), we obtain $g_0 = 2\pi \times 224$ Hz and $\kappa = 2\pi \times 65$ MHz which matches the independent calibration from PDH transmission fit (see Fig. 2.13 in [59]) . Moreover, in Fig. 4.7(b), we also study the membrane measurement rate Γ_m, damping rate γ_m and frequency shift $-\Delta\Omega_m$ as a function of laser power. As expected from theory, we see that a slight increase of membrane damping rate γ_m and the membrane measurement rate Γ_m increases linearly with laser power, and the optomechanical induced frequency shift is red detuned.

Chapter 5

Hybrid spin-optomechanics interface

This chapter introduces both the theoretical concepts and experimental implementations that should set the scene for understanding our main result, i.e. achieving the coherent feedback cooling of the membrane oscillator using atomic spins in the next chapter. The material presented here serves as a self-contained reference that intends to complement the main results. We first consider the coupled spin-membrane system using an abstract model and present the theoretical analysis of the coupled dynamics using the Heisenberg-Langevin equations. In the frequency domain, we may also derive a fit model that describes the spectra beyond the strong coupling including the sympathetic cooling regime. Lastly, we also present the Routh-Hurwitz criterion from control theory as a convenient means to access the stability of our coupled spin membrane systems.

On the experimental side, we introduce the experimental setup of our hybrid spin-optomechanics interface, then we revisit the spin noise cancellation and strong coupling experiment [14]. Finally, building on the strong coupling result, we show that we can manipulate the spin damping rate which makes the spin system a coherent feedback controller to cool the membrane oscillator as shown in the next chapter.

The result presented in this chapter has been published in [14] [66] and from the supporting materials of [14] [66] without major modifications. The content presented here is largely adapted from the manuscript, only minor modifications were made to the notations, formulas and references.

Theoretical description of the spin-membrane system

The spin-membrane coupling theory was described in a general framework of cascaded quantum systems that even includes multiple passes of light-matter interactions through the quantum system [30]. It is insightful to first forget the experiment complexity and to consider to first the spin and membrane interacting with a common traveling electromagnetic mode sequentially as sketched in Fig. 5.1. This allows one to engineer the light-mediated interaction without restricting ourselves to the experimental complexities. Specifically, we are interested

in the case where a traveling field a_L interacts with the spin first and then with the membrane and before interacting with the spin the second time in a looped geometry with the loop phase as a control knob (see Fig. 5.1). The cascaded interaction with the traveling quantum field a_L is given by [30]:

$$H_{\text{int}} = 2\hbar\sqrt{\Gamma_s}X_s\left[P_L\left(\zeta_1\right) + \cos(\phi)P_L\left(\zeta_3\right) - \sin(\phi)X_L\left(\zeta_3\right)\right] + 2\hbar\sqrt{\Gamma_m}X_mX_L\left(\zeta_2\right)$$

(5.1)

where $\zeta_1 < \zeta_2 < \zeta_3$ are the spatial coordinates along the optical path for the cascaded light-matter interactions.
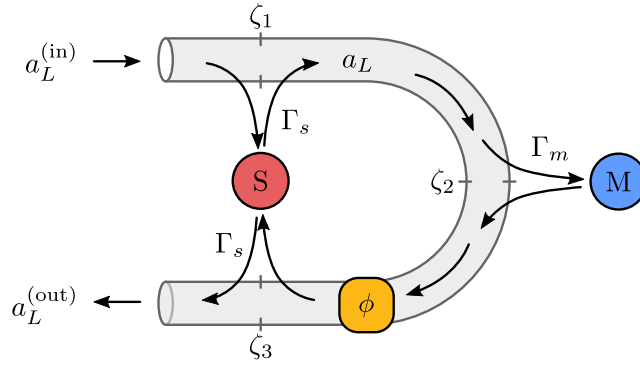
Figure 5.1: Schematic diagram of the coupling scheme. The optical field a_L first interacts with the spin (S) at spatial coordinate ζ_1, then to the membrane (M) at spatial coordinate ζ_2 before passing the spin (S) at the second time at ζ_3. Loop phase ϕ is set to π such that the light passes the spin system the second time would erase the information obtained from the first pass, therefore the backaction noise on the spin is suppressed. [Figure adapted from [30]]

It turns out that the cascaded light matter interactions can be brought to an effective interaction between the spin and membrane upon adiabatic elimination of the light field [30]. For pedagogical reasons, we can directly apply the final result, i.e. the master equations (derived in [14,30]) in the Lindblad form, where the coherent dynamics and the dissipative evolution can be interpreted separately (neglecting optical loss for simplicity) [30]:

$$\dot{\rho} = \frac{1}{i\hbar}\left[H_{\text{eff}}, \rho\right] + \mathcal{L}_{\text{eff}}\rho$$

(5.2)

where the effective Hamiltonian reads

$$H_{\text{eff}} = \hbar[1 - \cos(\phi)]gX_sX_m - \hbar\sin(\phi)2\Gamma_sX_s^2$$

(5.3)

where g $= 2\sqrt{\Gamma_s\Gamma_m}$ is the spin-membrane coupling strength. The collective dissipative part is captured by [30]:

$$\mathcal{L}_{\text{eff}}\rho = \mathcal{D}[J]\rho = J\rho J^\dagger - \frac{1}{2}\left(J^\dagger J\rho + \rho J^\dagger J\right)$$

(5.4)

where $J = J_m + J_s = \sqrt{2\Gamma_m}X_m + i\sqrt{2\Gamma_s}\left(1 + e^{i\phi}\right)X_s$ are the collective jump operators. Firstly, from the effective Hamiltonian, we can see that it involves a spin-membrane interaction but also a self-interaction of the spin. The latter can be exploited as an interaction for unconditional spin-squeezing (see Chapter 7). For $\phi = 0$, the interaction is dissipative. For this experiment, we are interested in the loop phase $\phi = \pi$ where we render an effective Hamiltonian interaction between the spin and membrane i.e. $H_{\text{eff}} = \hbar 2g X_s X_m$ and we also see that the dissipative part only affects the membrane, while the spin is decoupled from the input and output fields i.e. $J_s = 0$.

5.1 Heisenberg-Langevin equations

From the effective Hamiltonian Eq. 5.3, we can write down the Heisenberg-Langevin equations for the spin-membrane system as shown in Fig. 5.1 [30]. The equation of motion for the spin and membrane position and momentum operators read

$$\dot{X}_m = \Omega_m P_m, \tag{5.5}$$

$$\dot{P}_m = -\Omega_m X_m - \gamma_m P_m - 2g X_s(t-\tau) - \sqrt{4\Gamma_m}X_L^{(\text{in})}\left(\zeta_2\right) - \sqrt{2\gamma_m}F_m^{(\text{th})}, \tag{5.6}$$

$$\dot{X}_s = \Omega_s P_s, \tag{5.7}$$

$$\dot{P}_s = -\Omega_s X_s - \gamma_s P_s + 4\Gamma_s \sin(\phi)X_s(t-2\tau) + 2g\cos(\phi)X_m(t-\tau)$$
$$- \sqrt{4\Gamma_s}\left[P_L^{(\text{in})}\left(\zeta_1\right) + \cos(\phi)P_L^{(\text{in})}\left(\zeta_3\right) - \sin(\phi)X_L^{(\text{in})}\left(\zeta_3\right)\right] - \sqrt{2\gamma_s}F_s^{(\text{th})} \tag{5.8}$$

Here, $g = 2\sqrt{\Gamma_m \Gamma_s}$ is the spin-membrane coupling strength, τ is the optical propagation delay between the systems which we assume to be equal for either direction, and $\sqrt{2\gamma_m}F_m^{(\text{th})}$ and $\sqrt{2\gamma_s}F_s^{(\text{th})}$ are mechanical and spin thermal noise terms, respectively. Each oscillator is also driven by optical vacuum noise of the input field quadratures $X_L^{(\text{in})}(\zeta_i), P_L^{(\text{in})}(\zeta_i)$ at the different locations ζ_i along the optical path. This leads to quantum back-action of the light that mediates the spin-membrane interaction onto the coupled systems. For the spin oscillator, the optical input terms at the two locations ζ_1 and ζ_3 interfere as can be seen directly in Eqs.5.5-5.8. For the membrane there is no such interference as it interacts with the light field only once. Moreover, the two spin-light interactions also enable delayed light-mediated self-interaction of the spin. The effect of this is a modified frequency and linewidth since $X_s(t-2\tau) \approx X_s \cos(2\Omega_s\tau) - P_s \sin(2\Omega_s\tau)$. We thus have a spin frequency shift $\delta\Omega_s = 2\Gamma_s \sin(\phi)\cos(2\Omega_s\tau)$ and a shift of the damping rate $\delta\gamma_s = 4\Gamma_s \sin(\phi)\sin(2\Omega_s\tau)$. Since the atom-light coupling strength is inhomogeneous across the atomic ensemble, this can also lead to inhomogeneous broadening of the spin oscillator if $\phi \bmod \pi \neq 0$.

5.2 Fit function for the power spectral density of the coupled oscillators

The above coupled equations of motions can be readily solved in the frequency domain. By performing a first Fourier transform of the equations of motion Eqs. 5.5-5.8 on both sides. The effective susceptibilities read

$$\chi_{m,0}(\omega)^{-1}X_m(\omega) + 2g\,e^{i\omega\tau}X_s(\omega) = -\sqrt{2\gamma_m}F_m^{(\text{tot})}(\omega), \tag{5.9}$$

$$\chi_{s,0}(\omega)^{-1}X_s(\omega) + 2g\,e^{i\omega\tau}X_m(\omega) = -\sqrt{2\gamma_s}F_s^{(\text{tot})}(\omega), \tag{5.10}$$

where we have defined the individual oscillator susceptiblities as

$$\chi_{i,0}(\omega) = \frac{\Omega_i}{\Omega_i^2 - \omega^2 - i\omega\gamma_i}. \tag{5.11}$$

Solving for X_m and X_s yields

$$X_m(\omega) = \chi_{m,\text{eff}}(\omega)\big[-\sqrt{2\gamma_m}F_m^{(\text{tot})}(\omega) + 2g\,e^{i\omega\tau}\sqrt{2\gamma_s}\chi_{s,0}(\omega)F_s^{(\text{tot})}(\omega)\big],$$

$$X_s(\omega) = \chi_{s,\text{eff}}(\omega)\big[-\sqrt{2\gamma_s}F_s^{(\text{tot})}(\omega) + 2g\,e^{i\omega\tau}\sqrt{2\gamma_m}\chi_{m,0}(\omega)F_m^{(\text{tot})}(\omega)\big],$$

where we have introduced the effective susceptibilities of the membrane and spin oscillators as

$$\chi_{m,\text{eff}}(\omega)^{-1} = \chi_{m,0}(\omega)^{-1} - 4g^2 e^{i2\omega\tau}\chi_{s,0}(\omega), \tag{5.12}$$

$$\chi_{s,\text{eff}}(\omega)^{-1} = \chi_{s,0}(\omega)^{-1} - 4g^2 e^{i2\omega\tau}\chi_{m,0}(\omega). \tag{5.13}$$

We used this model to fit the power spectral densities of the mechanical displacement spectra [see Fig. 5.5A, C and Fig. 6.2(b)] globally using fit function $a^2|\chi_{m,\text{eff}}(\omega)|^2$ where a is a global scaling factor accounting for the noise terms driving the system. The argument of $\chi_{m,\text{eff}}$ returns the phase response plotted in Fig. 5.5B and D.

5.3 Derivation of the sympathetic cooling rate

Here, we also derive the sympathetic cooling rate (see Chapter. 6) which is relevant for the sympathetic cooling of the mechanical oscillator in the weakly coupling regime given in Eq. (6.3). For this, let us first write Eq. (5.12) explicitly

$$\chi_{m,\text{eff}}(\omega)^{-1} = \frac{1}{\Omega_m}\left(\Omega_m^2 - \omega^2 - i\omega\gamma_m - 4g^2 e^{i2\omega\tau}\frac{\Omega_m\Omega_s\left(\Omega_s^2 - \omega^2 + i\omega\gamma_s\right)}{\left(\Omega_s^2 - \omega^2\right)^2 + (\omega\gamma_s)^2}\right),$$

which can be written in the form of

$$\chi_{m,\text{eff}}(\omega)^{-1} = \frac{1}{\Omega_m}\left[\Omega_m^2 - \delta\Omega_{\text{shift}}^2 - \omega^2 - i\omega\left(\gamma_m + \gamma_{\text{sym}}\right)\right]. \tag{5.14}$$

Here, we have defined an effective frequency shift $\delta\Omega_{\text{shift}}$ and the sympathetic cooling rate γ_{sym}, which for $\omega = \Omega_m$ read

$$\delta\Omega_{\text{shift}}^2 = \frac{4g^2\Omega_m\Omega_s}{\left(\Omega_s^2 - \Omega_m^2\right)^2 + \left(\Omega_m\gamma_s\right)^2} \times \left[\left(\Omega_s^2 - \Omega_m^2\right)\cos\left(2\Omega_m\tau\right) - \Omega_m\gamma_s\sin\left(2\Omega_m\tau\right) \right],$$

and

$$\gamma_{\text{sym}} = \frac{4g^2\Omega_m\Omega_s}{\left(\Omega_s^2 - \Omega_m^2\right)^2 + \left(\Omega_m\gamma_s\right)^2} \times \left[\gamma_s\cos\left(2\Omega_m\tau\right) + \frac{\Omega_s^2 - \Omega_m^2}{\Omega_m}\sin\left(2\Omega_m\tau\right)\right].$$

For $\Omega_s \approx \Omega_m$ and large spin damping $\gamma_s > g$, we get a simplified expression for the frequency shift and sympathetic cooling rate [Eq. (6.3)]

$$\delta\Omega_{\text{shift}}^2 \approx \frac{4g^2\Omega_m}{4\delta^2 + \gamma_s^2}\left[2\delta\cos\left(2\Omega_m\tau\right) - \gamma_s\sin\left(2\Omega_m\tau\right)\right], \tag{5.15}$$

$$\gamma_{\text{sym}} \approx \frac{4g^2}{4\delta^2 + \gamma_s^2}\left[\gamma_s\cos\left(2\Omega_m\tau\right) + 2\delta\sin\left(2\Omega_m\tau\right)\right], \tag{5.16}$$

where $\delta = \Omega_s - \Omega_m$.

5.4 Routh-Hurwitz stability criterion of the coupled system

In this section we present a stability analysis in which the Routh-Hurwitz criterion [94] from control theory is applied to our linearly coupled spin-membrane oscillators. The criterion provides a convenient means to assess the stability of our linear systems without solving the equations of motion. In this treatment, we exclude the Langevin noise, as we are interested to see if the delayed coupled oscillator dynamics is stable by itself. We then explore the experimental parameter space to see under which conditions the coupled system becomes unstable. We take the equations of motion for the delayed coupled system Eqs. (6.1) and (6.2) neglecting the noise terms

$$\ddot{X}_m + \gamma_m\dot{X}_m + \Omega_m^2 X_m = -2g\Omega_m X_s(t - \tau), \tag{5.17}$$

$$\ddot{X}_s + \gamma_s\dot{X}_s + \Omega_s^2 X_s = -2g\Omega_s X_m(t - \tau). \tag{5.18}$$

Substituting the ansatz $X_j(t) = X_j(s)\,e^{st}$ where $s \in \mathbb{C}$ yields

$$\left(s^2 + s\gamma_m + \Omega_m^2\right)X_m(s) = -2g\Omega_m\,e^{-s\tau}X_s(s), \tag{5.19}$$

$$\left(s^2 + s\gamma_s + \Omega_s^2\right)X_s(s) = -2g\Omega_s\,e^{-s\tau}X_m(s). \tag{5.20}$$

Solving the simultaneous equations Eqs. (5.19) and (5.20), we obtain the characteristic equation for non-trivial solutions $X_m \neq 0$,

$$\left(s^2 + s\gamma_m + \Omega_m^2\right)\left(s^2 + s\gamma_s + \Omega_s^2\right) - 4g^2\Omega_m\Omega_s\,e^{-2s\tau} = 0. \tag{5.21}$$

For clarity, we consider here small propagation delays $\tau \ll 1/\Omega_j$ and apply a first order Taylor expansion $\exp(-2s\tau) \approx (1 - 2s\tau)$ (in the actual simulation we keep terms up to 4th order). We then obtain

$$
\begin{aligned}
0 =& s^4 + (\gamma_s + \gamma_m)s^3 + (\Omega_m^2 + \Omega_s^2 + \gamma_m\gamma_s)s^2 \\
&+ (\Omega_s^2\gamma_m + \Omega_m^2\gamma_s + 8g^2\Omega_m\Omega_s\tau)s \\
&+ \Omega_m\Omega_s(\Omega_m\Omega_s - 4g^2).
\end{aligned}
\tag{5.22}
$$

Having our dynamics in this polynomial form, we can define the polynomial coefficients of a fourth order polynomial by

$$
p(s) = a_4s^4 + a_3s^3 + a_2s^2 + a_1s + a_0 = 0, \ a_4 > 0.
\tag{5.23}
$$

In order to apply the Routh-Hurwitz criterion, the so-called Hurwitz matrix containing the polynomial coefficients has to be defined. For a fourth order polynomial this matrix reads

$$
H_4 = \begin{pmatrix} a_3 & a_1 & 0 & 0 \\ a_4 & a_2 & a_0 & 0 \\ 0 & a_3 & a_1 & 0 \\ 0 & a_4 & a_2 & a_0 \end{pmatrix}.
\tag{5.24}
$$

According to the Routh-Hurwitz criterion, the system dynamics is asymptotically stable if all the principal minors of the Hurwitz matrix are non-zero and positive. Application of the Hurwitz criterion leads to the following stability criteria for a fourth order polynomial system:

$$
\Delta_1 = |a_3| > 0,
\tag{5.25}
$$

$$
\Delta_2 = \begin{vmatrix} a_3 & a_1 \\ a_4 & a_2 \end{vmatrix} = a_2a_3 - a_4a_1 > 0,
\tag{5.26}
$$

$$
\Delta_3 = \begin{vmatrix} a_3 & a_1 & 0 \\ a_4 & a_2 & a_0 \\ 0 & a_3 & a_1 \end{vmatrix} = a_1\Delta_2 - a_3^2a_0 > 0,
\tag{5.27}
$$

$$
\Delta_4 = \det(H_4) = a_0 \cdot \Delta_3 > 0.
\tag{5.28}
$$

In our system, the coefficients are given explicitly by

$$
a_4 = 1,
\tag{5.29}
$$

$$
a_3 = \gamma_s + \gamma_m,
\tag{5.30}
$$

$$
a_2 = \Omega_s^2 + \Omega_m^2 + \gamma_s\gamma_m,
\tag{5.31}
$$

$$
a_1 = \gamma_m\Omega_s^2 + \gamma_s\Omega_m^2 + 8g^2\Omega_m\Omega_s\tau,
\tag{5.32}
$$

$$
a_0 = \Omega_s\Omega_m \left(\Omega_s\Omega_m - 4g^2 \right).
\tag{5.33}
$$

Since $\Omega_s\Omega_m \gg 4g^2$, all coefficients are positive. Thus, the criterion Δ_1 is fulfilled and the criterion Δ_4 depends directly on the criterion Δ_3. Therefore, only Δ_2 and

Δ_3 are left to be checked. In order to get an intuition on the stability for different parameters, Fig. 5.2 shows the stable regions as a function of spin damping, detuning and delay.
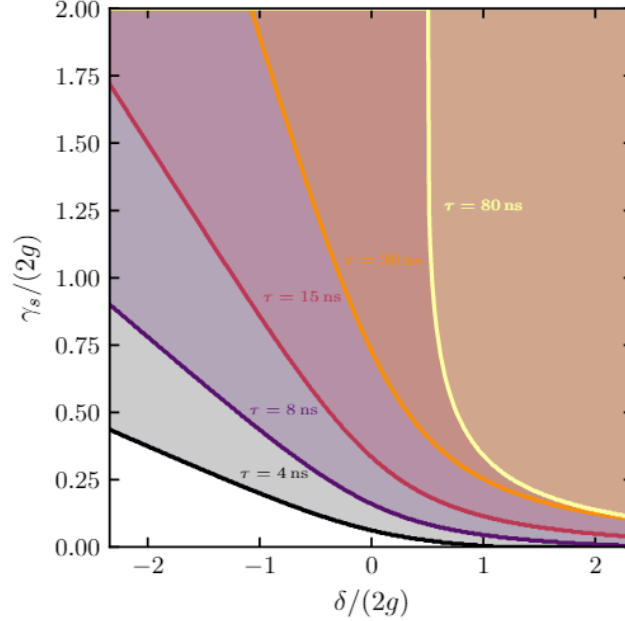
Figure 5.2: Evaluation of the stability of the coupled system using the Routh-Hurwitz criterion: The colored regions (i.e. region above each solid line) show the sets of parameters for which the coupled dynamics is stable for a given value of the feedback delay. Without propagation delay, every set of detunings and spin damping leads to stable dynamics. For $\tau = 80\,\mathrm{ns}$ we have $\Omega_m \tau \approx 1$ thus the validity of the Taylor expansion of the exponential function in presence of small delays reaches its limit. For the stability estimations shown here we used $2g = 2\pi \times 6.8\,\mathrm{kHz}$, $\gamma_m = 2\pi \times 262\,\mathrm{Hz}$, and $\Omega_m = 2\pi \times 1.957\,\mathrm{MHz}$. [Figure taken from [66]]

5.5 Overview of the coupling scheme

As we discussed in the first three chapters, we introduced the individual light-matter interfaces for the membrane and the spin. From the form of their individual light-matter Hamiltonian, the atomic spin is sensitive to the phase fluctuation of the light, whereas the membrane is sensitive to the amplitude fluctuation. This suggests that in order for the spin and membrane to interact with each other, the full coupling setup has to be able to convert the polarization dependent spin signal into an amplitude modulation that the membrane can see. Similarly, the membrane has to convert the amplitude modulation into a polarization modu-
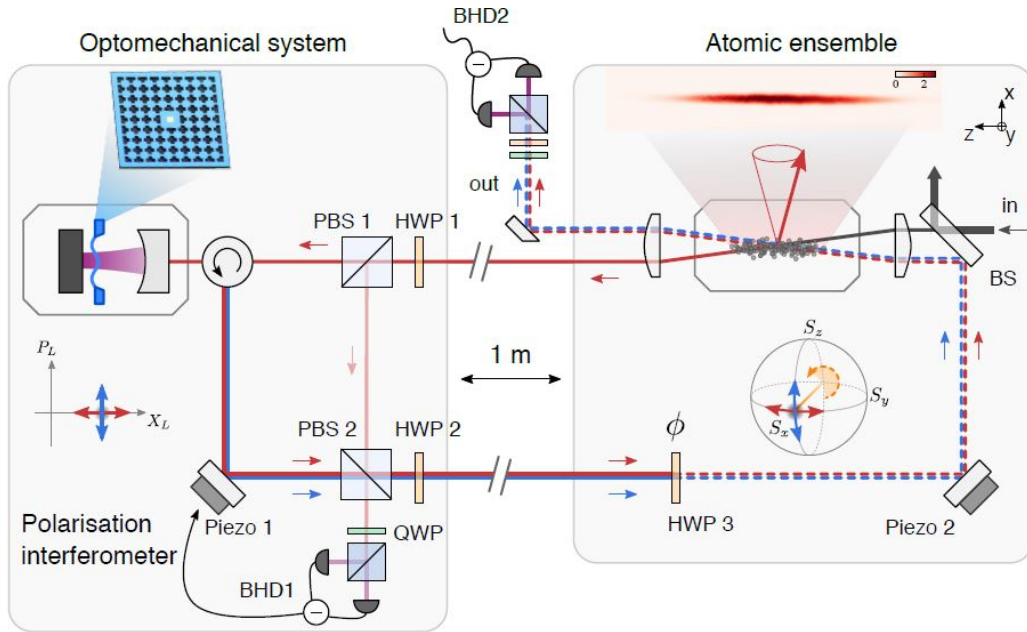
Figure 5.3: Simplified sketch of the experimental setup and the path of the light field used to mediate an effective interaction from the atomic spin ensemble to the membrane oscillator and back. A polarization interferometer maps between the Stokes vector at the atomic ensemble (shown on the Poincaré sphere) and the field quadratures of light (drawn as an optical phase space diagram). Light fields carrying spin signal are drawn as red lines, while light fields carrying membrane signals are blue. Before the light field returns to the atomic ensemble, a half-wave plate rotates the Stokes vector about the S_x axis and introduces a phase shift $\phi = \pi$ on the quantum fields in S_y, S_z which carry the spin and membrane signals, respectively. [Figure taken from [14]]

lation that the spin sees. Before we discuss the details of the coupling scheme, we discuss the overview of the coupling mechanism qualitatively below. As discussed in previous chapters, we see that the atomic spin couples to the circular polarization of light encoded in S_z and the membrane couples to the amplitude modulation encoded in S_y. In order for the two systems to interact with each other, we use the optical setup shown in Fig. 5.3 to convert between these two polarization states of light. We use a polarization interferometer, which consists of polarization dependent waveplates and beamsplitter to convert the amplitude modulation from the spin signal into a polarization modulation that couples to the spin. In order to mediate a bidirectional Hamiltonian, it is important that after the first interaction with the spin and then the membrane, the light interacts with the spin ensemble again. To manipulate the character of the light-mediated coupling, we can insert a half-waveplate HWP3 in the optical path returning to the spin. As we will discuss in more detail later, the waveplate allows one to add a phase

shift $\phi = 0$ or π to the quantum fields carrying the spin and membrane signals to access different coupling regime between the spin and membrane as discussed in Sec. 5.

5.6 Detailed description of the coupling scheme

Here, we describe in detail how we connect the two systems using light as a universal bus as shown in Fig. 5.3. This process involves several chains of signal transduction and it is convenient to designate the polarization of light by its stokes vector **S**. We consider our laser to be linearly polarized along x i.e. $\langle S_x \rangle = \bar{S}_0 = \Phi_L/2$, and we may write the x-polarized light as a strong coherent field and a quantum field in x polarization i.e. $a_x \approx \sqrt{\Phi_L} + b_L$ and the interesting field amplitudes (containing the membrane or the spin signals) are encoded in the y-polarized quantum field with notation $a_y = a_L$. The linearization of the stokes vector (dropping the second order terms) works well as long as $\langle a_L^\dagger a_L \rangle, \langle b_L^\dagger b_L \rangle \ll \Phi_L$,

$$S_0 = \frac{a_x^\dagger a_x + a_y^\dagger a_y}{2} \approx \bar{S}_0 + \sqrt{\frac{\bar{S}_0}{2}} \left(b_L + b_L^\dagger \right) \tag{5.34}$$

$$S_x = \frac{a_x^\dagger a_x - a_y^\dagger a_y}{2} \approx \bar{S}_0 + \sqrt{\frac{\bar{S}_0}{2}} \left(b_L + b_L^\dagger \right) \tag{5.35}$$

$$S_y = \frac{a_x^\dagger a_y + a_y^\dagger a_x}{2} \approx \sqrt{\frac{\bar{S}_0}{2}} \left(a_L + a_L^\dagger \right) \tag{5.36}$$

$$S_z = -i\frac{a_x^\dagger a_y - a_y^\dagger a_x}{2} \approx -i\sqrt{\frac{\bar{S}_0}{2}} \left(a_L - a_L^\dagger \right) \tag{5.37}$$

Here, we will describe the signal transduction of the light. First, the input light is linearly polarized along x such that $\langle S_x \rangle = \bar{S}_0 = \Phi_L/2$, subsequently the spin imprints its information onto the outgoing light via Faraday Hamiltonian.

$$H_{s,\text{int}} = 2\hbar\sqrt{\Gamma_s/\bar{S}_x}X_s S_z \approx 2\hbar\sqrt{\Gamma_s}X_s P_L \tag{5.38}$$

The spin imprints its transverse component $X_s \propto F_z$ as the polarization modulation of the light via the input-output relation.

$$S_y^{(\text{out})} = S_y^{(\text{in})} + 2\sqrt{\Gamma_s \bar{S}_0}X_s \tag{5.39}$$

At the input of the polarization interferometer, a half-waveplate is set to angle θ_H. This transforms the polarization as

$$S_x' = +\cos(4\theta_H)S_x + \sin(4\theta_H)S_y \tag{5.40}$$

$$S_y' = -\cos(4\theta_H)S_y + \sin(4\theta_H)S_x \tag{5.41}$$

$$S_z' = -S_z \tag{5.42}$$

This half-waveplate changes the ratio between the quantum signal (S_y) and local oscillator (S_x) that goes to the signal arm containing the optomechanical cavity and to the local oscillator arm, respectively. The photon flux in the arm containing the optomechanical cavity is given by

$$a_y'^\dagger a_y' = S_0 - S_x' = S_0 - \cos(4\theta_H) S_x - S_y \sin(4\theta_H) \tag{5.43}$$

Since the flux $a_y'^\dagger a_y'$ enters the optomechanical cavity, for a broad cavity linewidth, we may substitute $c^\dagger c = (4/\kappa) a_y'^\dagger a_y'$ by the input photon flux, we get

$$H_m = \hbar \frac{4g_0}{\kappa} \sqrt{2} X_m a_y'^\dagger a_y' \tag{5.44}$$

We may substitute Eq. 5.43, and linearize the stokes vector around the strong coherent amplitude (Eq. 5.34-5.37) yields

$$H_m = \hbar \frac{4g_0}{\kappa} \sqrt{\bar{S}_0} X_m \left[\left(b_L + b_L^\dagger \right) (1 - \cos(4\theta_H)) - \sin(4\theta_H) \left(a_L + a_L^\dagger \right) \right] \tag{5.45}$$

where the membrane Hamiltonian is now a weighted sum consisting terms a_L that contains the spin signal and a noise term due to the x polarized light that doesn't contain any spin signal but interacts with the membrane. To ensure good coupling of a_L to the membrane, the half-waveplate angle is set such that the classical part of the laser light, i.e. the x polarized light is reflected to the local oscillator arm and its quantum noise term b_L is suppressed to $1 - \cos(4\theta_H) = 0.1$, whereas most of the quantum field of y polarized light a_L is transmitted to the optomechanical cavity with $\sin(4\theta_H) = 0.5$, the backaction rate due to a_L over the total backaction rate due to a_L and b_L is still high i.e. $\sin(4\theta_H)^2 / [(1 - \cos(4\theta_H))^2 + \sin(4\theta_H)^2] \approx 0.93$. We recover the optomechanical interaction Hamiltonian $H_m \approx \hbar 2 \sqrt{\Gamma_m} X_m X_L$ with the membrane measurement rate given by $\Gamma_m = (4g_0/\kappa)^2 \Phi_m$ with an effective photon flux $\Phi_m = \Phi_L \sin(4\theta_H)^2 / 4$ at the optomechanical cavity. The membrane couples to the spin-induced amplitude modulation $2 \sin(4\theta_H) \sqrt{\Gamma_s \bar{S}_0} X_s$. The membrane responds to the changing radiation pressure and changes its position producing a phase shift $\phi_m = (4g_0/\kappa)\sqrt{2} X_m$ on the beam reflected from the cavity. We obtain a well defined homodyne phase by locking the relative phase between the local oscillator arm and the signal arm to the zero crossing of an error signal of a fringe lock with feedback piezo mirror 1 (see Fig. 5.3). The input stokes vector after the first HWP and is mapped onto the output stokes vector before the second HWP as

$$S_x'^{(\text{out})} = S_x'^{(\text{in})} \tag{5.46}$$

$$S_y'^{(\text{out})} = \cos(\phi_m) S_y'^{(\text{in})} + \sin(\phi_m) S_z'^{(\text{in})} \tag{5.47}$$

$$S_z'^{(\text{out})} = \cos(\phi_m) S_z'^{(\text{in})} - \sin(\phi_m) S_y'^{(\text{in})} \tag{5.48}$$

After the interferometer, the mean of the output stokes vector $\bar{S}$ is rotated back along S_x by setting HWP 2 to the same angle θ_H as HWP 1 (c.f. Eq. 5.40-5.42). For

$|\phi_m| \ll 1$, $\langle S_z'^{(\text{in})} \rangle = 0$ and $\langle S_y'^{(\text{in})} \rangle = \bar{S}_0 \sin(4\theta_H)$, the polarization modulation due to the membrane amounts to $S_z = 2\sqrt{\bar{S}_0 \Gamma_m} X_m$, which produces a mean torque that acts on the spin.

As shown in Fig. 5.3, the key control knob in our hybrid experiment is the loop phase which is currently realized by the insertion of a third half-waveplate HWP3 before the second atom-light interaction. For the hybrid experiments, the fast axis of the half-wave plate is aligned parallel to the laser polarization along x. This allows one to retard the orthogonal y-polarization by phase ϕ of 0 or π.

5.7 Strong coupling in the Hamiltonian regime

Upon establishing the basis of the spin-membrane coupling, we first present the result of spin noise suppression which is the key to realize Hamiltonian coupling in our hybrid experiment. Then, we will summarize the main results of the strong coupling between the atomic spin and the nanomechanical membrane mediated in a remote distance. As discussed in the previous section, we focus on the specific scenario, i.e. by adding a π optical phase on the light returning from membrane to atomic spins, which exhibits normal-mode splitting, coherent energy exchange oscillations as signature of strong Hamiltonian coupling. The result constitutes the basis for achieving coherent feedback cooling of the nanomechanical membrane oscillator we will discuss in the next chapter.

5.7.1 Spin noise suppression

The details of the spin noise suppression was presented in [14]. Here we provide a brief summary of the cancellation of spin signal in the output field which suppresses the quantum backaction on the spin. Since the spin information is prevented from leaking to the environment, the spin evades the quantum backaction. To perform this measurement, the optomechanical cavity is tuned off resonant to the laser such that there is no coupling of the spin to the membrane. Upon spin preparation, a short RF-pulse of 30 µs is sent to excite the spin to a small amplitude. Subsequently, the coupling beam is switched on to detect the Faraday rotation on the balanced homodyne detector (BHD 2 in Fig. 5.3). The waveplate is set up to detect the X_L quadrature which contains the Faraday signal. Fig. 5.4A shows the measured root-mean-squared spin signal in $X_L^{(\text{out})}$ for three different configurations. Two traces correspond to the double-pass atom-light interface with loop phases of $\phi = 0$ and $\phi = \pi$. The third trace shows the spin signal for a single pass interaction which is realized by moving the laser beam away from the atomic cloud in the second pass. The data clearly show a strong suppression of the spin signal for $\phi = \pi$ as compared to $\phi = 0$. Fitting the traces with an exponential decay including an initial detector rise time ($1/e$-time 10 µs) allows us to extract the amplitudes as well as the spin decay rates. First, we note that the double-pass signal for $\phi = 0$ is 3.3 times larger than the single-pass output, which indicates
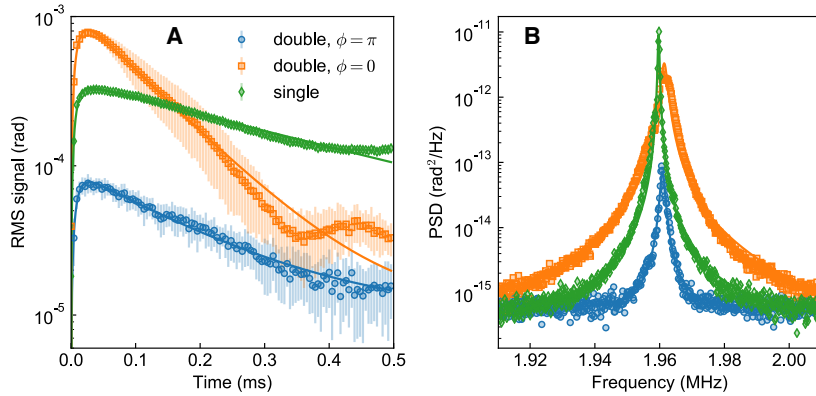
Figure 5.4: Destructive interference of the spin signal in the output field. (A) root-mean-squared spin signal as a function of time for the three configurations, double pass with $\phi = \pi$, $\phi = 0$, and single pass. Lines are fits with an exponential decay. (B) FFT power spectral densities for the same data as in (A). Lines are fits with a Lorentzian model. [Figure taken from [14]]

a 1.6-fold enhancement of the scattering efficiency in the presence of the second laser beam. Compared to $\phi = 0$, the spin signal at $\phi = \pi$ is suppressed by a factor 14. This value is in good agreement with $\epsilon(0)/\epsilon(\pi) \approx 12$ for $2\Omega_s \tau = 0.17$. In this measurement, optical delay is only due to optical path length of about 4 m because the cavity is off-resonant.

5.7.2 Normal-mode splitting

We first investigate the light-mediated coupling in the Hamiltonian regime ($\phi = \pi$) and with the spin realizing a positive-mass oscillator. At a magnetic field of $B_0 = 2.81$ G the spin is tuned into resonance with the membrane ($\Omega_s = \Omega_m$). In this configuration, the resonant terms in H_{eff} realize a beam-splitter interaction $H_{\text{BS}} = \hbar g(b_s^\dagger b_m + b_m^\dagger b_s)$, which generates state swaps between the two systems. Here $b_s = (X_s + iP_s)/\sqrt{2}$ and $b_m = (X_m + iP_m)/\sqrt{2}$ are annihilation operators of the spin and mechanical modes, respectively. We perform spectroscopy of the coupled system using independent drive and detection channels for spin and membrane. The membrane vibrations are recorded by balanced homodyne detection using an auxiliary laser beam coupled to the cavity in orthogonal polarization. To drive the membrane, this beam is amplitude modulated using an AOM. The spin precession is detected by splitting off a small portion of the coupling light on the path from spin to membrane. A radio-frequency (RF) magnetic coil drives the spin. We measure the amplitude and phase response of either system using a lock-in amplifier that demodulates the detector signal at the drive frequency see (Sec. 3.5.1 and Sec. 4.5.2). After spin-state initialization we simultaneously switch on coupling and drive and start recording. The drive fre-
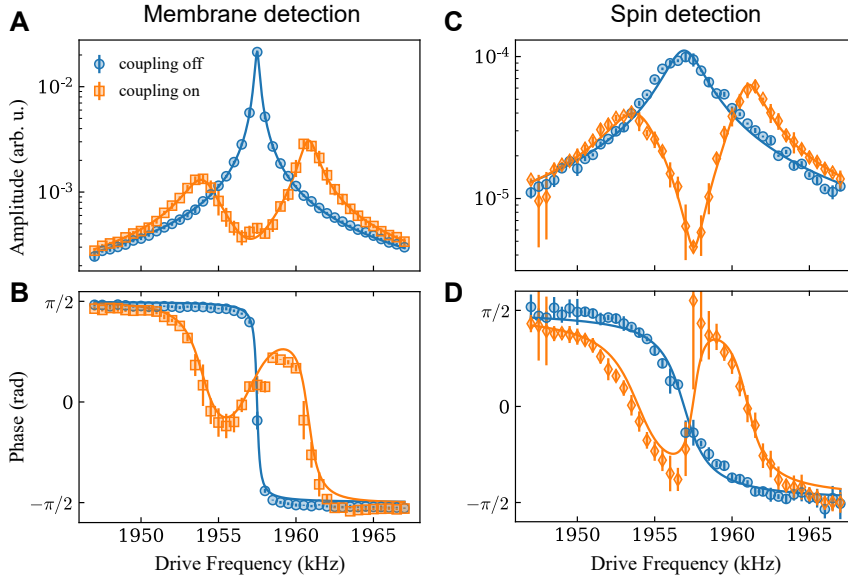
Figure 5.5: Observation of strong spin-membrane coupling. Spectroscopy of the membrane (**A,B**) and the spin (**C,D**), both revealing a normal mode splitting if the coupling beam is on and the oscillators are resonant ($\Omega_s = \Omega_m$). For comparison we show the uncoupled responses of the membrane with coupling beam off (**A,B**) and of the spin with cavity off-resonant (**C,D**). Lines are fits to the data with a coupled-mode model (see Sec. 5.2). Error bars are standard deviations of 3 independent measurements. [Figure taken from [14]]

quency is kept fixed during each experimental run and stepped between consecutive runs. Figs. 5.5A and B show the membrane's response in amplitude and phase, respectively. With the coupling beam off, it exhibits a Lorentzian resonance of linewidth $\gamma_m = 2\pi \times 0.3$ kHz, broader than the intrinsic linewidth due to optomechanical damping by the red-detuned cavity field [9]. For the uncoupled spin oscillator (Figs. 5.5C, D) with cavity off-resonant, we also measure a Lorentzian response of linewidth $\gamma_s = 2\pi \times 4$ kHz, broadened by the coupling light. When we turn on the coupling to the spin, the membrane resonance splits into two hybrid spin-mechanical normal modes. This signals strong coupling [95, 96], where light-mediated coupling dominates over local damping. Fitting the well-resolved splitting yields $2g = 2\pi \times 6.1$ kHz, which exceeds the average linewidth $(\gamma_s + \gamma_m)/2 = 2\pi \times 2$ kHz and agrees with the expectation based on an independent calibration of the systems (see Chapter 1-3). A characteristic feature of the long-distance coupling is a finite delay τ between the systems. It causes a linewidth asymmetry of the two normal modes when $\Omega_s = \Omega_m$, which we observe in Fig. 5.5. The fits yield a value of $\tau = 15$ ns, consistent with the propagation delay of the light between the systems and the cavity response time. We also observe normal-mode splitting in measurements of the spin (Figs. 5.5C

and D).

5.7.3 Energy exchange oscillations
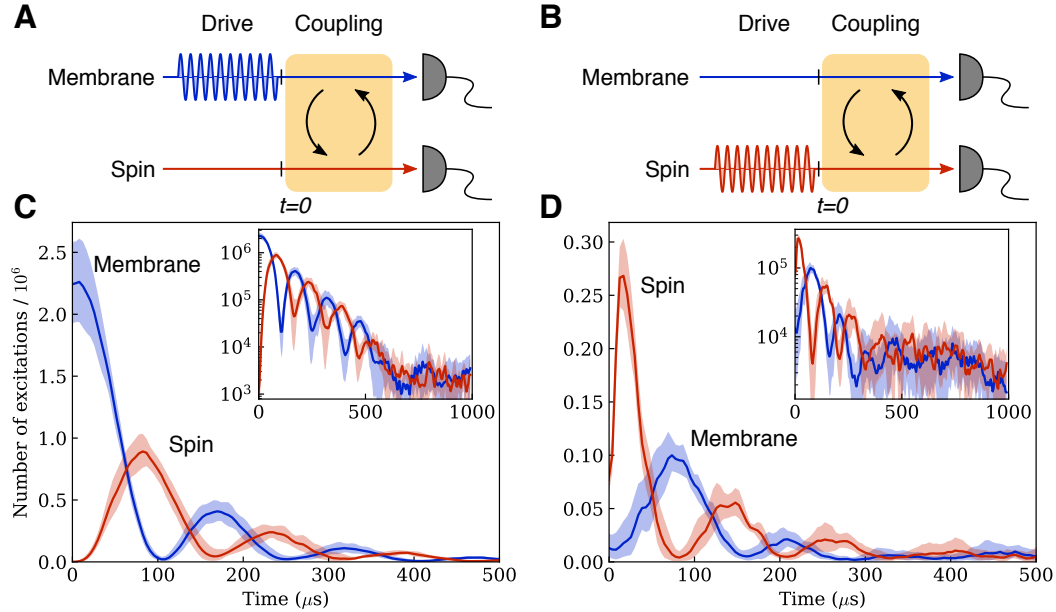
Figure 5.6: Time-domain exchange oscillations showing coherent energy transfer between spin and membrane (A) Pulse sequence for excitation of the membrane by radiation-pressure modulation via the auxiliary laser beam. (B) Pulse sequence for spin excitation with an external RF magnetic field. (C) Oscillations in the excitation numbers of membrane and spin as a function of the interaction time, measured using the pulse sequence in A. (D) Data obtained with pulse sequence B and weaker drive strength than in C. Here, the finite rise time of the spin signal at $t = 0$ corresponds to the turn-on of the coupling beam, which is also used for spin detection. Insets in C,D show the same data on a log-scale. Lines and shaded area represent the mean and one standard deviation of five measurements, respectively. [Figure taken from [14]]

Having observed the spectroscopic signature of the strong coupling, we now use it for swapping spin and mechanical excitations in a pulsed experiment. We start by coherently exciting the membrane to $\approx 2 \times 10^6$ phonons, a factor of 100 above its mean equilibrium energy, by applying an amplitude modulation pulse to the auxiliary cavity beam (Fig. 5.6A). At the same time, the spin is prepared in its ground state with $\Omega_s = \Omega_m$. The coupling beam is switched on at time $t = 0$ μs and the displacements $X_s(t)$ and $X_m(t)$ of spin and membrane are continuously monitored via the independent detection. From the measured mean square displacements we determine the excitation number of each system (see Sec. 4.5.2 and

Sec. 3.5.1). Fig. 5.6C shows the excitation numbers as a function of the interaction time. The data show coherent and reversible energy exchange oscillations from the membrane to the spin and back with an oscillation period of $T \approx 150$ μs, in accordance with the value π/g extracted from the observed normal-mode splitting. Damping limits the maximum energy transfer efficiency at time $T/2$ to about 40%. The same experiment is repeated but with the initial drive pulse applied to the spin (Figs. 5.6B and D). Here, we observe another set of exchange oscillations with the same periodicity, swapping an initial spin excitation of $n_s \approx 3 \times 10^5$ to the membrane and back. After the coherent dynamics have decayed, the systems equilibrate in a thermal state of $\approx 3 \times 10^3$ phonons, lower than the effective optomechanical bath of 1.5×10^4 phonons, demonstrating sympathetic cooling [13] of the membrane by the spin.

5.8 Calibration of the spin damping rate
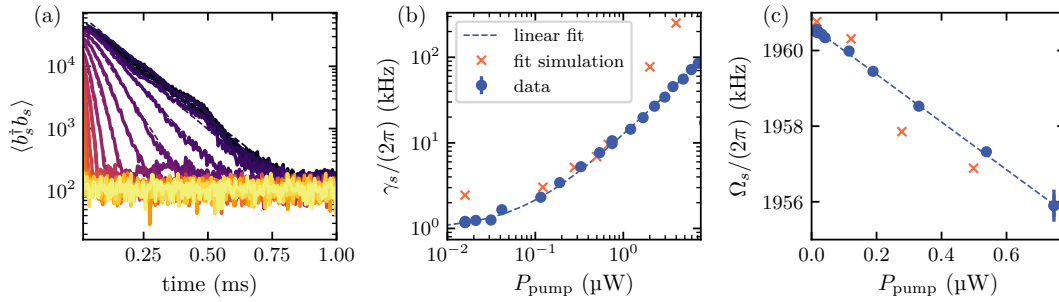
Figure 5.7: Measurement of the spin in the absence of coupling to the membrane after it is excited by a weak RF-pulse: (a) Time trace of double pass measurement of the spin with different pumping powers (range from 0 to $10\,\mu$W). The dashed lines show fits with an exponential decay. The spin linewidth (b) and spin frequency (c) are plotted as a function of the pump power. The dashed lines in (b) and (c) show a linear fit to the spin linewidth and resonance frequency. The crosses show the fit parameters extracted from Fig. 6.2(a) which were used as input for the simulations. The data shown in (a) is an average over seven experimental realisations and was used to fit the exponential decay [for (b)] and the Lorentzian peak [for (c)]. The error bars in (b) and (c) show the fit-error of the corresponding quantity. [Figure taken from [66]]

We end this chapter to demonstrate that we have flexible control over the spin damping rate γ_s which allows one the perform cool the membrane. In order to measure the spin damping rate in the presence of all lasers but without coupling to the membrane, we detuned the coupling laser from the cavity resonance ($|\Delta_c| \gg \kappa$). The laser thus is reflected from the incoupling mirror of the cavity and only

the spin is probed. For the calibration measurement of the spin damping rate, the spin was coherently excited by a weak RF-pulse. The spin signal was measured by detecting the residual spin signal on the light after the second pass via the spin. It is normalised to occupation numbers [shown in Fig. 5.7(a)]. Each experimental trace corresponds to a measurement with a different pump power. The damping rate γ_s is extracted from the exponential fit to the temporal dynamics [Fig. 5.7(b)] and the frequency Ω_s is extracted from a Lorentzian fit to the spectrum [Fig. 5.7(c)]. For optical pumping power larger than $P_{\text{pump}} > 0.7\,\mu\text{W}$, the spectra were too broad to provide reasonable fit results [and are therefore not shown in Fig. 5.7(c)]. In Fig. 5.7(b) and (c), fit parameters for the coupled dynamics are shown. We also observed a systematic shift of the Larmor frequency Ω_s with the spin pumping power, this is likely to be caused by undesired light shift when varying the spin pump power. To conclude, we can see that the we have flexible control over the spin linewidth by varying the spin pumping power P_{pump} in which paves the way to the main result present in the next chapter.

Chapter 6

Coherent feedback of a nanomechanical membrane with atomic spins

Coherent feedback stabilises a system towards a target state without the need of a measurement, thus avoiding the quantum backaction inherent to measurements. Here, we employ optical coherent feedback to remotely cool a nanomechanical membrane using atomic spins as a controller. Direct manipulation of the atoms allows us to tune from strong-coupling to an overdamped regime. Making use of the full coherent control offered by our system, we perform spin-membrane state swaps combined with stroboscopic spin pumping to cool the membrane in a room-temperature environment to $T = 216\,\text{mK}$ ($\bar{n}_m = 2.3 \times 10^3$ phonons) in $200\,\mu\text{s}$. We furthermore observe and study the effects of delayed feedback on the cooling performance. Starting from a cryogenically pre-cooled membrane, this method would enable cooling of the mechanical oscillator close to its quantum mechanical ground state and the preparation of nonclassical states. *The result presented in this chapter has been published in [66] and is included here without major modifications.*

6.1 Introduction

Hybrid quantum systems in which a mechanical oscillator is coupled to a spin are a promising platform for fundamental quantum science as well as for quantum sensing [10, 21, 97]. The interest in such systems derives from the fact that the spin – a genuinely quantum-mechanical object – can be used to control, read-out, and lend new functionality to the much more macroscopic mechanical device. Recently, different spin-mechanics interfaces have been realized, involving the coupling of a mechanical oscillator to (pseudo-)spin systems such as atomic ensembles [12–15, 22, 23], quantum dots [24, 25], superconducting qubits [19, 20, 26], or impurity spins in solids [11, 16–18], using light-, strain-, or magnetically-mediated interactions.

Coherent feedback is an intriguing concept that can be studied with such systems [60, 61]. In coherent feedback, a quantum system is controlled through its interaction with another one, in such a way that quantum coherence is preserved. In

contrast to measurement-based feedback [62], coherent feedback does not rely on measurements, thus avoiding the associated backaction and decoherence. Coherent feedback can under certain conditions outperform measurement-based feedback in tasks such as cooling of resonators [63, 64], and it has been implemented in solid state systems to enhance the coherence time of a qubit [98]. In optomechanical systems, it has been theoretically studied as a way to generate large nonlinearities at the single photon level [99, 100], to enhance optomechanical cooling and state transfer [101], as well as for entanglement generation [101–103].

In the context of spin-mechanics interfaces, the mechanical oscillator can act as the system to be controlled, i.e. the *plant*, which is coupled to a noisy thermal bath, and the spin system as the *controller*, coupled to a zero-temperature bath. Coherent feedback is achieved by coupling the two systems, thus reducing the noise in the mechanical system by transferring it to the spin, where it is dissipated. Additional coherent control of the spin enhances the cooling performance.

Hybrid systems combining atomic ensembles and mechanical oscillators have been used for sympathetic cooling by coupling the mechanical vibrations of a membrane to the center-of-mass oscillation of cold atoms in an optical lattice [13, 23]. In these systems the atomic motion was strongly damped and did not offer the possibility for coherent control. Furthermore, optical traps for atoms cannot reach MHz trapping frequencies without introducing substantial photon scattering and dissipation, restricting this cooling scheme to low-frequency mechanical oscillators. In contrast, collective spin states of atomic ensembles offer long coherence times and wide magnetic tuning of the spin precession frequency across the MHz range. Crucially, a versatile quantum toolbox exists that provides sophisticated techniques for ground-state cooling and quantum control [33, 40]. This makes it possible to use the atomic spin as a coherent feedback controller, which can be employed to efficiently cool and control the mechanical oscillator [104], e.g., via a state-swap [65].

Here, we demonstrate coherent feedback control of a nanomechanical membrane oscillator with the collective spin of an atomic ensemble and employ it to cool the membrane. For this, we exploit the coherent control offered by our recently demonstrated spin-membrane interface, where light mediates strong coupling between the two systems [14]. Using optical pumping on an internal atomic transition we can modify the spin damping rate and study the membrane cooling performance in different regimes. We show that coherent state swaps alternated with spin pumping pulses allow us to extract the noise from the mechanical system in an efficient way, providing the largest cooling rate and reaching the phonon steady-state faster than for continuous cooling. Finally, we study the effect of feedback delay onto the steady-state temperature of the membrane in the light-mediated coupling between the mechanical and spin systems. Our observations agree well with a theoretical model.
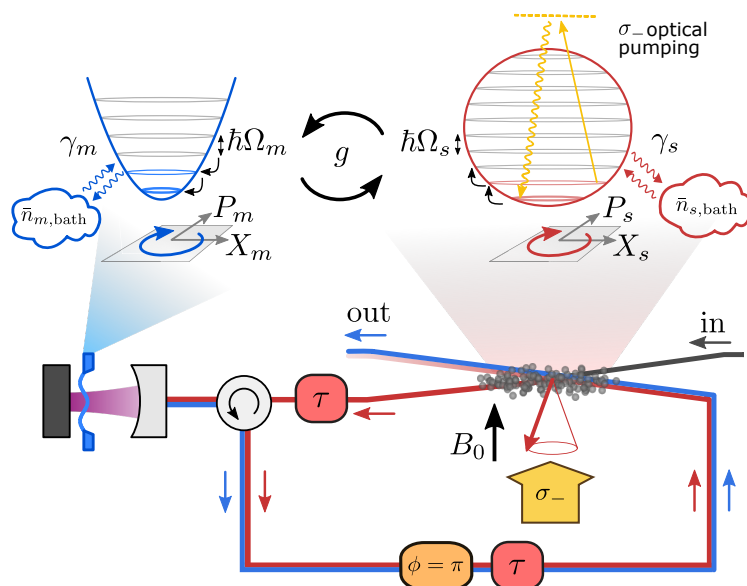
Figure 6.1: Sketch of the light-mediated spin-membrane coupling. Light interacts first with the spin, then with the membrane, and then again with the spin. The propagation of the light leads to a feedback delay τ. On the way back from the membrane to the spin, a π-phase is imprinted on the light, rendering the spin-membrane interaction effectively Hamiltonian for zero-delay $\tau = 0$. The systems can be approximated by harmonic oscillators of frequencies Ω_m and Ω_s with damping rates γ_m and γ_s coupling them to a bath with $\bar{n}_{m,\text{bath}}$ and $\bar{n}_{s,\text{bath}}$ phonons, respectively. The oscillators are coupled at a rate g. The spin damping rate can be increased by applying a σ_--polarized pumping laser.

6.2 Setup

Our hybrid system consists of a mechanical oscillator and a collective atomic spin coupled by laser light over a distance of 1 meter in a loop geometry (Fig. 6.1). The mechanical oscillator is the (2, 2) square drum mode of a silicon-nitride membrane [105], which has a vibrational frequency $\Omega_m = 2\pi \times 1.957\,\text{MHz}$ and an intrinsic quality factor $Q = 1.4 \times 10^6$. The membrane is placed in a single-sided optical cavity of linewidth $\kappa = 2\pi \times 77\,\text{MHz}$, which enhances the optomechanical coupling to external fields. The cavity is driven by an auxiliary laser beam (not shown in Fig. 6.1) that is red-detuned from the cavity resonance, providing some initial cavity optomechanical cooling of the membrane to 2×10^5 phonons [9]. The reflection of this beam is used to stabilize the cavity length and read out the membrane displacement via homodyne detection (detailed in Sec. 4.5.1).

The collective spin is realised with an ensemble of 1.3×10^7 cold ^{87}Rb atoms confined in an optical dipole trap. Strong coupling of the atomic ensemble to the
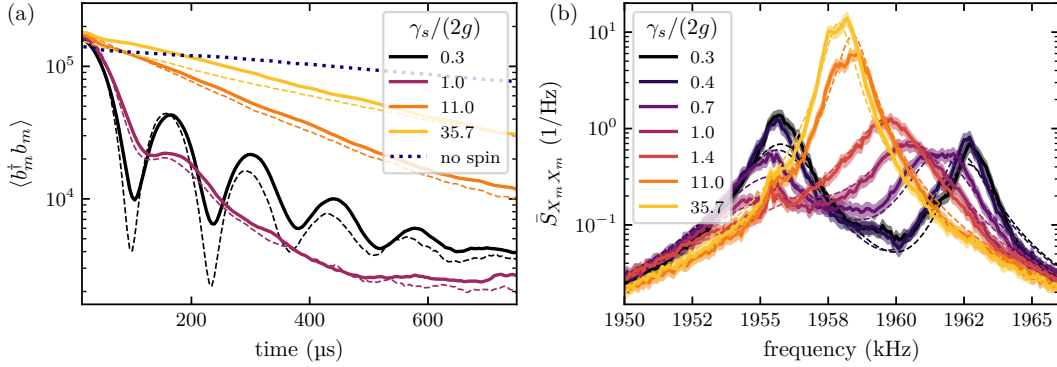
Figure 6.2: (a) Time traces of the membrane occupation number after turning on the coupling to the atoms. The different traces show measurements with different spin damping rates γ_s. The dashed lines correspond to the simulation described in the text based on Eqs. (6.1) and (6.2). The dotted line shows the membrane dynamics without atoms but with the coupling beam turned on. (b) Power spectral density of the membrane displacement. The dashed lines show a global fit to the data with the initial phonon occupation $\langle b_i^\dagger b_i \rangle(t = 0)$, Ω_m, τ, g, and the detector shot noise level as global fit parameters and Ω_s and γ_s as individual fit parameters. All other parameters were taken from independent calibrations. In (a) and (b), solid lines correspond to the mean and shaded areas to the standard deviation of 355 measurements.

light is ensured by its large optical depth $d_0 \approx 300$. The atomic spins are optically pumped into the hyperfine ground state $|F = 2, m_F = -2\rangle$ with respect to a static magnetic field $B_0 = 2.8\,\text{G}$ perpendicular to the propagation direction of the coupling laser. The Larmor frequency $\Omega_s \propto B_0$ is tuned into resonance with the membrane frequency Ω_m. The spin precession is measured after the first interaction with the coupling laser by picking up a small fraction of the light (calibration shown in Sec. 3.5.1). The small-amplitude dynamics of the transverse spin components can be described by a harmonic oscillator of frequency Ω_s using the Holstein-Primakoff approximation [33].

A coupling laser beam interacts first with the spin, then with the membrane, and once again with the spin, as sketched in Fig. 6.1 and detailed in [14]. The coupling beam with $1\,\text{mW}$ optical power is slightly red-detuned with respect to the membrane cavity and $-2\pi \times 40\,\text{GHz}$ red-detuned from the ^{87}Rb D$_2$-line. It cools the membrane further to $\bar{n}_{m,\text{bath}} = 2.0 \times 10^4$ phonons, which broadens its linewidth to $\gamma_m = 2\pi \times 262\,\text{Hz}$. In presence of the coupling beam, the spin linewidth is $\gamma_s = 2\pi \times 2.2\,\text{kHz}$. In the first spin-light interaction, the X_s quadrature of the atomic spin is imprinted onto the coupling beam via the Faraday interaction [33], resulting in a modulation of the radiation-pressure force on the membrane. Likewise, the membrane displacement X_m modulates the light reflected from the cavity [9] which then creates a torque on the spin in the second interaction. On the

way back from the membrane to the spin, the optical field carrying the spin and membrane signals is phase-shifted by π such that the effective spin-membrane interaction is predominantly Hamiltonian and the backaction of the light on the spin is suppressed [30]. Tracing out the light field and neglecting the propagation delay for the moment, the resonant part of the effective spin-membrane interaction is described by a beam splitter Hamiltonian $H_{\text{BS}} = \hbar g(b_s^\dagger b_m + b_m^\dagger b_s)$, where b_m (b_s) is the annihilation operator of a membrane (spin) excitation and g is the effective spin-membrane coupling rate [14].

6.3 Continuous Cooling

Recently, we demonstrated strong coupling with this spin-membrane interface, i.e. $2g > (\gamma_s + \gamma_m) \approx \gamma_s$ [14]. Strong coupling is manifested by the hybridization of the membrane and spin modes which leads to a normal mode splitting of $2g = 2\pi \times 6.8\,\text{kHz}$ in the spectrum as shown in Fig. 6.2(b). In the time domain, strong coupling gives rise to state swaps between the spin and the membrane at the coupling rate g. In Fig. 6.2(a) we show the time evolution of the membrane occupation number after switching on the coupling beam. For $2g > \gamma_s$, the thermally excited membrane swaps its state with the spin, which is initially prepared close to its ground-state, in half a period $T_\text{ß} = \pi/g$ of the energy exchange oscillations. After another half period, the thermal state is swapped back onto the membrane but the phonon number is reduced due to the damping that occurred in the spin system, whose linewidth is larger than that of the membrane. The oscillations dephase after approximately 1 ms and a steady state with a membrane occupation of $\bar{n}_{m,\text{ss}} \approx 2.3 \times 10^3$ phonons is reached, corresponding to a temperature decrease by two orders of magnitude compared to the initial state. In this process the membrane is predominantly cooled via its coupling to the cold and damped spin, reaching a temperature one order of magnitude lower than in the presence of the optomechanical cooling beams alone.

We now study the effect of increasing the spin damping rate γ_s on the coupled dynamics. To increase γ_s we apply a σ_--polarized pump laser along the polarization axis of the spin (calibration in Sec. 5.8). As can be seen in Fig. 6.2(a), increasing γ_s first enhances the membrane cooling, until the overdamped regime $\gamma_s \gg 2g$ is reached where the membrane couples incoherently to a quasi-continuum of cold spin fluctuations. The membrane decay is then governed by Fermi's golden rule, with the occupation number decreasing at the sympathetic cooling rate $\gamma_{\text{sym}} \approx 4g^2/\gamma_s$, i.e. the cooling becomes less effective as γ_s is increased further. In this weak-coupling regime, the modes decouple and the membrane spectrum shows a single Lorentzian peak, broadened by the interaction with the spin, see Fig. 6.2(b).
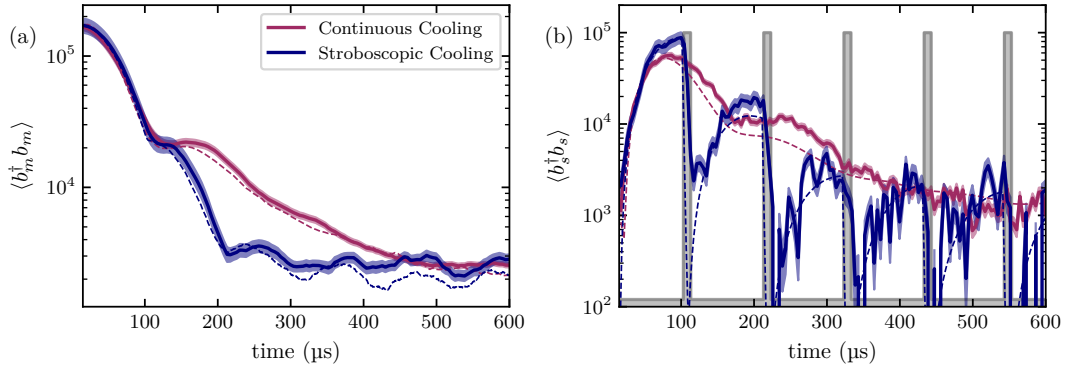
Figure 6.3: (a) Membrane and (b) spin occupation numbers for continuous cooling at $\gamma_s = 2g$ and stroboscopic cooling at $\gamma_s = 0.6g$. The gray shaded areas indicate the spin pumping pulses (where $\gamma_s \approx 60g$). Solid lines and shaded areas correspond to the mean and standard deviation of 70 measurements and dashed lines correspond to a simulation.

6.4 Stroboscopic Cooling

Previous experiments, which coupled a membrane to the motion of cold atoms [13, 23], lacked both strong coupling and coherent control over the atoms. In contrast, our strongly coupled spin-membrane system allows us to implement more elaborate coherent control schemes. In particular, we can combine strong coupling and strong spin damping in a stroboscopic fashion in order to cool the membrane much faster than in the continuous cooling case discussed above. In Fig. 6.3 we show a comparison between stroboscopic and continuous cooling, where time traces for (a) the membrane occupation number and (b) the spin occupation number are shown. In the stroboscopic sequence we perform a coherent π-pulse ($T_{\text{pulse}} = 100\,\mu s$, $\gamma_s = 0.6g$) to swap membrane and spin states. Afterwards, we apply an optical pumping pulse of duration $T_{\text{pump}} = 10\,\mu s$ which increases the spin damping rate to $\gamma_s \approx 60g$ and depletes the spin occupation on a timescale much shorter than the state swap (gray pulses in Fig. 6.3(b)). During the pumping pulse the coupling is kept on. Since the spin is reinitialised close to the ground state, the next coherent state swap does not transfer thermal energy back to the membrane but only cools it further. It takes two to three such iterations of a coherent π-pulse followed by a spin pumping pulse to reach the steady state (see Fig. 6.3). Using this simple sequence, we can reach the membrane steady state temperature of 216 mK ($\bar{n}_{m,\text{ss}} = 2.3 \times 10^3$ phonons) in around 200 µs, approximately a factor of two faster than for continuous cooling. This exemplarily shows the advantage of a coherent feedback controller, which enables faster cooling than if the membrane is coupled with a similar rate to an incoherent, overdamped system.
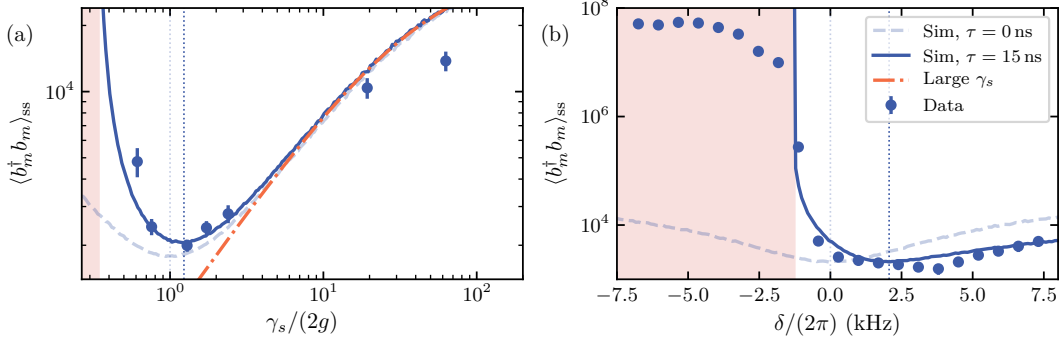
Figure 6.4: Steady state occupation of the membrane as a function of (a) spin damping rate γ_s (at resonance, $\delta = 0$) and (b) spin-membrane detuning $\delta = \Omega_s - \Omega_m$ at $\gamma_s = 0.6g$. The solid (dashed) blue line shows the result of the simulation with (without) delay. In (a), the red dashed-dotted line indicates the steady-state number given by the rate in Eq. (6.3) with $\tau = 15$ ns. The red shaded area shows the region for which the dynamics is found to be unstable using the Routh-Hurwitz criterion. For this measurement, $\bar{n}_{m,\text{bath}} \approx 4.0 \times 10^4$ phonons and $\gamma_m = 2\pi \times 94$ Hz (independently calibrated without atoms). The data points with error bars correspond to the mean and the standard deviation of steady state occupations of 20 (3) experimental realisations in (a) ((b)).

6.5   Theoretical Model

Further insight into the dynamics is gained by solving the equations of motion for the coupled spin-membrane system [14],

$$\ddot{X}_m + \gamma_m \dot{X}_m + \Omega_m^2 X_m = -2g\Omega_m X_s(t - \tau) + \mathcal{F}_m, \quad (6.1)$$

$$\ddot{X}_s + \gamma_s \dot{X}_s + \Omega_s^2 X_s = -2g\Omega_s X_m(t - \tau) + \mathcal{F}_s, \quad (6.2)$$

where terms on the left-hand-side describe the internal dynamics of the damped oscillators and the first term on the right-hand-side describes the state swap dynamics including a propagation delay τ between the spin and the membrane. We included the generalized Langevin forces $\mathcal{F}_m$ and $\mathcal{F}_s$ that capture stochastic force terms due to quantum fluctuations, thermal and measurement backaction noise (detailed in Appendix. A).

We used the following procedures to simulate our experimental results: for the continuous cooling measurements, we first fitted the spectra for different γ_s in Fig. 6.2(b) globally using a coupled-mode model (fit function given in Sec. 5.2). From this fit, the extracted τ and Ω_m were used as the input parameters for the simulation. We adapted the technique described in [106] to numerically solve the equations of motion (6.1) and (6.2) and compare the solution to our data (more details are given in Appendix. A). To generate each time trace in Fig. 6.2(a) (dashed lines) we fitted the numerical solution to our data with only γ_s and Ω_s as free

111

parameters. The fit results show a systematic shift of Ω_s with increasing spin pumping power, likely due to the light shift induced by the circularly polarised pumping laser (Fig. 5.7), and γ_s was observed to be larger than in the independent calibration of Sec. 5.8.

For the stroboscopic cooling measurements, we took the fit parameters from the continuous cooling measurement and ran the simulation with a time dependent spin damping rate which was taken to be $\gamma_s = 0.6g$ during the state swaps and $\gamma_s = 60g$ during the pumping pulses. The fit is shown for membrane and spin in Fig. 6.3 as a dashed line. The good agreement between fit and data shows that our model includes all the relevant factors which govern the coupled dynamics.

6.6 Delayed Feedback

Our hybrid spin-membrane system constitutes a coherent feedback network [64], in which delayed feedback can give rise to instabilities [58, 107, 108]. In our experiment, such instabilities show up as a spontaneous coupled oscillation of spin and membrane, which we observe for certain values of the spin-membrane detuning $\delta = \Omega_s - \Omega_m$. Even at resonance, we have to include the feedback delay to predict the experimentally measured steady state occupation of the membrane accurately. In Fig. 6.4 we plot the measured and simulated occupation numbers of the membrane in steady state as a function of γ_s [Fig. 6.4(a)] and δ [Fig. 6.4(b)]. At resonance and for $\Omega_m \tau \ll 1$ (as in our system), the effect of the feedback delay is most apparent in the limit of small γ_s. The model without delay (light-blue dashed line) predicts a significantly smaller occupation number compared to both what we observe in experiments and what is predicted by our model including the feedback delay (blue solid line). In the large γ_s limit, the sympathetic cooling rate is modified to

$$\gamma_{\text{sym}} \approx \frac{4g^2}{4\delta^2 + \gamma_s^2} \left[\gamma_s \cos(2\Omega_m \tau) + 2\delta \sin(2\Omega_m \tau) \right] \tag{6.3}$$

(see Sec. 5.3 for derivation). In this limit, the steady state occupation is given asymptotically by $\langle b_m^\dagger b_m \rangle_{\text{ss}} = \bar{n}_{m,\text{bath}} \gamma_m / (\gamma_m + \gamma_{\text{sym}})$, shown as the red dashed-dotted line in Fig. 6.4(a). The theory of coupled oscillators without delay predicts optimal sympathetic cooling at the critical damping of $\gamma_s = 2g$ (faded vertical dotted line in Fig. 6.4). Including the feedback delay in the model, the minimal occupation number shifts to larger γ_s (dark vertical dotted line), because the self-oscillations have to be compensated by a higher spin damping rate. The experimental data confirms this theoretical prediction.

Furthermore, we find that the presence of delay lifts the symmetry in δ, as inferred theoretically from Eq. (6.3) for large γ_s and shown both experimentally and theoretically in Fig. 6.4(b) for small $\gamma_s = 0.6g$. We see that the minimal steady state occupation of the membrane is obtained for positive detuning δ, i.e. $\Omega_s > \Omega_m$,
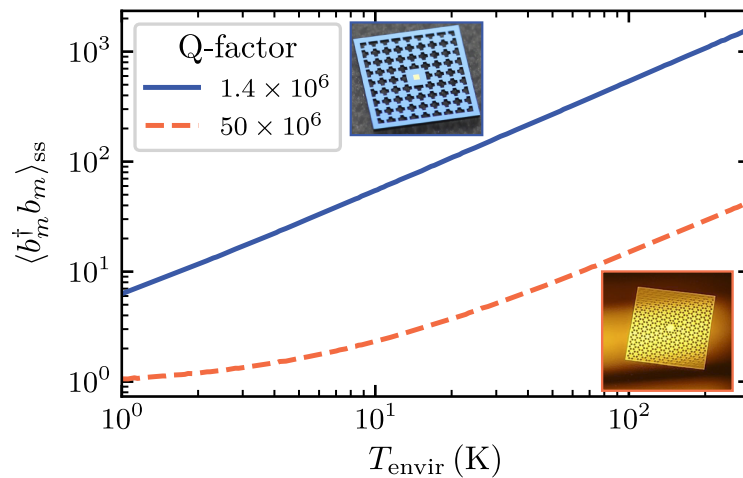
Figure 6.5: Simulated steady state occupation of membranes for varying cryostat temperature and different mechanical Q factors. Here, $\gamma_s = 2g$, $\delta = 0$ and $\tau = 15\,\text{ns}$. The insets show the current membrane with phononic shield used in these experiments and a soft-clamped membrane for which $Q \approx 5 \times 10^7$.

which is true in general for a feedback system with a delay of $\tau < \pi/(2\Omega_m)$. For large enough negative δ, we observe that the coupling drives the system into limit cycle oscillations, see Fig. 6.4(b). With our model we can attribute these self-oscillations to the feedback delay. In this self-driven regime, the resulting membrane occupation of 6.8×10^7 exceeds the spin length by around a factor of three. The emergence of such instabilities can be characterised using the Routh-Hurwitz stability criterion [94], which indicates whether the real part of one of the normal modes of the system reverses its sign (shown in Sec. 5.4). In Fig. 6.4 we indicate such unstable regions for our coupled system by a shaded area. Our calculations show that the precise value of δ at which the driving due to the loop delay exceeds the damping of the coupled system depends on γ_s. Even at resonance [Fig. 6.4(a)] self-oscillations are predicted for small enough γ_s.

The propagation delay is an interesting tuning knob for coherent feedback experiments, which gives access to Hamiltonian and dissipative dynamics: We can induce self-oscillations of the system, tune the dependence of the steady state on system parameters such as damping rate and detuning, or even render the delay negligible by tuning $2\Omega_m\tau$ to a multiple of 2π.

6.7 Discussion

In our experiment, the cooling rate of the membrane due to its coupling to the spin exceeds the cavity-optomechanical cooling rate by more than one order of magnitude. The lowest achievable phonon occupation of the membrane is thus

given by the competition of cooling the membrane with the spin and heating due to its coupling to the room-temperature environment. In Fig. 6.5 we show the expected membrane steady state occupation for varying environment temperature and two different membrane designs. In this calculation we include the cavity-optomechanical cooling of the membrane (which has a negligible effect), the light-mediated coupling to the spin including backaction of the light, as well as thermal and quantum mechanical ground state fluctuations of both systems. The higher quality factors $Q > 5 \times 10^7$ of soft-clamped membranes [48, 109] would reduce the thermal decoherence rate by a factor 25 and allow us to prepare the mechanical oscillator close to its ground state in a 4 K environment. These technical improvements would realize a mechanical oscillator whose phonon occupation is limited by quantum backaction instead of thermal noise. While in the current coupling scheme the double pass eliminates backaction on the atomic spin, a large membrane quantum cooperativity $C_m > 1$ would favor a double pass scheme with coherent cancellation of quantum backaction on the membrane. This would lead to a higher quantum cooperativity for the spin-membrane coupling [30]. Further, the feedback control of the membrane could be improved by increasing the quantum cooperativity of the spin system. This involves gaining a better understanding of the spin decoherence sources and achieving a larger spin-light coupling rate.

In this work we implemented a relatively simple coherent feedback sequence based on coherent state swaps of pulse area π interleaved with short spin pumping pulses. In the future, it would be interesting to explore more elaborate feedback sequences to optimize the cooling in a specific situation. For example, the duty cycle of the stroboscopic cooling sequence could be changed over time to cool a mechanical oscillator with a high initial occupation that exceeds the spin length. Initially, short coupling pulses of pulse area $\ll \pi$ could remove excitations without saturating the spin, and once the phonon number is sufficiently reduced, the pulse area could be increased to minimize the final temperature.

Our coherent feedback cooling scheme is a rather general technique that can be applied to any physical system with a strong light-matter interface. This includes cavity optomechanical systems or mechanical oscillators without an optical cavity. Moreover, similar cooling schemes could be implemented in the microwave domain with electromechanical oscillators [26] coupled to solid-state spin systems. The macroscopic distance between the feedback controller and the target system enables modular control schemes in analogy to classical feedback in electrical engineering. This opens up the new possibility to use coherent feedback control in quantum networks.

The coherent control and bidirectional Hamiltonian coupling employed in this work pave the way towards more elaborate quantum protocols such as the generation of non-classical mechanical states via state swaps [65] as well as further studies of coherent feedback in the quantum regime [60–63].

Chapter 7

Conclusion and Outlook

In this thesis, we reported on the demonstration of coherent feedback cooling of a nanomechanical membrane using atomic spins [66]. The coherent feedback builds on and exploits the strong, bidirectional Hamiltonian coupling between the two systems [14, 30, 59]. We were able to access different cooling regimes with the control on the spin damping rate and developed a more efficient cooling strategies using the concept of coherent feedback.

In Chapter 6, we showed that we can exploit the spin-membrane state swaps and combine with the coherent control pulsed pumping on the spin to achieve more efficient cooling [64, 66] than the overdamped cooling regime. Nevertheless, our result only constitutes an example of an experimental implementation in the vast field of quantum coherent feedback [61, 62, 64]. Specifically, the discussion of the role of propagation delay in our main result (see Sec. 6.6 in Chapter 6) hinted to a more rigorous experimental study of the double pass via the individual spin membrane light-matter interface. We can send laser light twice through the spin or membrane and study the effect of varying length of the optical fiber or the loop phase between the two passes. For example, we can send light on the spin twice to study the effect of dynamical backaction in analogy to cavity optomechanics using the retarded nature of the feedback force. Moreover, such double pass scheme also allows the study of one-axis twisting Hamiltonian $H_{s,\text{int}} = \hbar 2\Gamma_s X_s^2$ [30, 110], which is an important ingredient to generate spin-squeezed state and entanglement for quantum metrology [40].

Another important goal of our experiment is to achieve quantum coherent coupling between the spin and membrane, which is a stronger condition than strong coupling [96]. The coupling strength g must exceeds the thermal decoherence rates of both systems. To achieve this, the individual spin/membrane interface need to be upgraded. On the membrane side, we are currently exploring the new soft-clamped membranes which have demonstrated quality factor of $Q_m \approx 10^7 - 10^8$ [48] at room temperature. With the higher quality factor and the aid of cryogenic pre-cooling, we can attempt sympathetic cooling of the membrane to the ground

state using the spin. On the spin side, we still need to understand the mismatch between the observed spin damping rate to that expected from spontaneous emission. One possibility is that there is inhomogeneous broadening resulted from the vector or tensor light shift. In addition, it is worth to vary the atomic ensemble and probe beam geometry experimentally to verify if the spin measurement rate is consistent with the non-uniform atom-light coupling description as discussed in the Chapter 3 [73]. It would be interesting to study the quantum limits of the individual coherent feedback systems and eventually the quantum coherent coupling between the spin-membrane system.

To sum up, we have demonstrated the first application of our strong coupling control offered by our spin-membrane system, i.e. to use the spin as a quantum feedback controller to cool a nanomechanical membrane [66]. Such cooling strategy has already been put forward to be an interesting alternative solution to experimental systems to perform cooling without the need of an optical cavity as an interesting application [64]. Our results only marks the beginning of an interesting exploration in the field of coherent feedback. With future endeavor and progress towards realizing the spin membrane interface in the quantum-limited regime, our coherent hybrid platform can find interesting applications for quantum control such as hybrid quantum network [111], state swaps of squeezed states from the spin to the membrane and entanglement [60–63].

Appendix A

Simulation of the spin-membrane dynamics

We present a theoretical simulation algorithm [106] that enables one to fit the time trace of the coupled spin membrane dynamics including the stochastic noise terms. From the Heisenberg-Langevin equations Eqs. 5.5-5.8, we present how we adapt the algorithm in [106] to perform stochastic simulation for our spin membrane system. The stochastic simulation are required to correctly account for the number of excitations of the coupled oscillator in the time domain of our main sympathetic cooling result. For the purpose of context, we consider the equations of motion for X_j and P_j with $j \in (m,s)$ restricted to loop phase of $\phi = \pi$:

$$\dot{X}_m(t) = \Omega_m P_m(t) \tag{A.1}$$

$$\dot{P}_m(t) = -\Omega_m X_m(t) - \gamma_m P_m(t) - 2g X_s(t-\tau) - \mathcal{F}_m(t) \tag{A.2}$$

$$\dot{X}_s(t) = \Omega_s P_s(t) \tag{A.3}$$

$$\dot{P}_s(t) = -\Omega_s X_s(t) - \gamma_s P_s(t) + 2g \cos(\phi) X_m(t-\tau) - \mathcal{F}_s(t) \tag{A.4}$$

where we have introduced the generalized noise forces $\mathcal{F}_j(t) = \sqrt{2\gamma_j} F_j^{(\text{tot})}(t)$. The total force noise $F_j^{(\text{tot})}(t)$ includes the thermal noise $F_j^{(\text{th})}(t)$ and the back-action noise $F_j^{(\text{ba})}(t)$ which itself depends on the optical vacuum noise $F_j^{(\text{in})}(t)$. Thus, it is given by

$$
\begin{aligned}
F_j^{(\text{tot})}(t) &= F_j^{(\text{th})}(t) + F_j^{(\text{ba})}(t) \\
&= F_j^{(\text{th})}(t) + \sqrt{\frac{2\Gamma_j}{\gamma_j}} F_j^{(\text{in})}(t)
\end{aligned}
\tag{A.5}
$$

where Γ_j is the measurement rate of the individual systems. To further simplify the above equations, we move to a frame rotating at the membrane frequency Ω_m

$$
\begin{aligned}
\tilde{X}_j &= X_j \cos(\Omega_m t) - P_j \sin(\Omega_m t) \\
\tilde{P}_j &= X_j \sin(\Omega_m t) + P_j \cos(\Omega_m t)
\end{aligned}
\tag{A.6}
$$

Let's work through a single example e.g. $\dot{\tilde{X}}_m(t)$

$$\dot{\tilde{X}}_m(t) = \dot{X}_m(t)\cos(\Omega_m t) - X_m\Omega_m\sin(\Omega_m t) - \dot{P}_m(t)\sin(\Omega_m t) - P_m\Omega_m\cos(\Omega_m t)$$
$$= \gamma_m\sin(\Omega_m t)P_m(t) + 2g\sin(\Omega_m t)X_s(t-\tau) + \mathcal{F}_m\sin(\Omega_m t) \tag{A.7}$$

Here, we consider the limit where the propagation delay is small compared to other timescales involved in the coupled dynamics (i.e. $\tau \ll \gamma_j^{-1}, g^{-1}, \delta^{-1}$), where we introduced the spin-membrane detuning $\delta = \Omega_s - \Omega_m$. Therefore, we may approximate[1] $X_s(t-\tau) \approx X_s\cos(\Omega_s\tau) + P_s\sin(\Omega_s\tau)$. Substituting the lab frame operators X_j, P_j by slow varying operators $\tilde{X}_j$, $\tilde{P}_j$, and applying the rotating wave approximation (i.e. dropping $2\Omega_m$ term),

$$\cos^2(\Omega_m t) = \frac{1 + 2\cos(2\Omega_m t)}{2} \approx 1/2$$
$$\sin^2(\Omega_m t) = \frac{1 - 2\cos(2\Omega_m t)}{2} \approx 1/2 \tag{A.9}$$
$$\cos(\Omega_m t)\sin(\Omega_m t) = \frac{\sin(2\Omega_m t)}{2} \approx 0$$

The slow varying membrane position quadrature $\dot{\tilde{X}}_m(t)$ now reads

$$\dot{\tilde{X}}_m(t) = -\gamma_m\tilde{P}_m/2 + g[\sin(\Omega_m\tau)\tilde{X}_m(t) + \cos(\Omega_m\tau)\tilde{P}_m(t)] + \mathcal{F}_m\sin(\Omega_m t) \tag{A.10}$$

Repeating similar calculations, we get the new equations of motion in slowly varying operators

$$\frac{d}{dt}\begin{pmatrix} \tilde{X}_m(t) \\ \tilde{P}_m(t) \\ \tilde{X}_s(t) \\ \tilde{P}_s(t) \end{pmatrix} = -\mathbf{M}\begin{pmatrix} \tilde{X}_m(t) \\ \tilde{P}_m(t) \\ \tilde{X}_s(t) \\ \tilde{P}_s(t) \end{pmatrix} + \begin{pmatrix} -\sin(\Omega_m t)\mathcal{F}_m(t) \\ \cos(\Omega_m t)\mathcal{F}_m(t) \\ -\sin(\Omega_m t)\mathcal{F}_s(t) \\ \cos(\Omega_m t)\mathcal{F}_s(t) \end{pmatrix}, \tag{A.11}$$

where we have split the dynamics into the 4×4 time independent dynamical matrix

$$M = \begin{pmatrix} \gamma_m/2 & 0 & -g\sin(\Omega_m\tau) & -g\cos(\Omega_m\tau) \\ 0 & \gamma_m/2 & g\cos(\Omega_m\tau) & -g\sin(\Omega_m\tau) \\ -g\sin(\Omega_m\tau) & -g\cos(\Omega_m\tau) & \gamma_s/2 & -\delta \\ g\cos(\Omega_m\tau) & -g\sin(\Omega_m\tau) & \delta & \gamma_s/2 \end{pmatrix} \tag{A.12}$$

---

[1]Using the general oscillator solution for $X_s(t)$ and $P_s(t)$,

$$X_s(t-\tau) = X_s(0)\cos(\Omega_s(t-\tau)) + P_s(0)\sin(\Omega_s(t-\tau))$$
$$= X_s(0)[\cos(\Omega_s t)\cos(\Omega_s\tau) + \sin(\Omega_s t)\sin(\Omega_s\tau)] + P_s(0)[\sin(\Omega_s t)\cos(\Omega_s\tau) - \cos(\Omega_s t)\sin(\Omega_s\tau)]$$
$$\approx X_s(t)\cos(\Omega_s\tau) + P_s(t)\sin(\Omega_s\tau)$$

$$\tag{A.8}$$

and the stochastic noise part, which is now entering both $\tilde{X}_j$ and $\tilde{P}_j$. The noise terms $F_j^{(\nu)}(t)$, $\nu \in (\text{th}, \text{in})$ can be expressed explicitly in terms of the product of a noise amplitude and a zero mean, delta correlated noise $f_j^{(\nu)}(t)$:

$$
\begin{aligned}
F_j^{(\text{th})}(t) &= \sqrt{\bar{n}_{j,\,\text{bath}} + \frac{1}{2}}\, f_j^{(\text{th})}(t), \\
F_m^{(\text{in})}(t) &= \sqrt{\frac{\eta^2}{2}}\, f_m^{(\text{in})}(t), \\
F_s^{(\text{in})}(t) &= \sqrt{\frac{1 - \eta^4}{2}}\, f_s^{(\text{in})}(t),
\end{aligned}
\tag{A.13}
$$

where $\eta^2 \approx 0.8$[2] is the power transmission coefficient of the light between the spin and the membrane and $\bar{n}_{j,\text{bath}}$ is the number of thermal phonons in the individual system. The number of thermal phonons of the membrane of the membrane $\bar{n}_{m,\text{bath}}$ was measured by homodyne detection in presence of all laser beams but without loading the atoms. This calibrated value agrees very well with an estimation from comparing the spectral linewidth in presence of the cooling and coupling beams with the spectral linewidth of the uncooled membrane and the calculated room temperature occupation of the membrane. We assumed the spin pumping to be perfect such that the spin oscillator environment is in its quantum mechanical ground state (i.e. $\bar{n}_{s,\text{bath}} = 0$).

Stochastic simulation algorithm

The approach given in [106] allows for an exact simulation of the stochastic dynamics for a single oscillator for arbitrary time steps, which we extend to the case of two coupled oscillators with delay. This is done by calculating for each time step the coherent evolution and the noise separately:

$$
\begin{pmatrix}
\tilde{X}_m(t_{i+1}) \\
\tilde{P}_m(t_{i+1}) \\
\tilde{X}_s(t_{i+1}) \\
\tilde{P}_s(t_{i+1})
\end{pmatrix}
= e^{-\mathbf{M}\Delta t}
\begin{pmatrix}
\tilde{X}_m(t_i) \\
\tilde{P}_m(t_i) \\
\tilde{X}_s(t_i) \\
\tilde{P}_s(t_i)
\end{pmatrix}
+
\begin{pmatrix}
\Delta \tilde{X}_m^{t_i \to t_{i+1}} \\
\Delta \tilde{P}_m^{t_i \to t_{i+1}} \\
\Delta \tilde{X}_s^{t_i \to t_{i+1}} \\
\Delta \tilde{P}_s^{t_i \to t_{i+1}}
\end{pmatrix},
\tag{A.14}
$$

where $\Delta t = t_{i+1} - t_i$ is one simulation time step, and $\Delta \tilde{X}_j^{t_i \to t_{i+1}}$, $\Delta \tilde{P}_j^{t_i \to t_{i+1}}$ are terms for the stochastic noise which enters the system in between time t_i and t_{i+1}. We performed the simulation at time steps comparable to the oscillation period Ω_m^{-1}. Thus, the noise terms $\Delta \tilde{X}_j^{t_i \to t_{i+1}}$ and $\Delta \tilde{P}_j^{t_i \to t_{i+1}}$ are correlated which is taken into account by following the calculation of noise variances and covariances in [106]. Because the coupling between the two oscillators is much slower than the simulation

---

[2]For perfect transmission, i.e. no optical losses $\eta^2 = 1$, and the optical vacuum noise destructively interferes.

time step $g \ll \Omega_m \approx \Delta t^{-1}$ we neglect the correlation of noise building up between the oscillators during one simulation step. Thus, we can treat the noise of both oscillators separately. In order to simulate the system more efficiently, we perform the simulation in time steps of multiples of one frame rotation $\Delta t = k \cdot 2\pi/\Omega_m$, $k = 1, 2, 3...$ such that the noise amplitudes [proportional to $\sin(\Omega_m t), \cos(\Omega_m t)$, see Eq. (A.11)] are the same for each the step of the simulation.

Bibliography

[1] Nicolas Gisin, Grégoire Ribordy, Wolfgang Tittel, and Hugo Zbinden. Quantum cryptography. Rev. Mod. Phys., 74:145–195, Mar 2002.

[2] Immanuel Bloch, Jean Dalibard, and Sylvain Nascimbène. Quantum simulations with ultracold quantum gases. Nature Phys, 8(4):267–276, April 2012.

[3] R. Blatt and D. Wineland. Entangled states of trapped atomic ions. Nature 453, pages 1008–1015, 2008.

[4] R. Hanson and D. Awschalom. Coherent manipulation of single spins in semiconductors. Nature 453, pages 1043–1049, 2008.

[5] J. J. L. Morton and B. W. Lovett. The powerful role of electron spins. Annu. Rev. of Condens. Matter Phys, 2:189–212, 2011.

[6] Morten Kjaergaard, Mollie E. Schwartz, Jochen Braumüller, Philip Krantz, Joel I.-J. Wang, Simon Gustavsson, and William D. Oliver. Superconducting Qubits: Current State of Play. Annual Review of Condensed Matter Physics, 11(1):369–395, 2020.

[7] J. Clarke and F. Wilhelm. Superconducting quantum bits. Nature 453, pages 1031–1042, 2008.

[8] M. Poot and H. van der Zant. Mechanical systems in the quantum regime. Phys Rep, 511(5):273–336, 2012.

[9] Markus Aspelmeyer, Tobias J. Kippenberg, and Florian Marquardt. Cavity optomechanics. Rev. Mod. Phys., 86(4):1391–1452, December 2014.

[10] Gershon Kurizki, Patrice Bertet, Yuimaru Kubo, Klaus Mølmer, David Petrosyan, Peter Rabl, and Jörg Schmiedmayer. Quantum technologies with hybrid systems. PNAS, 112(13):3866–3873, 2015.

[11] Donghun Lee, Kenneth W. Lee, Jeffrey V. Cady, Preeti Ovartchaiyapong, and Ania C. Bleszynski Jayich. Topical review: spins and mechanics in diamond. J. Opt., 19(3):033001, February 2017.

[12] Christoffer B. Møller, Rodrigo A. Thomas, Georgios Vasilakis, Emil Zeuthen, Yeghishe Tsaturyan, Mikhail Balabas, Kasper Jensen, Albert Schliesser, Klemens Hammerer, and Eugene S. Polzik. Quantum back-action-evading measurement of motion in a negative mass reference frame. Nature, 547(7662):191–195, July 2017.

[13] Andreas Jöckel, Aline Faber, Tobias Kampschulte, Maria Korppi, Matthew T. Rakher, and Philipp Treutlein. Sympathetic cooling of a membrane oscillator in a hybrid mechanical–atomic system. Nat. Nanotechnol., 10(1):55–59, Nov 2015.

[14] Thomas M. Karg, Baptiste Gouraud, Chun Tat Ngai, Gian-Luca Schmid, Klemens Hammerer, and Philipp Treutlein. Light-mediated strong coupling between a mechanical oscillator and atomic spins 1 meter apart. Science, 369(6500):174–179, July 2020.

[15] Rodrigo A. Thomas, Michał Parniak, Christoffer Østfeldt, Christoffer B. Møller, Christian Bærentsen, Yeghishe Tsaturyan, Albert Schliesser, Jürgen Appel, Emil Zeuthen, and Eugene S. Polzik. Entanglement between distant macroscopic mechanical and spin systems. Nat. Phys., 17(2):228–233, February 2021.

[16] D. Rugar, R. Budakian, H. J. Mamin, and B. W. Chui. Single spin detection by magnetic resonance force microscopy. Nature, 430(6997):329–332, July 2004.

[17] O. Arcizet, V. Jacques, A. Siria, P. Poncharal, P. Vincent, and S. Seidelin. A single nitrogen-vacancy defect coupled to a nanomechanical oscillator. Nat. Phys., 7(11):879–883, November 2011.

[18] A. Barfuss, J. Teissier, E. Neu, A. Nunnenkamp, and P. Maletinsky. Strong mechanical driving of a single electron spin. Nat. Phys., 11(10):820–824, October 2015.

[19] A. D. O'Connell, M. Hofheinz, M. Ansmann, Radoslaw C. Bialczak, M. Lenander, Erik Lucero, M. Neeley, D. Sank, H. Wang, M. Weides, J. Wenner, John M. Martinis, and A. N. Cleland. Quantum ground state and single-phonon control of a mechanical resonator. Nature, 464(7289):697–703, April 2010.

[20] Patricio Arrangoiz-Arriola, E. Alex Wollack, Zhaoyou Wang, Marek Pechal, Wentao Jiang, Timothy P. McKenna, Jeremy D. Witmer, Raphaël Van Laer,

and Amir H. Safavi-Naeini. Resolving the energy levels of a nanomechanical oscillator. Nature, 571(7766):537–540, July 2019.

[21] P. Treutlein, C. Genes, K. Hammerer, and M. Poggio. Hybrid mechanical systems. In Markus Aspelmeyer, Tobias J. Kippenberg, and Florian Marquardt, editors, Cavity Optomechanics: Nano- and Micromechanical Resonators Interacting with Light, pages 327–351. Springer Berlin Heidelberg, Berlin, Heidelberg, 2014.

[22] Stephan Camerer, Maria Korppi, Andreas Jöckel, David Hunger, Theodor W. Hänsch, and Philipp Treutlein. Realization of an optomechanical interface between ultracold atoms and a membrane. Phys. Rev. Lett., 107(22):223001, November 2011.

[23] Philipp Christoph, Tobias Wagner, Hai Zhong, Roland Wiesendanger, Klaus Sengstock, Alexander Schwarz, and Christoph Becker. Combined feedback and sympathetic cooling of a mechanical oscillator coupled to ultracold atoms. New J. Phys., 20(9):093020, September 2018.

[24] I. Yeo, P.-L. de Assis, A. Gloppe, E. Dupont-Ferrier, P. Verlot, N. S. Malik, E. Dupuy, J. Claudon, J.-M. Gérard, A. Auffèves, G. Nogues, S. Seidelin, J.-Ph Poizat, O. Arcizet, and M. Richard. Strain-mediated coupling in a quantum dot–mechanical oscillator hybrid system. Nat. Nanotechnol., 9(2):106–110, February 2014.

[25] Michele Montinaro, Gunter Wüst, Mathieu Munsch, Yannik Fontana, Eleonora Russo-Averchi, Martin Heiss, Anna Fontcuberta i Morral, Richard J. Warburton, and Martino Poggio. Quantum Dot Opto-Mechanics in a Fully Self-Assembled Nanowire. Nano Lett., 14(8):4454–4460, August 2014.

[26] A. A. Clerk, K. W. Lehnert, P. Bertet, J. R. Petta, and Y. Nakamura. Hybrid quantum systems with circuit quantum electrodynamics. Nat. Phys., 16(3):257–267, March 2020.

[27] Jian-Qi Zhang, Wei Xiong, Shuo Zhang, Yong Li, and Mang Feng. Generating the Schrödinger cat state in a nanomechanical resonator coupled to a charge qubit. Annalen der Physik, 527(1-2):180–186, 2015.

[28] M Wallquist, K Hammerer, P Rabl, M Lukin, and P Zoller. Hybrid quantum devices and quantum engineering. Physica Scripta, T137:014001, December 2009.

[29] M. Aspelmeyer, S. Gröblacher, K. Hammerer, and N. Kiesel. Quantum optomechanics throwing a glance. J. Opt. Soc. Am. B 27, A:189–197, 2010.

[30] Thomas M. Karg, Baptiste Gouraud, Philipp Treutlein, and Klemens Hammerer. Remote Hamiltonian interactions mediated by light. Phys. Rev. A, 99(6):063829, June 2019.

[31] H. J. Kimble. Strong interactions of single atoms and photons in cavity qed. Phys.Scr., page 127, 1998.

[32] Serge Haroche and Daniel Kleppner. Cavity Quantum Electrodynamics. Physics Today, 42(1):24–30, January 1989.

[33] Klemens Hammerer, Anders S. Sørensen, and Eugene S. Polzik. Quantum interface between light and atomic ensembles. Rev. Mod. Phys., 82:1041–1093, Apr 2010.

[34] Ferdinand Brennecke, Tobias Donner, Stephan Ritter, Thomas Bourdel, Michael Köhl, and Tilman Esslinger. Cavity QED with a Bose–Einstein condensate. Nature, 450(7167):268–271, November 2007.

[35] A. E. Kozhekin, K. Mølmer, and E. Polzik. Quantum memory for light. Phys. Rev. A, 62:033809, Aug 2000.

[36] Ivan H. Deutsch and Poul S. Jessen. Quantum control and measurement of atomic spins in polarization spectroscopy. Optics Communications, 283:681–694, 2010.

[37] E. M. Eugeniy and I. Novikova. Low-frequency vacuum squeezing via polarization self-rotation in rb vapor. Optics Letters, 33, 2008.

[38] A. Kuzmich, L. Mandel, and N. P. Bigelow. Generation of spin squeezing via continuous quantum nondemolition measurement. Phys. Rev. Lett., 85:1594–1597, Aug 2000.

[39] B. Julsgaard, A. Kozhekin, and E. S. Polzik. Experimental long-lived entanglement of two macroscopic objects. Nature, 413:400–403, 2001.

[40] Luca Pezzè, Augusto Smerzi, Markus K. Oberthaler, Roman Schmied, and Philipp Treutlein. Quantum metrology with nonclassical states of atomic ensembles. Rev. Mod. Phys., 90:035005, Sep 2018.

[41] Brian Julsgaard, Jacob Sherson, J. Ignacio Cirac, Jaromír Fiurášek, and Eugene S. Polzik. Experimental demonstration of quantum memory for light. Nature, 432(7016):482–486, November 2004.

[42] Jacob F. Sherson, Hanna Krauter, Rasmus K. Olsson, Brian Julsgaard, Klemens Hammerer, Ignacio Cirac, and Eugene S. Polzik. Quantum teleportation between light and matter. Nature, 443(7111):557–560, October 2006.

124

[43] M. Napolitano, M. Koschorreck, B. Dubost, N. Behbood, R. J. Sewell, and M. W. Mitchell. Interaction-based quantum metrology showing scaling beyond the Heisenberg limit. Nature, 471(7339):486–489, March 2011.

[44] W. Wasilewski, K. Jensen, H. Krauter, J. J. Renema, M. V. Balabas, and E. S. Polzik. Quantum noise limited and entanglement-assisted magnetometry. Phys. Rev. Lett., 104:133601, Mar 2010.

[45] D. Leibfried, R. Blatt, C. Monroe, and D. Wineland. Quantum dynamics of single trapped ions. Rev. Mod. Phys., 75:281–324, Mar 2003.

[46] G. Anetsberger, R. Rivière, A. Schliesser, O. Arcizet, and T. J. Kippenberg. Ultralow-dissipation optomechanical resonators on a chip. Nature Photon, 2(10):627–633, October 2008.

[47] E. Serra, A. Borrielli, F. S. Cataliotti, F. Marin, F. Marino, A. Pontin, G. A. Prodi, and M. Bonaldi. Ultralow-dissipation micro-oscillator for quantum optomechanics. Phys. Rev. A, 86:051801, Nov 2012.

[48] Y. Tsaturyan, A. Barg, E. S. Polzik, and A. Schliesser. Ultracoherent nanomechanical resonators via soft clamping and dissipation dilution. Nat. Nanotechnol., 12(8):776–783, August 2017.

[49] A. H. Ghadimi, S. A. Fedorov, N. J. Engelsen, M. J. Bereyhi, R. Schilling, D. J. Wilson, and T. J. Kippenberg. Elastic strain engineering for ultralow mechanical dissipation. Science, 360(6390):764–768, May 2018.

[50] Massimiliano Rossi, David Mason, Junxin Chen, Yeghishe Tsaturyan, and Albert Schliesser. Measurement-based quantum control of mechanical motion. Nature, 563(7729):53–58, November 2018.

[51] J. D. Teufel, T. Donner, Dale Li, J. W. Harlow, M. S. Allman, K. Cicak, A. J. Sirois, J. D. Whittaker, K. W. Lehnert, and R. W. Simmonds. Sideband cooling of micromechanical motion to the quantum ground state. Nature, 475(7356):359–363, July 2011.

[52] Haocun Yu, L. McCuller, M. Tse, N. Kijbunchoo, L. Barsotti, N. Mavalvala, and members of the LIGO Scientific Collaboration. Quantum correlations between light and the kilogram-mass mirrors of LIGO. Nature, 583(7814):43–47, July 2020.

[53] Alexander G. Krause, Martin Winger, Tim D. Blasius, Qiang Lin, and Oskar Painter. A high-resolution microchip optomechanical accelerometer. Nature Photon, 6(11):768–772, November 2012.

[54] E. E. Wollman, C. U. Lei, A. J. Weinstein, J. Suh, A. Kronwald, F. Marquardt, A. A. Clerk, and K. C. Schwab. Quantum squeezing of motion in a mechanical resonator. Science, 349(6251):952–955, August 2015.

[55] K. Jähne, C. Genes, K. Hammerer, M. Wallquist, E. S. Polzik, and P. Zoller. Cavity-assisted squeezing of a mechanical oscillator. Phys. Rev. A, 79:063819, Jun 2009.

[56] T. P. Purdy, P.-L. Yu, R. W. Peterson, N. S. Kampel, and C. A. Regal. Strong optomechanical squeezing of light. Phys. Rev. X, 3:031012, Sep 2013.

[57] Moritz Forsch, Robert Stockill, Andreas Wallucks, Igor Marinković, Claus Gärtner, Richard A. Norte, Frank van Otten, Andrea Fiore, Kartik Srinivasan, and Simon Gröblacher. Microwave-to-optics conversion using a mechanical oscillator in its quantum ground state. Nat. Phys., 16(1):69–74, January 2020.

[58] Aline Vochezer, Tobias Kampschulte, Klemens Hammerer, and Philipp Treutlein. Light-mediated collective atomic motion in an optical lattice coupled to a membrane. Phys. Rev. Lett., 120(7):073602, February 2018.

[59] Thomas Karg. Strong light-mediated coupling between a membrane oscillator and an atomic spin ensemble. University of Basel, 2020.

[60] Jing Zhang, Yu xi Liu, Re-Bing Wu, Kurt Jacobs, and Franco Nori. Quantum feedback: Theory, experiments, and applications. Phys. Rep., 679:1–60, 2017.

[61] Seth Lloyd. Coherent quantum feedback. Phys. Rev. A, 62:022108, Jul 2000.

[62] Howard M. Wiseman and Gerard J. Milburn. Quantum Measurement and Control. Cambridge University Press, 2009.

[63] Ryan Hamerly and Hideo Mabuchi. Advantages of coherent feedback for cooling quantum oscillators. Phys. Rev. Lett., 109:173602, Oct 2012.

[64] James S Bennett, Lars S Madsen, Mark Baker, Halina Rubinsztein-Dunlop, and Warwick P Bowen. Coherent control and feedback cooling in a remotely coupled hybrid atom–optomechanical system. New J. Phys., 16(8):083036, August 2014.

[65] M. Wallquist, K. Hammerer, P. Zoller, C. Genes, M. Ludwig, F. Marquardt, P. Treutlein, J. Ye, and H. J. Kimble. Single-atom cavity QED and optomicromechanics. Phys. Rev. A, 81(2):023816, February 2010.

[66] Gian-Luca Schmid, Chun Tat Ngai, Maryse Ernzer, Manel Bosch Aguilera, Thomas M. Karg, and Philipp Treutlein. Coherent feedback cooling of a nanomechanical membrane with atomic spins. Phys. Rev. X, 12:011020, Jan 2022.

[67] T. Holstein and H. Primakoff. Field Dependence of the Intrinsic Domain Magnetization of a Ferromagnet. Phys. Rev., 58(12):1098–1113, December 1940.

[68] J M Radcliffe. Some properties of coherent spin states. Journal of Physics A: General Physics, 1971.

[69] R. Loudon. The Quantum Theory of Light. Oxford University Press, 2000.

[70] Denis Vasilyev, Klemens Hammerer, N Korolev, and A S Sørensen. Quantum noise for faraday light–matter interfaces. Journal of Physics B: Atomic, Molecular and Optical Physics, 2012.

[71] M. Kubasik, M. Koschorreck, M. Napolitano, S. R. de Echaniz, H. Crepaz, J. Eschner, E. S. Polzik, and M. W. Mitchell. Polarization-based light-atom quantum interface with an all-optical trap. Phys. Rev. A, 79:043815, Apr 2009.

[72] Rodrigo A. Thomas. Optical spin-mechanics quantum interface: entanglement and back-action evasion. University of Copenhagen, 2020.

[73] Ben Q. Baragiola, Leigh M. Norris, Enrique Montaño, Pascal G. Mickelson, Poul S. Jessen, and Ivan H. Deutsch. Three-dimensional light-matter interface for collective spin squeezing in atomic ensembles. Phys. Rev. A, 89(3):033850, March 2014.

[74] Jiazhong Hu, Wenlan Chen, Zachary Vendeiro, Hao Zhang, and Vladan Vuletić. Entangled collective-spin states of atomic ensembles under nonuniform atom-light interaction. Phys. Rev. A, 92:063816, Dec 2015.

[75] Brian Julsgaard. Entanglement and quantum interactions with macroscopic gas samples. Aarhus Universitetsforlag, 2003.

[76] F. Ya. Khalili and E. S. Polzik. Overcoming the standard quantum limit in gravitational wave detectors using spin systems with a negative effective mass. Phys. Rev. Lett., 121:031101, Jul 2018.

[77] V. B. Braginsky, Y. I. Vorontsov, and Thorne K. S. Quantum non demolition measurements. Science, 1980.

[78] Kip S. Thorne, Ronald W. P. Drever, Carlton M. Caves, Mark Zimmermann, and Vernon D. Sandberg. Quantum nondemolition measurements of harmonic oscillators. Phys. Rev. Lett., 40:667–671, Mar 1978.

[79] A. A. Clerk, M. H. Devoret, S. M. Girvin, Florian Marquardt, and R. J. Schoelkopf. Introduction to quantum noise, measurement, and amplification. Rev. Mod. Phys., 82:1155–1208, Apr 2010.

[80] G. J. Milburn W. P. Bowen. Quantum Optomechanics. CRC Press, October 2015.

[81] H. J. Kimble, Yuri Levin, Andrey B. Matsko, Kip S. Thorne, and Sergey P. Vyatchanin. Conversion of conventional gravitational-wave interferometers into quantum nondemolition interferometers by modifying their input and/or output optics. Phys. Rev. D, 65:022002, Dec 2001.

[82] J Appel, A MacRae, and Lvovsky A I. A versatile digital ghz phase lock for external cavity diode lasers. Meas. Sci. Technol. 20 055302, 2009.

[83] MSquared. SolsTiS User Manual v10.3, first edition edition, 2007.

[84] Gianni Buser. Dipole-trapped atoms at high optical depth for atom-light quantum interfaces. University of Basel, 2016.

[85] Andreas Jöckel. Sympathetic cooling of a membrane oscillator in a hybrid mechanical-atomic system. University of Basel, 2014.

[86] Aline Faber. Sympathetic cooling and self-oscillations in a hybrid atom-membrane system. PhD thesis, University of Basel, 2016.

[87] F Kaminski, N. S. Kampel, and M. P. H. Steenstrup. In-situ dual-port polarization contrast imaging of faraday rotation in a high optical depth ultracold 87rb atomic ensemble. The European Physical Journal D 66, Article number: 227, 2012.

[88] A. Daniel Steck. Rubidium 87 d line data. Los Alamos National Laboratory, 2001.

[89] B. Julsgaard, J. Sherson, Sørensen, J. L., and E. S. Polzik. Characterizing the spin state of an atomic ensemble using the magneto-optical resonance method. Journal of Optics B, 2003.

[90] C. W. Gardiner and M. J. Collett. Input and output in damped quantum systems: Quantum stochastic differential equations and the master equation. Phys. Rev. A, 31:3761–3774, Jun 1985.

[91] A. M. Jayich, J. C. Sankey, B. M. Zwickl, C. Yang, J. D. Thompson, S. M. Girvin, A. A. Clerk, F. Marquardt, and J. G. E. Harris. Dispersive optomechanics: a membrane inside a cavity. New J. Phys., 10(9):095008, September 2008. Publisher: IOP Publishing.

[92] P.-L. Yu, K. Cicak, N. S. Kampel, Y. Tsaturyan, T. P. Purdy, R. W. Simmonds, and C. A. Regal. A phononic bandgap shield for high-Q membrane microresonators. Appl. Phys. Lett., 104(2):023510, January 2014. Publisher: American Institute of Physics.

[93] Yeghishe Tsaturyan, Andreas Barg, Anders Simonsen, Luis Guillermo Villanueva, Silvan Schmid, Albert Schliesser, and Eugene S. Polzik. Demonstration of suppressed phonon tunneling losses in phononic bandgap shielded membrane resonators for high-Q optomechanics. Opt. Express, OE, 22(6):6810–6821, March 2014. Publisher: Optica Publishing Group.

[94] Eberhard P. Hofer. Grundlagen der Regelungstechnik/ Regelungstechnik 1. Open Access Repositorium der Universität Ulm, August 2008.

[95] Simon Gröblacher, Klemens Hammerer, Michael R. Vanner, and Markus Aspelmeyer. Observation of strong coupling between a micromechanical resonator and an optical cavity field. Nature, 460(7256):724–727, 2009.

[96] E. Verhagen, S. Deleglise, S. Weis, A. Schliesser, and T. J. Kippenberg. Quantum-coherent coupling of a mechanical oscillator to an optical cavity mode. Nature, 482(7383):63–67, 02 2012.

[97] Yiwen Chu and Simon Gröblacher. A perspective on hybrid quantum opto- and electromechanical systems. Appl. Phys. Lett., 117:150503, October 2020.

[98] Masashi Hirose and Paola Cappellaro. Coherent feedback control of a single qubit in diamond. Nature, 532(7597):77–80, April 2016.

[99] J. Zhang, R. Wu, Y. Liu, C. Li, and T. Tarn. Quantum coherent nonlinear feedback with applications to quantum optics on chip. IEEE Trans. Autom. Control, 57(8):1997–2008, 2012.

[100] Zhaoyou Wang and Amir H. Safavi-Naeini. Enhancing a slow and weak optomechanical nonlinearity with delayed quantum feedback. Nature Communications, 8:15886, July 2017.

[101] Alfred Harwood, Matteo Brunelli, and Alessio Serafini. Cavity optomechanics assisted by optical coherent feedback. Phys. Rev. A, 103:023509, 2021.

[102] M. J. Woolley and A. A. Clerk. Two-mode squeezed states in cavity optomechanics via engineering of a single reservoir. Phys. Rev. A, 89:063805, Jun 2014.

[103] Jie Li, Gang Li, Stefano Zippilli, David Vitali, and Tiancai Zhang. Enhanced entanglement of two different mechanical resonators via coherent feedback. Phys. Rev. A, 95(4):043819, April 2017.

[104] B. Vogell, T. Kampschulte, M. T. Rakher, A. Faber, P. Treutlein, K. Hammerer, and P. Zoller. Long distance coupling of a quantum mechanical oscillator to the internal states of an atomic ensemble. New J. Phys., 17(4):043044, April 2015.

[105] J. D. Thompson, B. M. Zwickl, A. M. Jayich, Florian Marquardt, S. M. Girvin, and J. G. E. Harris. Strong dispersive coupling of a high-finesse cavity to a micromechanical membrane. Nature, 452(7183):72–75, March 2008.

[106] Simon F. Nørrelykke and Henrik Flyvbjerg. Harmonic oscillator in heat bath: Exact simulation of time-lapse-recorded data and exact analytical benchmark statistics. Phys. Rev. E, 83(4):041103, April 2011.

[107] D. V. Ramana Reddy, A. Sen, and G. L. Johnston. Time delay induced death in coupled limit cycle oscillators. Phys. Rev. Lett., 80:5109–5112, Jun 1998.

[108] D. V. Ramana Reddy, A. Sen, and G. L. Johnston. Experimental evidence of time-delay-induced death in coupled limit-cycle oscillators. Phys. Rev. Lett., 85:3381–3384, Oct 2000.

[109] C. Reetz, R. Fischer, G. G. T. Assumpção, D. P. McNally, P. S. Burns, J. C. Sankey, and C. A. Regal. Analysis of Membrane Phononic Crystals with Wide Band Gaps and Low-Mass Defects. Phys. Rev. Appl., 12(4):044027, October 2019.

[110] Mingfeng Wang, Weizhi Qu, Pengxiong Li, Han Bao, Vladan Vuletić, and Yanhong Xiao. Two-axis-twisting spin squeezing by multipass quantum erasure. Phys. Rev. A, 96:013823, Jul 2017.

[111] H. J. Kimble. The quantum internet. Nature, 453(7198):1023–1030, June 2008.

Acknowledgements

Throughout my PhD studies, I was very fortunate to work on this state-of-the-art experiment and, more importantly, I was able to spend valuable time with like-minded colleagues during my PhD journey. Looking back now, it wouldn't have been possible without the help and support I received. I would like to take this opportunity to express my gratitude to each one of you.

I would like to thank my direct supervisor Prof. Philipp Treutlein for offering me the opportunity to work on this beautiful experiment. Your insight into optomechanics and atomic physics was very useful when we encountered a problem. The scientific methodology I learnt from you will benefit me not only in physics but solve any general problems in life. Moreover, you provided me with a lot of freedom in researching which cultivated me into being an independent physicist.

I would like to acknowledge my PhD committee members - Prof. Christoph Bruder and Prof. Eugene Polzik for reviewing my thesis and providing invaluable feedback on my work. Your expertise in physics always inspired me to view a problem from different angles and learn deeply about the subject.

Amongst my colleagues, I would like to say special thanks to Gian-Luca Schmid, Maryse Ernzer, Manel Bosch, Thomas Karg and Baptiste Gouraud for working together on this project. You are all always very patient and eager to help whenever I faced any problems. I spent most of my working time with Gian-Luca, it was a pleasure working with you. We shared a lot of work both in the lab and in theory. Sometimes we had different ideas and approaches to a problem, which made the discussion very interesting and rewarding. I would like to thank Maryse and Manel for sharing their knowledge, especially on the optomechanics part of the setup. Moreover, I also appreciate the comments and feedback on my thesis from all of you. During the early phase of my PhD, I would like to thank Thomas and Baptiste for passing their knowledge to me, the theory and physics knowledge you shared with me had been invaluable throughout my PhD thesis, and you set up a role model of what a mature researcher looks like. I would also like to show my appreciation to the rest of the group members, you all provided very good input